Toward the temperature and strain discrimination by Brillouin based distributed fiber sensor

Camille Sabatier

N° d'ordre NNT: 2019LYSES027

PhD Thesis University of LYON (France)
In co-tutelle with
Politecnico di Bari (Italy)

Ecole Doctorale N° ED SIS 488

10/16/2019

Camille Sabatier

Towards the temperature and strain discrimination by Brillouin based distributed fiber sensor

---

Reviewers :

Prof. Bao Xiaoyi	Center for Research in Photonics at the University of Ottawa
Prof. Mégret Patrice	Head of the Electromagnetism and Telecommunication Department, Université de Mons

Examiners :

Prof. Vincent Brice	Département Nanomatériaux, Electronique Et Vivant, Université de Lorraine
Dr. Rizzolo Serena	Airbus Defense and Space
Prof. Carpentieri Mario	Politecnico di Bari

Supervisors :

Prof. Marin Emmanuel	Laboratoire Hubert Curien, Université de Saint Etienne
Prof. Mescia Luciano	Politecnico di Bari
Prof. Girard Sylvain	Laboratoire Hubert Curien, Université de Saint Etienne

Glossary

SHM: Structura Healtj Monitoring

OFS: Optical Fiber Sensor

DOFS: Distributed Optical Fiber Sensor

OTDR: Optical Time Domain Reflectometry

OFDR: Optical Frequency Domain Reflectometry

FFT: Fast Fourier Transform

IFFT: Inverse Fast Fourier Transform

DTS: Distributed Temperature Sensor

R-OTDR: Raman-Optical Time Domain Reflectometer

R-OFDR: Raman-Optical Frequency Domain Reflectometer

BOTDR: Brillouin Optical Time Domain Reflectometer

BOFDR: Brillouin Optical Frequency Domain Reflectometer

BOTDA: Brillouin Optical Time Domain Analysis

BOFDA: Brillouin Optical Frequency Domain Analysis

BOCDA: Brillouin Optical Correlation Domain Analyzer

DPP: Differential Pulse Pair

EOM: Electro Optic Modulator

BFS: Brillouin Frequency Shift

SG: Signal Generator

TLS: Tunable Laser Source

EM: Electro Magentic

SBS: Stimulated Brillouin Scattering

FWHM: Full Width at Half Maximum

SNR: Signal to Noise Ratio

PM: Polarization Maintaining

PMF: Polarization Maintaining Fiber

LPR: Landau-Placzek Ratio

SMF: Single Mode Fiber

RIP: Refractive Index Profile

AVP: Acoustic Velocity Profile

FEM: Finite Element Method

IFA: Inter Fiber Analysis

MCVD: Modified Chemical Vapor Deposition

EMPA: Electron MicroProbe Analysis

DTSS: Distributed Temperature Strain Sensor

RIA: Radiation Induced Attenuation

REMERCIEMENTS

Je souhaite, en premier lieu remercier M. Peyron, mon professeur de physique en classe de terminal. Je le remercie pour sa pédagogie et sa capacité à transmettre son savoir. Il a su me pousser, me faire apprécier les sciences physiques et m'a encouragé à faire une des études de physique. Une pensée aussi pour les professeurs M. Oriol et M. Nau, professeurs d'électronique et de mécanique. Je les remercie aussi pour leur éternel débat du plus inutile entre l'électronique et la mécanique. Il semblerait que le débat soit clos, car à l'heure où j'écris ces mots, je travaille en tant qu'ingénieur en électronique (après une thèse en optique).

Pour continuer, je souhaiterais remercier mes professeurs d'université dans leur ensemble et plus particulièrement M. Moine. Merci pour la pédagogie, les cours d'optique et son aide pour mes choix d'orientations et de stages.

Il est maintenant temps de remercier les personnes qui m'ont permis de réaliser ce travail de thèse et qui m'accompagnent encore aujourd'hui.

Je vais donc commencer par Serena Rizzolo. Serena, apparemment je vais encore te suivre pendant un moment. Je vais donc commencer par te remercier pour le stage que j'ai réalisé sous ta tutelle en 2015. Tout d'abord, tu m'as fait découvrir le monde de la recherche et plus particulièrement les fibres optiques. J'ai aussi rencontré quelqu'un de souriant et motivant. Je me souviens de notre première mission au CEA, des sorties après le travail, je pense d'ailleurs te facturer les frais de dentiste. Tu m'as permis d'obtenir une thèse, d'obtenir un travail, et puis tu m'as remonté le moral pendant ces 4 années. Je préfère m'arrêter là car ces remerciements sont publics. Donc merci !!

Je vais ensuite remercier Adriana Morana. Décidemment, la Sicile a un pouvoir d'attraction. Adriana, j'attends toujours que tu me dises bonjour quand tu me croises dans les couloirs. Trèves de plaisanteries, j'ai rencontré Adriana au CEA dirons-nous, je la remercie pour nos nombreuses missions passées ensemble, le soutien et l'aide apportée pendant la thèse. Je me souviens de pleins de moments mais particulièrement d'une photo où l'on débobinait une fibre pour le CNES. Je me souviens aussi d'un moment avec toi et Serena sur l'origine de mon prénom. Bref pour tous ces moments merci.

Je remercie aussi Marine Aubry. Que dire, si ce n'est que notre première rencontre fut improbable, puis la deuxième au RADECS aussi. Tu m'as soutenu jusqu'au bout dans mon projet universitaire et professionnel. Je pense à notre trio de choc dans le bureau, au défi avec

les fibres carbonées, les cachoteries avec le groupe, ta joie de vivre. Pour tout cela merci et merci aussi d'être entrée dans ma vie. Pour la suite de mes remerciements je pense à Maxime Royon. On a commencé au même endroit, je repense à tous les bons moments dans le bureau, ton « ah ouais », ton aide, tes théories sur les films.

Je tenais aussi à remercier Antonino. Je commencerais par les nombreux cafés pris pendant ton mal de tête, puis les moments plus marrants ensemble. Merci de m'avoir montré la vérité sur MMF, et puis aussi pour notre marathon au RADECS 2017 à Genève.

Je remercie aussi toute l'équipe de doctorants de MOPERE, en commençant par Timothé, camarade de longue date à Saint Etienne, Thomas pour ses débats avec Cyprien. Une pensée pour Cyprien qui fait vraiment. Merci à Vincenzo et Cosimo pour m'avoir appris les rudiments de l'italien.

Je souhaite aussi remercier Gilles Mélin, pour tous les bons moments passé en conférence, tes passages à Saint Etienne, notre équipe d'irréductibles pendant les repas professionnels et aussi pour ton aide tout au long de ma thèse.

Merci à Thierry Robin qui m'a laissé une chance et m'a permis de faire ma thèse avec iXblue. Je le remercie pour son aide

Merci à l'équipe du CEA DAM, j'ai nommé Claude, Olivier, Martial, Philippe toujours accueillant et serviable, je les remercie aussi pour les expériences à Gramat. Un gros merci à Marc Gaillardin, qui m'a clairement sauvé mon RADECS 2018, et aussi pour les bons moments passés.

Pour commencer avec mes encadrants de thèse, je voudrais remercier Youcef Ouerdane, pour son écoute sa motivation et sa vision des choses. J'espère lui montrer à travers ce manuscrit que maintenant je peux toucher mon oreille sans faire le tour de ma tête. Youcef merci pour ces dix années, pour ton accompagnement et ta gentillesse.

Ensuite je remercie Aziz Boukenter pour son calme, son accompagnement. Je le remercie aussi pour ses cours privés en master et sa connaissance. Merci pour ces dix ans.

Vorrei ringraziare Luciano Mescia, il mio co-direttore di tesi in Italia. Grazie per l'accoglienza nel tuo laboratorio. Mi hai anche fatto scoprire le gioie del Sud Italia. Ti ringrazio per il tuo aiuto durante la tesi.

Pour finir avec mes encadrants de thèse je voudrais remercier Sylvain Girard. J'ai eu Sylvain comme professeur en 2013, je le remercie de m'avoir sélectionné pour cette thèse. Malgré la difficulté, je te remercie de m'avoir fait évoluer sur mon travail, de m'avoir permis de publier, de collaborer avec le CNES, Andra, le CEA, ou encore Viavi, bref merci pour les opportunités, promis j'essaierais d'améliorer mon anglais pour la suite. Merci pour ces 6 ans.

Enfin je voulais remercier mon directeur de thèse Emmanuel Marin, sans qui tout cela ne serait pas possible. Je me souviens des premiers jours de thèse où tu m'expliquais les difficultés de la thèse, et 3 ans et demi plus tard, je peux le dire tu avais raison. Merci pour ton aide, ta patience, tes conseils, les moments à l'extérieur, les parties de foot avec mon superbe maillot, les conférences et ton encadrement. Merci pour ces 5 ans.

Merci aussi aux autres membres du laboratoire Hubert Curien, aux collègues d'iXblue et l'équipe du Politecnico di Bari.

Merci à la fine équipe à savoir Ludovic Jordan, Anthony Cespedes, Canelle Grizard-ferrand. 11 ans d'amitié, ça serait trop long mais merci pour tous les bons moments, en particulier pour 2017, j'espère bien repartir pour 10 ans avec vous.

Pour terminer, je tenais à remercier mes parents et ma sœur. Merci de m'avoir permis d'arriver jusque-là, on peut dire que je n'étais pas bien parti à la base. Merci pour le soutien, de m'avoir permis de ne manquer de rien, de me pousser dans ce que je faisais, de m'avoir forcé à travailler à l'école, de m'avoir gâté. Merci aussi à Agathe pour tous les bons moments à Montpellier et de ton soutien !!

Patience et longueur de temps font plus que force ni que rage

Jean de la Fontaine

Introduction

Today, the structural health monitoring (SHM) of the developed infrastructures, facilities and factories relies more and more on advanced technologies, including those based on optical fibers. SHM allows detecting and assessing the tolerance of those sites to natural hazards, such as earthquakes, fires, overflows and can on a more regular basis serve to continuously monitor their energetic performances as an example. The most common type of measurements regards the spatio-temporal evolutions of the temperature and the strain, two environmental parameters of major importance defining the infrastructure lifetime and performances. Those technologies require the development of a network of sensors combining multiple sensitive elements and associated interrogators. Of course, most of those systems benefit from the huge market of microelectronics that provides advanced and low-cost components for those needs. Thanks to the miniaturization of the electronic systems, the sensors are less and less intrusive.

In parallel, the telecommunications market has strongly increased, as well as the one devoted to optical fiber technologies. The intensive production of optical fibers and the mitigation of the physical mechanisms (such as nonlinear effects) limiting the data transfer capacity has opened new perspectives for sensors exploiting these effects to functionalize the optical fiber as a sensitive element. In addition, as optical fibers are naturally slightly intrusive, immune to most of the electromagnetic perturbations and can be easily multiplexed, they quickly appear as a serious candidate to compete with other technologies for SHM. Today, two classes of fiber optic sensors are distinguished. The first type, point sensors (such as the Bragg gratings), uses the dependence of the refractive index on the stress or the temperature to measure these two parameters. This type of sensor offers similar or better performances than conventional sensors, but can be optimized to allow monitoring in very severe conditions: nuclear, high temperature, humidity, ignition risks, etc. The second type of optical fiber sensor is said to be distributed. For distributed sensors, the fiber itself serves as the sensitive element and is interrogated through a reflectometry technique. These sensors then allow monitoring temperature or stress all along the waveguide, potentially over tens of kilometers. This relatively new technology is a real revolution in the field of sensors. Indeed, electronic sensors offer point-by-point measurements, then an optical fiber can replace a huge number of electronic sensors, reducing strongly the implementation constraints and potentially the costs. Distributed optical fiber sensors therefore provide major advantages for the SHM of large facilities or in severe environments as those encountered in oil and gas industry, nuclear domain or geophysics fields.

Regarding the context of this PhD thesis, the presented work has been done in the framework of a collaboration between three entities:

- iXblue, an industrial specialized in the development of specialty optical fibers and the production of optical components using these optical fibers.
- The Hubert Curien Laboratory (LabHC), and more particularly its team Materials for Optics and Photonics in Extreme Radiation Environments (MOPERE). MOPERE works on the optimization of optical materials, components and systems for their integration in harsh environments.
- The Politecnico di Bari, polytechnic school in Italy (Bari), with a strong expertise in Multiphysics modeling tools.

This PhD thesis is the third joint work between these three structures leading to a PhD thesis. Indeed, considering the interests and competences of each actor, the consortium appears as very promising to overcome some of the observed limitation in the optical sensor field. For iXblue the development of a new generation of specialty optical fiber to anchor in the sensor market is of great interest, especially since iXblue is already established in the field of underwater surveillance and also in the offshore. LabHC can bring its expertise in the field of optical fiber sensor and sensor development. The MOPERE group has already developed and optimized various categories of fiber optic sensors through collaborations with institutes such as ANDRA, AREVA, and the “Commissariat à l’Energie Atomique” (CEA). Finally the Politecnico di Bari, will bring its expertise in terms of multiphysics and guided optics modeling.

The objectives of this PhD thesis are to propose new solutions in order to overcome the limitations of the existing distributed sensors based on the Brillouin scattering. For this, the work will be focused on the optimization of the structure and optical properties of the optical fibers serving as the sensitive element. More specifically, the main goal is to conceive and produce an optical fiber rendering possible to discriminate between the spatio-temporal evolutions of the temperature and of the strain along a single optical fiber through Brillouin-based measurements. To achieve this task, it will be necessary to apprehend the various physical effects at stake as well as their impact on the fiber material, to model these effects

and the resulting Brillouin signature in order to predict the performances of the distributed sensors using this fiber. Then via the simulation model, it will be a question of defining the materials and the structures of the optical fibers making it possible to exceed the intrinsic limitations of the existing technology such as the temperature / strain discrimination via a Brillouin sensor operating a single optical fiber. The objective is to have a global view of the sensor and the solution provided by the thesis can be exploited industrially.

This manuscript is organized around three main chapters:

In a first part, a state-of-the-art about distributed optical fiber sensors will be given. The concept of this class of sensors will be introduced and their main types will be benchmarked in terms of principles and performances: technologies based on Raman, Brillouin and Rayleigh scatterings. This will justify our choice to focus on the Brillouin-based sensing during this work. As a consequence we will more deeply present the physics related to the Brillouin light scattering and detail how this effect can be exploited to build different architectures of distributed sensors. Finally we will analyzed the different solutions proposed in the literature to overcome the discrimination issue with Brillouin sensors. This review will justify the strategy chosen for this PhD thesis, strategy that will be then introduced with more details.

In a second step, we will present the selected simulation model to calculate the Brillouin spectrum of an optical fiber and its associated temperature and strain sensitivities. The validity of our tools is assessed by benchmarking our calculation results with literature data about the responses of different well-known optical fibers. In addition, a first parametric study of the influence of the fiber composition and its refractive index structure on its Brillouin response will be proposed. This last study will allow us to understand how a fiber structure characterized by several Brillouin peaks could open the way to the discrimination between the temperature and strain distributions along a unique optical fiber.

In the last chapter, we will present and discuss the acquired results, both theoretical and experimental during the PhD thesis. In a first step, the influence of different parameters on the Brillouin spectrum will be investigated, such as the core size, the size of doped cladding, the concentration of germanium and/or fluorine, and the refractive index shape. We then select the most favorable ones to achieve a Brillouin response with several (at least two) Brillouin peaks and distinct strain and temperature coefficients. Then, as the output results of our simulations, two optical fiber structures have been identified, manufactured by iXblue and

then characterized. The obtained experimental results will be then compared to the predictive simulations, demonstrating the achieved capabilities of temperature / strain discrimination. The performances of the developed sensor will be compared with similar technologies or research works available in the literature.

Finally, the main conclusions of this research work will be presented as well as the possible perspectives to complete and improve the results obtained during this PhD work.

Chapter I: Optical Fiber Sensors

Optical Fiber Sensors (OFSs) are attracting more and more interest thanks to the numerous advantages they have compared to their competitive technologies: high acquisition rate, low weight and volume leading to a very low intrusivity level in addition to their unique capacity to exploit the optical fiber as the sensitive element to offer distributed measurements. To illustrate the growing impact of this technology, one can cite the diversity of applications that have been investigated in the literature, such as the structural health monitoring (SHM) [1] even in harsh environments [2]–[6], aircraft [7], space programs [8], geotechnical domain [9], [10], medicine [11]… Moreover, we can also see the increasing trend for the OFS market: in 2013 the worldwide market was of about ~1.9 billions of US dollars while the previsions for 2024 are around 4.5 billions of US dollars [12]–[14]**.**

This chapter provides a state-of-the-art about OFS technologies, focusing on the various architectures of Distributed Optical Fiber Sensors (DOFSs) that generally combine the measurement of the different light scattering signatures of the silica-based optical fiber with reflectometry techniques. Indeed, the silica scattering properties strongly depend on its environmental conditions such as the temperature [15], the applied strain [16]**,** pressure [17], or the presence of a magnetic field [18]… Different classes of DOFSs have been built that use one of the three scattering phenomena: Rayleigh [19], Brillouin [20] and Raman [21]. Actually, the main limitation of DOFSs remains the spatial and time discrimination capacities between the different stimuli applied along the fiber sensing line. Indeed, Brillouin and Rayleigh scatterings are sensitive to both strain and temperature. It is then not possible using a unique DOFS basing on these signatures to determine the relative contributions of the two parameters on the global response. Different mitigation approaches have been investigated to overcome this drawback, the most evident one consisting in combining the measurements on two fibers with two different DOFSs.

In this chapter, a state-of-the-art on the DOFSs architectures and performances is presented. First, the main techniques are detailed and classified by the nature of the exploited scattering phenomenon. Attention is focused on the sensors using the Brillouin scattering that will be deeply investigated during the PhD work. In the second part, are detailed the main solutions that have been proposed for the discrimination between the strain and the temperature along a

unique fiber with a DOFS. Finally, the promising solutions that have been selected for investigation during this PhD thesis work will be introduced.

1.1. Light scattering in silica-based optical fiber

During the propagation of an electromagnetic wave into a silica–based optical fiber, three different scattering mechanisms are observed. These three phenomena, named Rayleigh, Brillouin, and Raman scatterings are illustrated in Figure 1.1. If the temperature and/or strain applied on the fiber changes, the light scattering will be modified. As a result by monitoring the spatial and time evolution of the backscattered light, the optical fiber can be used for strain and/or temperature monitoring.

Two main classes of DOFSs can be distinguished: the first one is based on the Optical Time Domain Reflectometry (OTDR) whereas the second one exploits the Optical Frequency Domain Reflectometry (OFDR). Concerning the OTDR technologies, the distributed capacity (spatial resolution) is directly related to the duration of the laser pulses launched into the fiber. Indeed, by measuring the propagation time of the pulsed light is it possible to determine the position where the external stimuli occurs. The relation between the laser pulse duration and the sensor spatial resolution DOFs is given by [22]:

$$\delta z = \frac{\tau c}{2 n_{eff}} \qquad (1.1)$$

where $\boldsymbol{\tau}$ is the width of the pulse light, $\boldsymbol{c}$ is the light celerity, and $\boldsymbol{n_{eff}}$ is the effective refractive index of the optical mode. The OTDR technology is used to probe the backscattered components of the Rayleigh [23], Brillouin [24], and Raman [25], [26] scatterings. Another approach is based on the OFDR technique. In this case, the DOF operates in the frequency domain instead of the time domain thanks to a Fast Fourier Transform (FFT). The DOF spatial resolution is then determined by the frequency range $\boldsymbol{\Delta F}$ depending on the Rayleigh scattering [27] (see section 1.1.2), Brillouin scattering [28], or Raman scattering [29] (see sections 1.1.1 and 1.1.3, respectively).

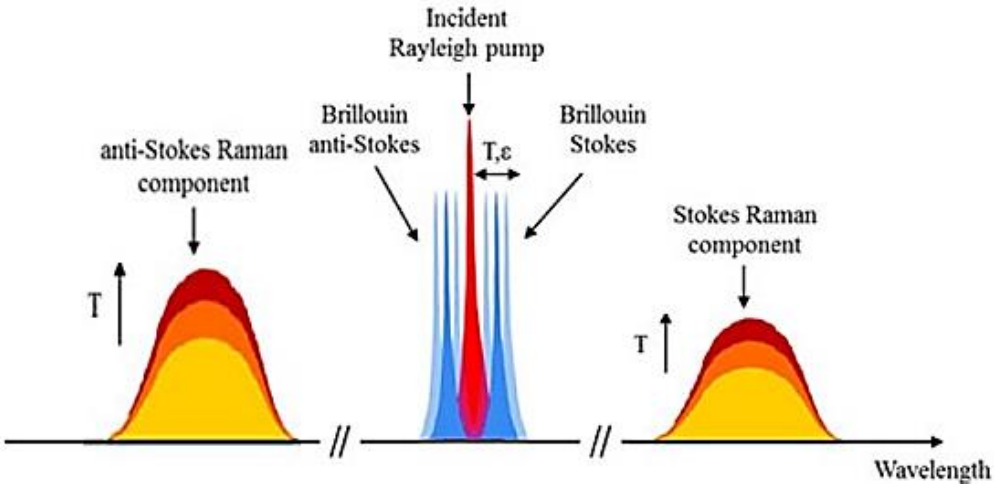

Figure 1.1 Scattering phenomena in silica-based fiber and their strain and/or temperature dependencies [30]

1.1.1 Raman scattering

Raman scattering is an inelastic process meaning that the incident signal wavelength differs from the scattered light wavelength. The phenomenon is represented in Figure 1.2. The incident photon (ω_0) will be absorbed by the virtual state, and the de-excitation results in the emission of a photon at a different wavelength. In terms of energy we will obtain a lowest energy for the Stokes (ω_S) photons and highest energy for the anti-Stokes (ω_{AS}) photons as described in Figure 1.2 a). This phenomenon is explained by the incident light interaction with vibrating molecules in the material. In terms of wavelengths (see Figure 1. 2 b), the lowest wavelength corresponds to the anti-Stokes (λ_{AS}) component and the highest wavelength corresponds to the Stokes (λ_S) one. Moreover, the amplitude of the anti-Stokes component strongly depends on the temperature whereas the Stokes one only weakly depends on it. Equations (1.2) and (1.3) give those temperature dependences of the differential cross section $\frac{d\sigma}{d\Omega}$ for the Stokes and anti-Stokes components [31]:

$$\frac{d\sigma_S}{d\Omega} = \frac{\nu_S^4}{1 - e^{-\frac{h\Delta\nu}{K_B T}}} \tag{1.2}$$

$$\frac{d\sigma_{AS}}{d\Omega} = \frac{\nu_{AS}^4}{e^{\frac{h\Delta\nu}{K_B T}} - 1} \tag{1.3}$$

where ν_S and ν_{AS} are the frequencies of the Stokes and anti-Stokes components, respectively, $K_B$is the Boltzmann constant, T is the temperature, h is the Planck constant, and $\Delta\nu$ is the frequency of the emitted or absorbed phonon and is equal to 1.3×10^{13} Hz for the fused silica.

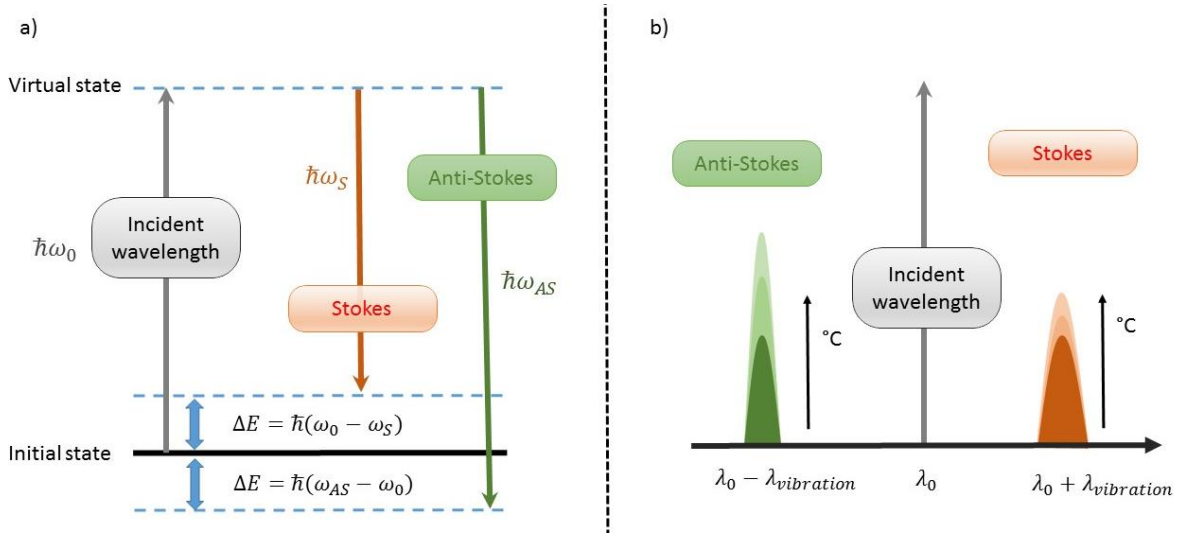

Figure 1.2: Explanation of the spontaneous Raman scattering [32]

By calculating the ratio between the anti-Stokes (I_{AS}) and the Stokes (I_A) backscattered intensities, it is possible to determine the temperature through equation (1.4):

$$R(T,z) = \frac{I_{AS}(z,T)}{I_S(z,T)} = \left(\frac{\nu_{AS}}{\nu_S}\right)^4 e^{-\int_0^z (\alpha(\lambda_{AS},x)-\alpha(\lambda_S,x))dx} \qquad (1.4)$$

where $\alpha(\lambda_{AS},x)$ and $\alpha(\lambda_S,x)$ are the attenuations of the anti-Stokes and the Stokes components at the x position, z corresponding to the fiber length. And then, the measured ratio gives an absolute temperature value at each x position. Two different types of Distributed Temperature Sensor (DTS) have been developed, known as the R-OTDR and the R-OFDR. These sensors will be detailed in the next parts.

1.1.1.1Raman Optical Time Domain Reflectometer: R-OTDR

The most widely used class of DTS operates in the time domain. Figure 1.3 illustrates the typical architecture of a Raman-Optical Time Domain Reflectometer (R-OTDR). A pulsed laser light is launched into the sensing fiber. The Stokes and anti-Stokes backscattered signals pass through an optical circulator. Then, an optical filter separates the two components,

allowing recording the temporal change of their intensities, and then as a function of the fiber distance. The sensor spatial resolution proportionally depends on the laser pulse duration (equation 1.1): typically a 10 ns pulse allows achieving a spatial resolution of 1 m. By using R-OTDR, sensing distance of 100 km is possible [33] with a temperature accuracy of 1 °C, an error of 0.1 °C.

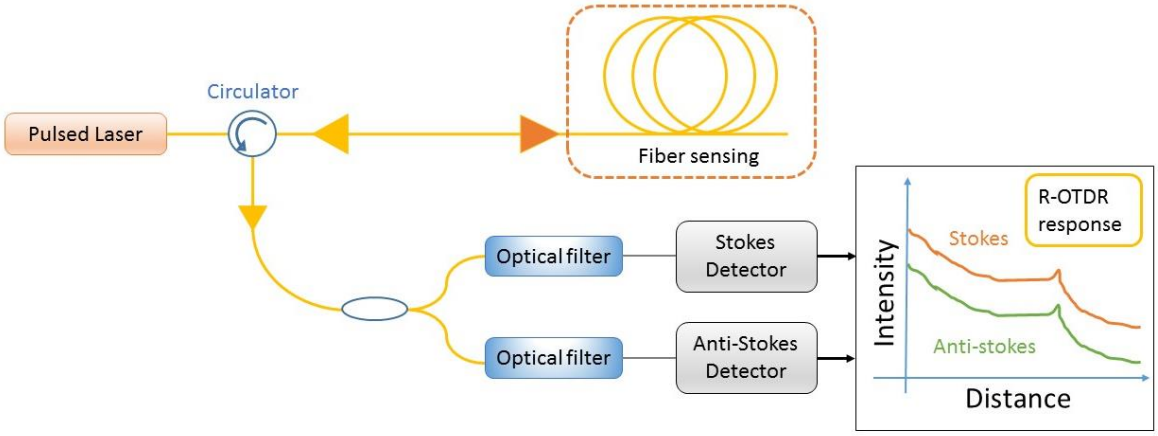

Figure 1.3: Representation of the basic R-OTDR system [34]

1.1.1.2 Raman Optical Frequency Domain Reflectometer: R-OFDR

The second DTS architecture is the Raman-Optical Frequency Domain Reflectometer (R-OFDR). Figure 1.4 describes the R-OFDR system using as the optical source a Continuous Wave (CW) laser which is modulated in intensity by an Electro Optic Modulator (EOM) and a Signal Generator (SG). The backscattered Stokes and anti-Stokes components are separated and detected in function of the SG. The frequency response of the backscattered signal is measured by a Network Analyzer. By applying an Inverse Fast Fourier Transform (IFFT) the time domain response is obtained. The spatial resolution is then driven by the frequency range ΔF given by:

$$\delta z = \frac{c}{2n_{eff}\Delta F} \qquad (1.5)$$

Typically the R-OFDR allows achieving a spatial resolution of 2 m along 30 km of fiber with a temperature resolution of 1.9 °C [35].

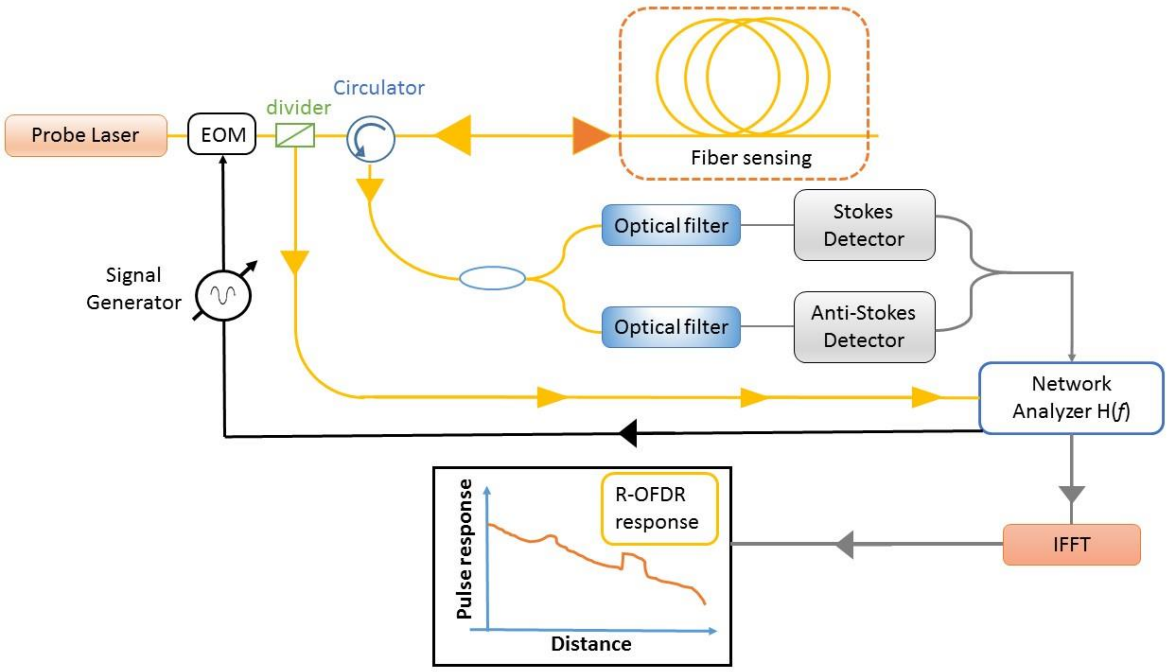

Figure 1.4: Representation of basic R-OFDR system [29]

1.1.2. Rayleigh scattering

1.1.2.1 Optical Time Domain Reflectometer: OTDR

The Rayleigh scattering is an elastic scattering phenomenon [36], it means that the scattered light and the probe laser have the same wavelength. Rayleigh scattering is caused by the random fluctuations of the silica refractive-index of the optical fiber [22]. Moreover, the Rayleigh scattering is the strongest phenomena compared to the Raman and Brillouin scatterings which are always present. By applying an external stimuli, such as strain or temperature, on the fiber, its properties are locally modified in particular its refractive index. Then, by comparing the backscattered Rayleigh levels before and after applying the stimuli, it is possible to monitor this stimuli. Most of the interrogators are designed as Optical Time Domain Reflectometer (OTDR). The OTDR architecture is schematically represented in Figure 1.5. A laser pulse is launched in the optical fiber, the backscattered Rayleigh signal is then monitored. Thanks to the time-of-flight technique, is it possible to determine the position of the event along the fiber through:

$$z = v_\lambda \frac{t}{2} \qquad (1.6)$$

where v_λ is the light velocity in the fiber, z is the position, and t is the time of flight, the factor ½ is explained by the consideration of the return trip of the light. The spatial resolution

depends on the pulse width according to equation (1.1). To perform the temperature measurement, the ratio between the reference trace and the trace of the perturbed fiber is calculated. This ratio linearly depends on the temperature with a typical sensitivity of 0.015 %/°C. Such system then exhibits poor performances with temperature resolution of ~15 °C [37].

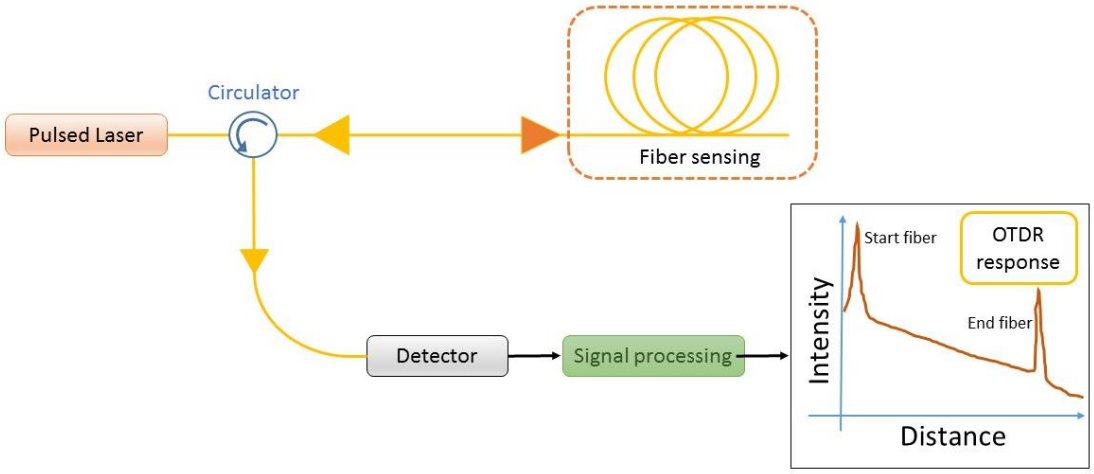

Figure 1.5: representation of simplest OTDR system adapted from [38]

1.1.2.2 Optical Frequency Domain Reflectometer: OFDR

A second technique based on the Rayleigh scattering has been developed and it is called Optical Frequency Domain Reflectometry (OFDR). Its operating principle is represented in Figure 1.6. A tunable laser source (TLS) is used to have a spectral range swept in time. The launching light is split in two parts. The first part goes in the reference arm while the second part goes in the fiber acting as the sensitive element. The backscattered light from the sensing fiber is combined to the light from the reference arm by a coupler in order to generate interferences [39]. The two components of the polarized light are recorded with two detectors, labelled as P and S detectors.

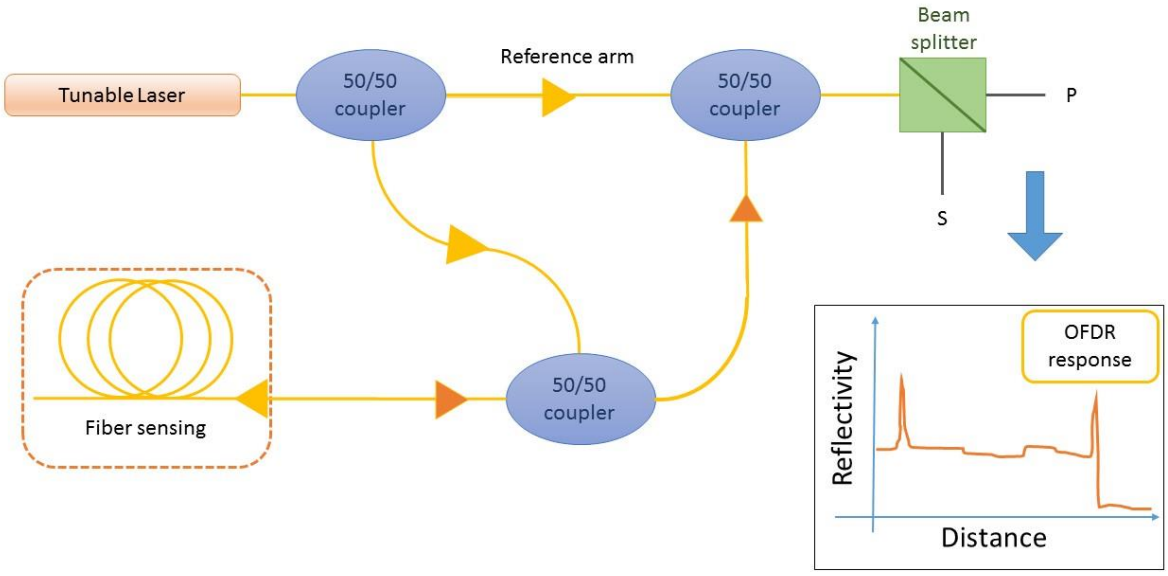

Figure 1.6: Operation principle of the OFDR technologies [39]

To understand the sensing principle, we can analyze a short distance of the fiber, noted as Δx and having its characteristics represented in Figure 1.7. We first perform a reference measurement of the Rayleigh amplitude of the fiber (dashed line). After heating the fiber we record the new trace (solid line). By applying a Fast Fourier Transform (FFT) we obtain the spectra corresponding to the fiber before and after perturbation (Figure 1.7a). Finally, with a cross correlation between the reference and the perturbed signals we obtain a wavelength ($\Delta\lambda$) or frequency shift ($\Delta\nu$) (Figure 1.7 b), this shift being linearly dependent on the strain and the temperature [40]:

$$\frac{\lambda}{\Delta\lambda} = -\frac{\nu}{\Delta\nu} = C_T\Delta T + C_\epsilon\epsilon \qquad (1.7)$$

where λ and ν are the mean optical wavelength and frequency respectively, C_T and C_ε are the temperature and the strain coefficients respectively. By considering Δx= 5 mm, the temperature resolution of the OFDR technologies is of about 0.1 °C and the strain resolution is of about 1 με [41].

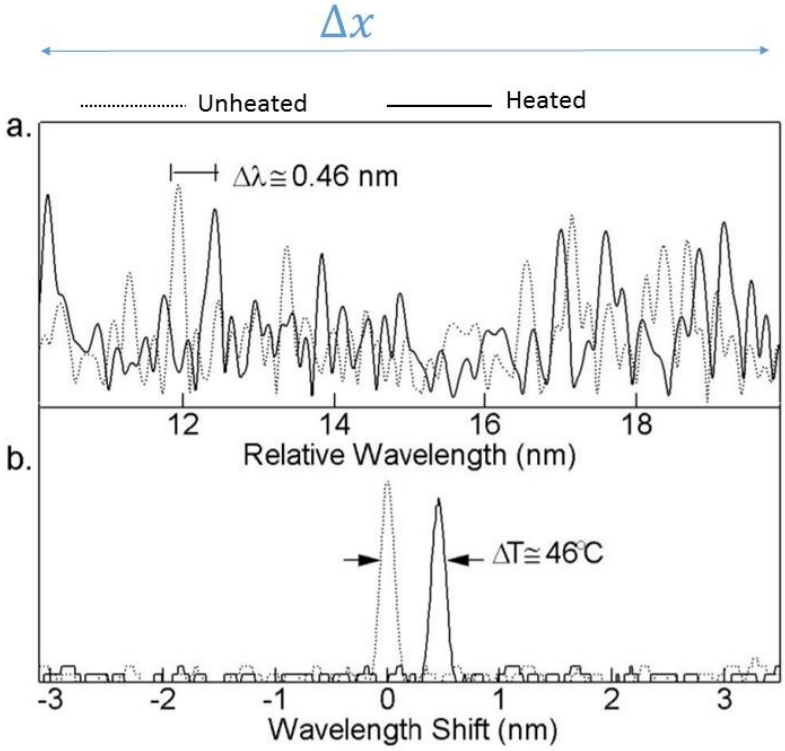

Figure 1.7: Rayleigh response of a short length of a single-mode fiber acting as the sensitive element [41], [42]. The solid line corresponds to the heated fiber (ΔT=46°C, perturbed state) and the dashed line to the unheated fiber (reference state). In a) the wavelength spectra of the unheated and heated sample, in b) the cross correlation of the reference and perturbed spectra between the both measurements

1.1.3 Brillouin scattering

As the Raman scattering, the Brillouin scattering is an inelastic phenomenon. It means that the scattered Brillouin wavelength differs from the one of the probe laser, as illustrated in Figure 1.8. Contrary to Raman case, Brillouin scattering is related to the acoustic waves (phonons) present inside the silica-based fiber due to the thermal activity. Moreover the Brillouin scattering of the silica glass is sensitive to both temperature and strain [43], [44]. The physics of the spontaneous and of the stimulated Brillouin scattering phenomena will then be described in this part. Finally the various interrogator architectures allowing to exploit the fiber Brillouin response to perform distributed temperature and/or strain sensing along an optical fiber will be introduced.

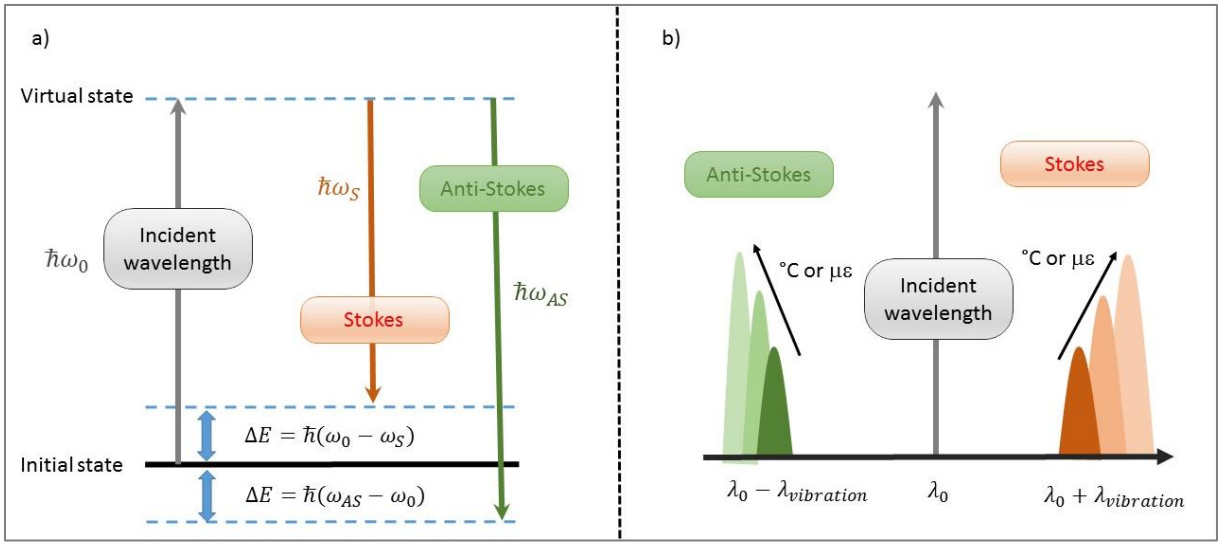

Figure 1.8: Explanation of the spontaneous Brillouin scattering [45]

1.1.3.1 Spontaneous Brillouin scattering

To understand the origins of the Brillouin scattering, we applied the Maxwell equations to the case of a single mode silica-based optical fiber [46]. The silica is a dielectric material meaning that no charges and no currents have to be considered into the Maxwell's equations that can by reduced as:

$$\nabla \times \vec{E} = -\frac{\partial \vec{B}}{\partial t} \quad (1.8)$$

$$\nabla \times \vec{B} = \mu_0 \frac{\partial \vec{D}}{\partial t} \quad (1.9)$$

$$\nabla \cdot \vec{B} = 0 \quad (1.10)$$

$$\nabla \cdot \vec{D} = 0 \quad (1.11)$$

where $\vec{E}$ and $\vec{B}$ are the Electric and the Magnetic fields respectively, μ_0 is the permeability of free space, and $\vec{D}$ represents the electric displacement field through [47]–[49] :

$$\vec{D} = \epsilon_0 \vec{E} + \vec{P} \quad (1.12)$$

with ϵ_0 the dielectric permittivity of free space, and P the polarization density. So, we can define the linear equation of propagation by:

$$\nabla^2 \vec{E} - \frac{n^2}{c^2} \frac{\partial^2 \vec{E}}{\partial^2 t} = 0 \quad (1.13)$$

where n is the refractive index and c the speed of light. In a dielectric media, the following constitutive equation has to be taken into account:

$$\vec{P} = \epsilon_0 \chi \vec{E} \quad (1.14)$$

where χ is the electric susceptibility. By considering the scattering phenomenon the equation (1.14) becomes:

$$\vec{P} = \epsilon_0 \chi \vec{E} + \vec{P}_{NL} \quad (1.15)$$

with

$$\vec{P}_{NL} = \Delta\epsilon \vec{E} \quad (1.16)$$

where $\Delta\epsilon$ is the permittivity tensor of the considered material. By including equation (1.16) in equation (1.13), the propagation equation becomes:

$$\nabla^2\vec{E} - \frac{n^2}{c^2}\frac{\partial^2\vec{E}}{\partial^2 t} = \mu_0\frac{\partial^2\vec{P}_{NL}}{\partial^2 t} \qquad (1.17)$$

The permittivity tensor allows explaining the Brillouin scattering, indeed the tensor could be expressed in two parts, one is scalar while the second is a tensor:

$$\Delta\epsilon_{ik} = \Delta\epsilon\delta_{ik} + \Delta\epsilon_{\mathrm{ik}} \qquad (1.18)$$

where $\Delta\epsilon\delta_{ik}$ corresponding to the scalar depends on the pressure P, the temperature T and the material density ρ, $\Delta\epsilon_{\mathrm{ik}}$ is the tensor describing the Rayleigh wings as well as the Raman scattering. The scalar part $\Delta\epsilon\delta_{ik}$ is at the origin of the Brillouin and the Rayleigh scatterings, it depends on the elastic properties. The variation of the dielectric constant can be described as:

$$\Delta\epsilon = \left(\frac{\partial\epsilon}{\partial\rho}\right)_T \Delta\rho + \left(\frac{\partial\epsilon}{\partial T}\right)_\rho \Delta T \qquad (1.19)$$

The variations of the permittivity induced by the temperature remains low, below 2%. Then we can consider only the first term of second part of the equation (1.19). The density depends on the entropy S and on the pressure P, the variation can be expressed as:

$$\Delta\rho = \left(\frac{\partial\rho}{\partial P}\right)_S \Delta P + \left(\frac{\partial\rho}{\partial S}\right)_P \Delta S \qquad (1.20)$$

The right part of the second term explains the Rayleigh scattering while the other term corresponds to the Brillouin scattering. So we can summarize the equation (1.19) by including the equation (1.20) and considering only the Brillouin contribution:

$$\Delta\epsilon = \frac{\partial\epsilon}{\partial\rho}\left(\frac{\partial\rho}{\partial P}\right)_S \Delta P \qquad (1.21)$$

In the case of the optical fibers, the Brillouin scattering is due to the variation of pressure which is explained by the acoustic wave. This acoustic wave corresponds to a local variation of the density through:

$$\rho(z,t) = \rho_0 + \Delta\rho(z,t) \tag{1.22}$$

where ρ_0 is the average density of the material and could be defined by wave equation as:

$$\Delta\rho(z,t) = \frac{1}{2}A(z,t)e^{j(\Omega t - qz)} + c.c \tag{1.23}$$

with A being its amplitude, Ω is the pulsation, q the wave vector, and c.c is the complex conjugate. By considering the effect of the acoustic wave in the polarization density as well as the scalar approximation, P_{NL} becomes:

$$P_{NL}(r,t) = \frac{\partial\epsilon}{\partial\rho}\Delta\rho(z,t)E(r,t) \tag{1.24}$$

We can define:

$$\gamma = \rho_0\frac{\partial\epsilon}{\partial\rho} = n^4\epsilon_0 p_{12} \tag{1.25}$$

where γ is the coefficient of electrostriction, and p_{12} the elasto-optic coefficient defined in chapter 2.

We define the Electro Magnetic (EM) wave through:

$$\vec{E}(r,t) = \vec{e}_p\frac{1}{2}E_0 e^{j(\omega_0 t - kz)} + c.c \tag{1.26}$$

where ω_0 is the angular frequency, k is the wave vector, E_0 the amplitude, and $\vec{e}_p$ is the unit vector of polarization. So by including the equations (1.23) and (1.26) in the P_{NL} we can define the electronic polarization as:

$$\vec{P}_{NL}(r,t) = \vec{e}_p\frac{\gamma}{4\rho_0}\left[AE_0 e^{j((\omega_0+\Omega)t-(k+q)z)} + A^*E_0 e^{j((\omega_0-\Omega)t-(k-q)z)}\right] + c.c \tag{1.27}$$

and then we can define the propagation equation defining the spontaneous Brillouin scattering as [47]:

$$\nabla^2 E - \frac{n^2}{c^2}\frac{\partial^2 E}{\partial^2 t} = e_p \frac{\mu_0 \gamma}{4\rho_0}\left[(\omega_0+\Omega)^2 A E_0 e^{j((\omega_0+\Omega)t-(k+q)r)} + (\omega_0-\Omega)^2 A^* E_0 e^{j((\omega_0-\Omega)t-(k-q)r)}\right] + c.c \quad (1.28)$$

The Brillouin scattering is said as spontaneous when the variation of density (acoustic wave) is due to the thermal activity. It is important to note that two terms in the equation define two new spectral components. Indeed $(\omega_0 + \Omega)$ and $(\omega_0 - \Omega)$ demonstrate clearly the phenomenon shown in Figure 1.8, where $(\omega_0 + \Omega)$ and $(\omega_0 - \Omega)$ represent the Anti-Stokes and the Stokes components, respectively.

1.1.3.2 Stokes component

As reported in Figure 1.9, the first component of the Brillouin scattering is the Stokes one. In particular, $\vec{k}_s$ represents the wave number of the Stokes component (orange arrow), $\vec{k}_p$ (blue arrow) and $\vec{q}$ (green arrow) are the wave numbers of the incident light and the acoustic wave, respectively. Λ_a represents the wavelength of the acoustic wave. The yellow part represents the modulation of acoustic wave, and then the modulation of the material density. The equation (1.28) requires that, for the Stokes component, the wave number and the pulsation follow the equations (1.29) and (1.30) corresponding to the momentum and energy conservations, respectively:

$$\vec{k}_s = \vec{k}_p - \vec{q} \quad (1.29)$$

$$\omega_s = \omega - \Omega \quad (1.30)$$

The frequency of the Stokes component depends on the angle θ between the incident optical wave and the acoustic wave. Moreover the acoustic wave frequency is small compared to the one of optical wave, then we can do the approximation that $k_S \approx k_P$. Then by satisfying the equations (1.29) and (1.30) we can write:

$$q = 2k_p \sin\left(\frac{\Theta}{2}\right) \quad (1.31)$$

and then by using the equations of dispersion: $k = \frac{\omega}{C}$ and $q = \frac{\Omega}{V_a}$, the equation (1.31) becomes:

$$\Omega = 2k_p V_a \sin\left(\frac{\Theta}{2}\right) \tag{1.32}$$

where V_a is the speed of the acoustic wave. The frequency Ω is generally known as the Brillouin shift. Throughout this PhD thesis, this parameter will be called Brillouin frequency (ν_B) to avoid confusion with the Brillouin shift induced by the temperature and/or strain. The equation (1.32) could be expressed in function of the incident optical wavelength as:

$$\nu_B = \frac{2nV_a}{\lambda_0} \sin\left(\frac{\Theta}{2}\right) \tag{1.33}$$

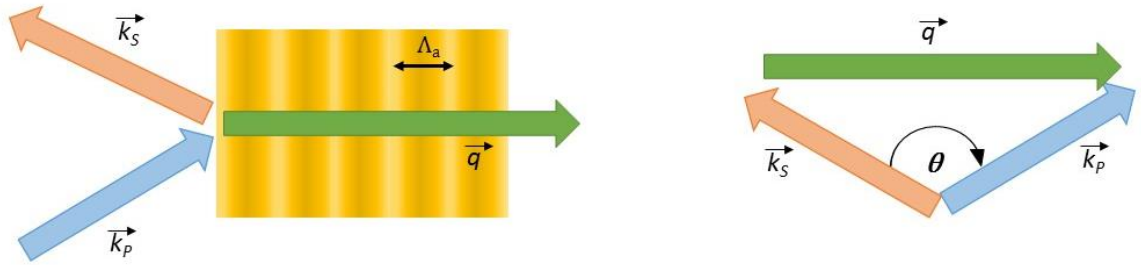

Figure 1.9: Representation of the Stokes component scattered by the spontaneous Brillouin phenomenon. k_s corresponds to the wave number of Stokes component, k_P and q, the wave numbers of the incident wavelength and the acoustic wave respectively. Λ_a is the wavelength of the acoustic wave[47].

Into an optical fiber, the light can only be guided in two opposite directions. So the angle θ can take only two values: θ=0 ° or θ=180 °. So by considering the equation (1.33) the scattered light is null in the direction of propagation and maximum in the opposite direction. Considering the backscattered phenomenon used in the Brillouin Optical Time Domain Reflectometer (BOTDR) interrogators equation (1.33) could be simplified as:

$$\nu_B = \frac{2nV_a}{\lambda_0} \tag{1.34}$$

1.1.3.3 Anti-Stokes component

Such as the Stokes component, the Anti-Stokes component must follow the momentum and the energy conservations, and then by considering the equation (1.28) we obtain:

$$\vec{k}_{As} = \vec{k}_p + \vec{q} \tag{1.35}$$

$$\omega_{As} = \omega_0 + \Omega \tag{1.36}$$

Figure 1.10 represents the Anti-Stokes wave scattered by the Brillouin scattering. Moreover, frequency shift is the same as the Stokes component. This approach allows demonstrating the variation of frequency between the incident light and the scattered one as it has been described in Figure 1.8.

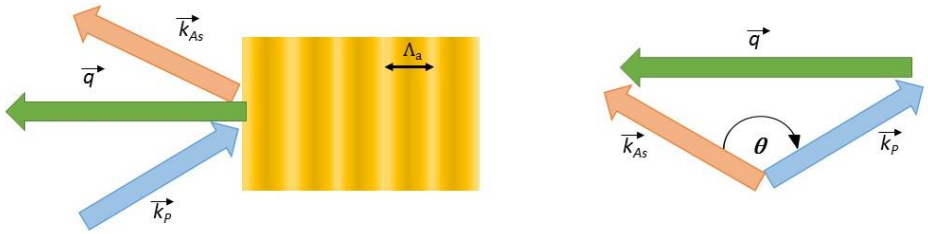

Figure 1.10: Representation of the Anti-Stokes component scattered by the spontaneous Brillouin phenomenon. k_{As} corresponds to the wave number of Stokes component, k_P and q, the wave numbers of the incident wavelength and the acoustic wave respectively. Λ_a is the wavelength of the acoustic wave[50].

1.1.4 Stimulated Brillouin scattering

In the case of the Stimulated Brillouin Scattering (SBS) the equations characterizing the Spontaneous Brillouin scattering are still valid, but by adding another optical wave referred as the "pump wave" the Brillouin scattering intensity is increased. Indeed, the Brillouin scattering exhibits a lower intensity than the Rayleigh one. Using this pump wave allows increasing the number of acoustic phonons (acoustic waves) and then achieving a higher intensity of Brillouin scattering. In the case of optical fiber, implementing the pump wave will create an electrostriction phenomenon.

1.1.4.1 Electrostriction

The electrostriction happens when a pump wave and a probe wave are simultaneously launched in the optical fiber. Figure 1.11 details this phenomenon: by launching an optical probe wave in the single mode fiber, a Stokes wave will be backscattered (red line) as explained in part 1.3.2. Simultaneously, by launching a pump wave, these two waves will interfere creating an electromagnetic beat with a frequency ν_B at a speed equal to the acoustic wave. The Electrostriction will create a pressure wave which increases the acoustic wave and then reinforces the Brillouin scattering.

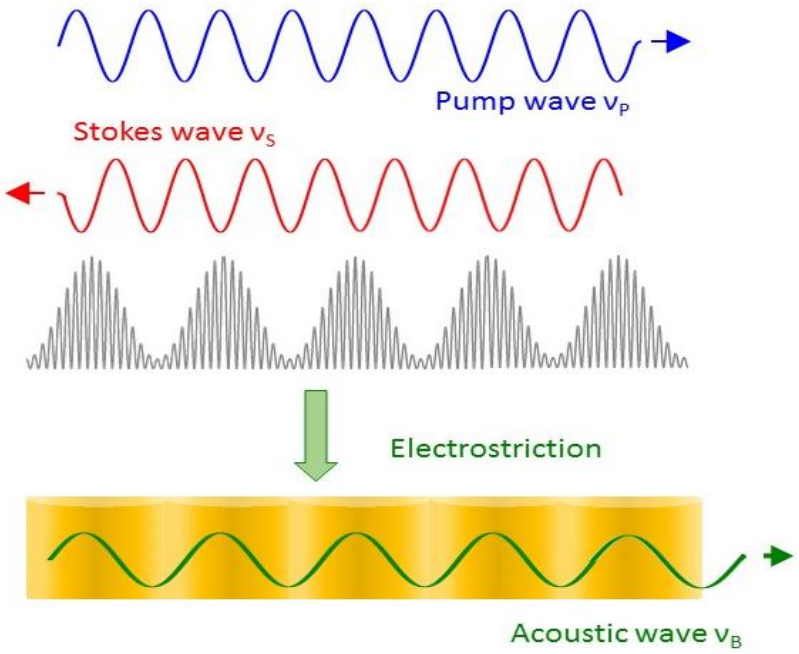

Figure 1.11: Electrostriction phenomenon

This phenomenon will be played on a loop, as shown in Figure 1.12, and the amplitude of the pump wave will decrease while the one of the Stokes wave increases.

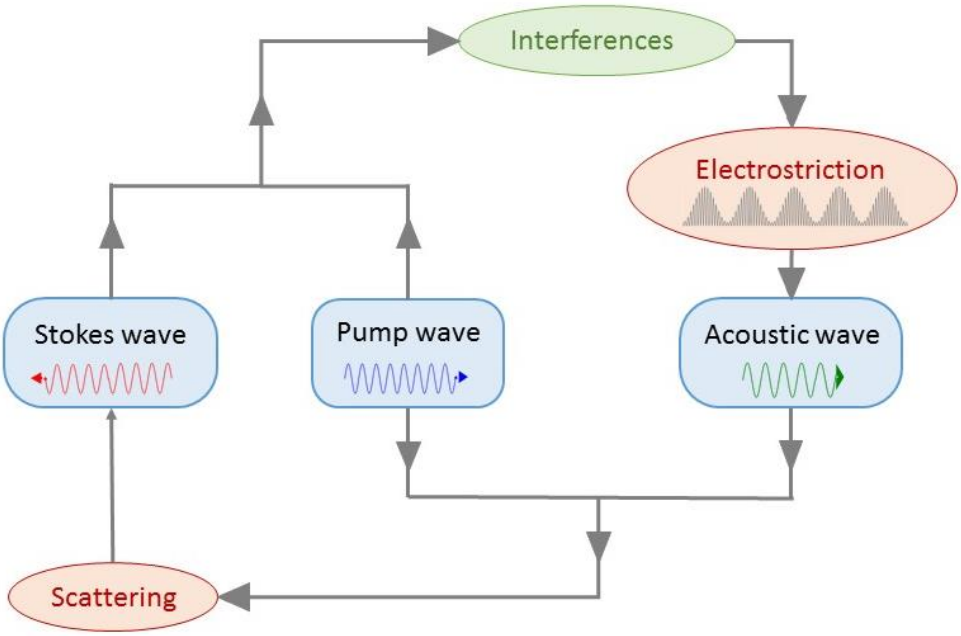

Figure 1.12: Principle of the SBS [46]

1.1.4.2 Equation of Stimulated Brillouin Scattering

In the case of SBS, and then with the presence of electrostriction phenomenon, three waves are present: the Stokes wave E_S, the pump wave E_P, and the acoustic wave or pressure wave $\Delta\rho$:

$$\vec{E}_P(r,t) = \vec{e}_p \frac{1}{2} E_P(z,t) e^{j(\omega_P t - k_p z)} + c.c \quad (1.37)$$

$$\vec{E}_S(r,t) = \vec{e}_p \frac{1}{2} E_S(z,t) e^{j(\omega_S t + k_S z)} + c.c \quad (1.38)$$

$$\Delta\rho(r,t) = \frac{1}{2} A(z,t) e^{j(\Omega t - qz)} + c.c \quad (1.39)$$

Due to the interference, and then the electrostriction, the polarization unit vector e_p is the same for the Stokes and pump wave. To define the propagation equations of the pump and the Stokes waves, the polarization density (as defined for the spontaneous Brillouin scattering) has to be taken into account:

$$\vec{P}_{NL}^{P}(r,t) = \vec{e}_p \frac{1}{2} \frac{\gamma}{\rho_0} A(z,t) E_S(z,t) e^{j(\omega_P t - k_P z)} + c.c \quad (1.40)$$

$$\vec{P}_{NL}^{S}(r,t) = \vec{e}_p \frac{1}{2} \frac{\gamma}{\rho_0} A^*(z,t) E_P(z,t) e^{j(\omega_S t + k_S z)} + c.c \quad (1.41)$$

Concerning the SBS, the acoustic phonons originate from the electrostriction and their amplitude depends on the intensity of the beat created by the Stokes and pump waves. So the polarization depends on the optical intensity, this dependence explains that the SBS is a non-linear optical effect. The equations of the perturbed wave and the acoustic wave can be defined as:

$$\nabla^2 E_P - \frac{n^2}{c^2} \frac{\partial^2 E_P}{\partial^2 t} = \mu_0 \frac{\partial^2 P_{NL}^P}{\partial^2 t} \quad (1.42)$$

$$\nabla^2 E_S - \frac{n^2}{c^2} \frac{\partial^2 E_S}{\partial^2 t} = \mu_0 \frac{\partial^2 P_{NL}^S}{\partial^2 t} \quad (1.43)$$

$$\frac{\partial^2 \Delta\rho}{\partial^2 t} + 2\Gamma_B \frac{\partial \Delta\rho}{\partial t} - V_a^2 \nabla^2 \Delta\rho = -\nabla \cdot F \quad (1.44)$$

where F represents the force of Electrostriction, and Γ_B is the damping factor acoustic.

An approximation can be applied to simplify the equations (1.42)-(1.44). In the case of low interaction, the involved waves do not evolve along a distance corresponding to a few wavelengths or during a few periods of oscillation. This approximation corresponds to the *slowly varying envelope approximation* and allows removing the second derivate term. Under this approximation, the equations (1.42)-(1.44) become:

$$\left(\frac{\partial}{\partial z}+\frac{n}{c}\frac{\partial}{\partial t}+\frac{\alpha}{2}\right)E_P=-\frac{jk_P\gamma}{4\epsilon\rho_0}AE_S e^{j\Delta kz} \tag{1.45}$$

$$\left(\frac{\partial}{\partial z}-\frac{n}{c}\frac{\partial}{\partial t}+\frac{\alpha}{2}\right)E_S=\frac{jk_S\gamma}{4\epsilon\rho_0}A^*E_P e^{-j\Delta kz} \tag{1.46}$$

$$\left(\frac{\partial}{\partial z}+\frac{\Gamma_B}{V_a}+\frac{\Omega-j\Gamma_B}{\Omega V_a}\frac{\partial}{\partial t}\right)A=-\frac{jq\gamma}{4V_a^2}E_S E_P e^{-j\Delta kz} \tag{1.47}$$

where α is the linear optical attenuation of the fiber, the right part of the equation (1.47) corresponds to the $-\nabla\cdot F$and where F is defined as $F=\frac{1}{2}\gamma\nabla\mathrm{E}^2$ before the slowly varying envelope approximation, and Δk is introduced when the resonance exists but with an acoustic frequency slightly different than the Brillouin frequency. Finally, Δk is defined through:

$$\Delta k=k_P+k_s-q\ \approx 0 \tag{1.48}$$

but Δk is still small, and could be translated in frequency as:

$$\Delta\nu=\nu_S-(\nu_P-\nu_B)\approx 0 \tag{1.49}$$

The principal interest of the SBS is the amplification of the Brillouin signal. The amplification factor is called the Brillouin gain: g_B. This term appears in the two differential equations of E_S and E_P, indeed by defining the amplitude of the acoustic waves through the equations (1.50) as stationary wave, we obtain the equations (1.51) and (1.52) [47]:

$$A(z)=-\frac{jq\gamma}{4\Gamma_B V_a}E_P E_S^*\frac{e^{-j\Delta kz}}{1-j(2\Delta\nu/\Delta\nu_B)} \tag{1.50}$$

$$\frac{dE_P}{dz}=-\frac{qk_P\gamma^2}{16\epsilon\Gamma_B V_a\rho_0}\frac{E_P|E_S|^2}{1-j\left(\frac{2\Delta\nu}{\Delta\nu_B}\right)}-\frac{\alpha}{2}E_P \tag{1.51}$$

$$\frac{dE_S}{dz} = -\frac{qk_P\gamma^2}{16\epsilon\Gamma_B V_a\rho_0}\frac{E_S|E_P|^2}{1-j\left(\frac{2\Delta\nu}{\Delta\nu_B}\right)} + \frac{\alpha}{2}E_S \tag{1.52}$$

If we define the intensity and the electric field in terms of intensity as:

$$I = \frac{n\epsilon_0 c_0}{2}|E|^2 \tag{1.53}$$

$$E_P(z) = \sqrt{\frac{2}{n\epsilon_0 c_0}I_P(z)} \tag{1.54}$$

$$E_s(z) = \sqrt{\frac{2}{n\epsilon_0 c_0}I_S(z)} \tag{1.55}$$

the equation of intensity of the SBS can be obtained:

$$\frac{dI_P}{dz} = -g_B(\nu)I_P I_S - \alpha I_P \tag{1.56}$$

$$\frac{dI_S}{dz} = -g_B(\nu)I_P I_S + \alpha I_S \tag{1.57}$$

with the gain is defined as:

$$g_B = 2\,\frac{qk\gamma^2}{16\epsilon\Gamma_B V_a\rho_0}\frac{2}{n\epsilon_0 c_0} = \frac{2\pi n^7 p_{12}}{c_0\lambda_P^2\rho_0 V_a\Delta\nu_B} \tag{1.58}$$

$$g_B(\nu) = g_B\frac{(\Delta\nu_B/2)^2}{\Delta\nu^2 + (\Delta\nu_B/2)^2} \tag{1.59}$$

where λ_P is the wavelength of the pump wave, and $\Delta\nu_B$ is the Full Width at Half Maximum (FWHM). Finally, for fiber case, only the SBS Stokes component is amplified while the Anti-Stokes is annihilated. Indeed, for the SBS, the number of acoustic phonons which propagate in the same direction as the pump wave increases. This phenomenon increases the amplitude of the Stokes wave. But when an Anti-Stokes photon is created, a photon of the pump wave and a phonon of the acoustic wave (in counter propagation of pump wave) will be annihilated. Then by creating Anti-Stokes photons, the number of acoustic phonons responsible for the creation of Anti-Stokes photon is reduced. This last will be played on loop, and the population of the acoustic phonons becomes rapidly null. This is why the sole Stokes component is represented in Figure 1.13.

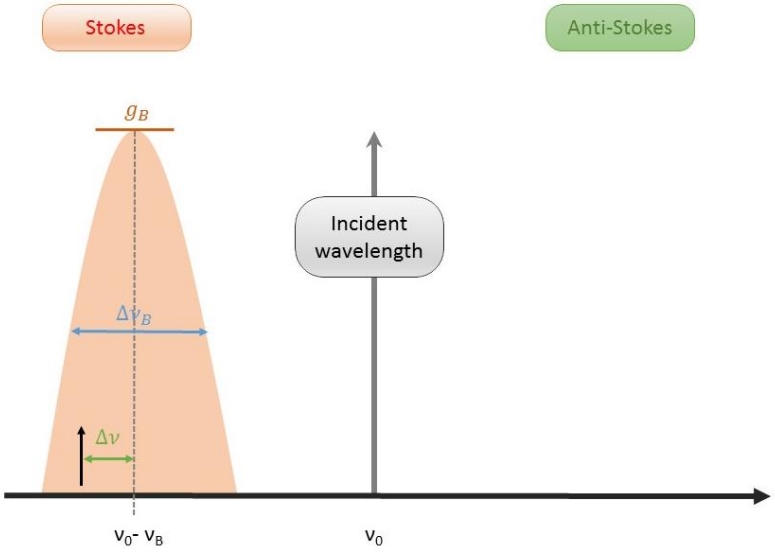

Figure 1.13: Stokes component amplification in the SBS regime

1.1.5 Interrogator

The Brillouin scattering, has been used to monitor the temperature and/or strain using optical fiber. Indeed the Brillouin scattering properties linearly depend on both stimuli [51] through the equation (1.60):

$$\nu_B = C_T T + C_\epsilon \epsilon \qquad (1.60)$$

with C_T and C_ϵ the temperature and strain coefficients, typically for the well-known SMF28 fiber those coefficients are equal to: $C_T = 1MHz/°C$ and $C_\epsilon = 0.05MHz/\mu\epsilon$. Different types of interrogators based on the Brillouin scattering have been developed such as the BOTDR, BOTDA, or the BOFDR (detailed in parts 1.1.5.1, 1.1.5.2, and 1.1.5.3, respectively). Some of them exploit the spontaneous Brillouin scattering while the others are based on the SBS. Each interrogator architecture presents its own advantages and limitations.

1.1.5.1 Brillouin Optical Time Domain Reflectometer: BOTDR

The first kind of interrogator is the Brillouin Optical Time Domain Reflectometer (BOTDR). Figure 1.14 illustrates the principle of operation of this interrogator that is based on the spontaneous Brillouin scattering. A laser pulse is launched in the fiber serving as the sensitive element, part of this laser light is backscattered in Stokes component. This signal is detected and a spectrum analyzer allows measuring the Brillouin frequency. By using a pulsed light it is possible to measure the Brillouin frequency as a function of the fiber distance. The spatial resolution depends on the pulse duration: typically a pulse width of 10 ns allows achieving a spatial resolution of 1 m. The principal advantage of BOTDR is that the sensor is single-ended meaning that to perform the measurement only one end fiber access is required. However, its main limitation of the BOTDR system remains the accessible sensing length. As the signal is not amplified a BOTDR system typically permits to have a sensing length of up to 50 km.

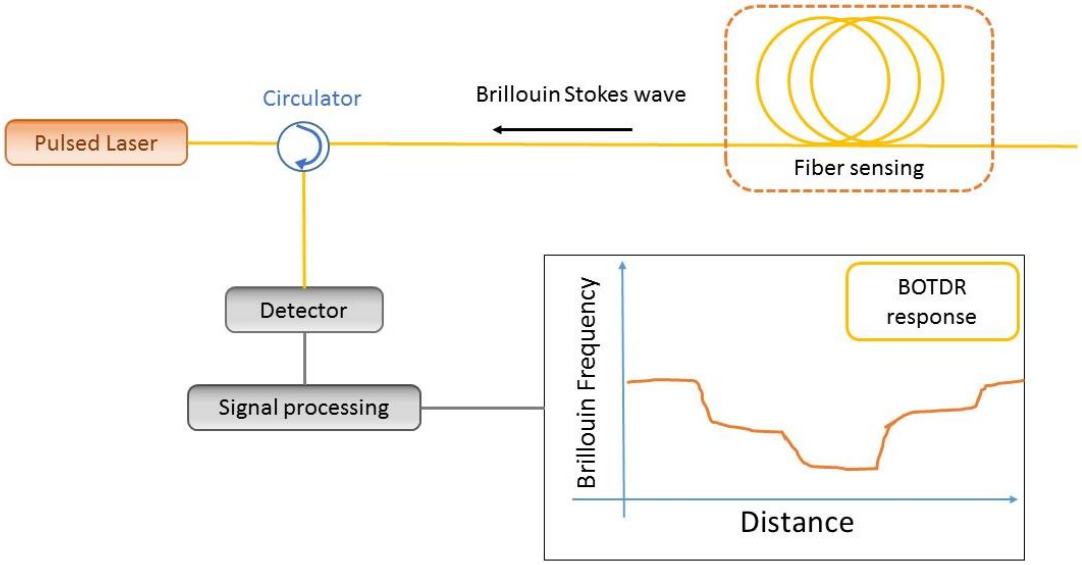

Figure 1.14: Principle of the BOTDR interrogator[52]

1.1.5.2 Brillouin Optical Time Domain Analysis: BOTDA

The second architecture is the Brillouin Optical Time Domain Analysis (BOTDA). Figure 1.15 illustrates its operation principle that is based on the stimulated regime of Brillouin scattering. It is worthwhile to note that two light sources have to be launched in the fiber serving as the sensitive element. The first one is a pulsed laser allowing to achieve the spatial localization (equation (1.1)) while the second one is a CW laser that is used to obtain a Brillouin gain. When the condition $\nu_{probe} - \nu_{pump} = \nu_B$ is satisfied, the backscattered light is detected and analyzed to obtain the distribution on the Brillouin frequency along the fiber. Two types of BOTDA exist, the first one measures the gain of the Stokes component. For this configuration the probe laser is pulsed and operates at low power while the pump signal is continuous and more powerful [53]. The second case consists in measuring the losses of the pump signal. In this case the pump laser is pulsed while the probe laser is CW [54]. The biggest advantage of the BOTDA is obviously that very long sensing length (~100 km) can be monitored thanks to the SBS regime. However, the main BOTDA limitation remains its double-ended configuration. Different researches (such as [55]) have developed some architectures allowing to operate it through a single ended configuration with only one optical source. By using an electro-optic amplitude modulator it is possible to create both the probe and the pump from the same source by performing a temporal shift.

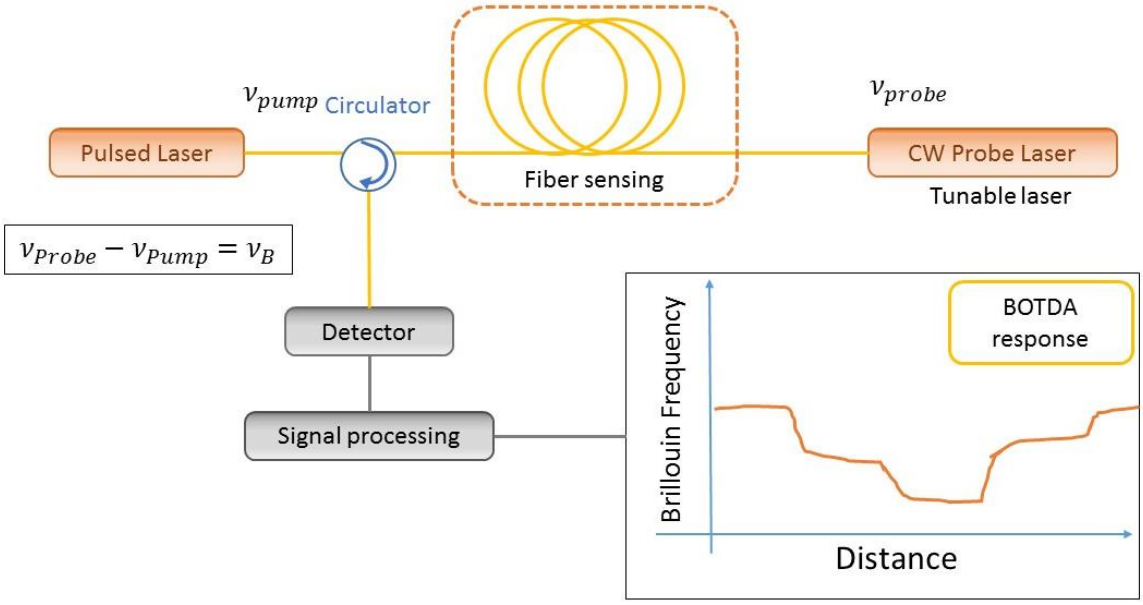

Figure 1.15: Principle of the BOTDA interrogator[24]

1.1.5.3 Brillouin Optical Frequency Domain Reflectometer: BOFDR

The last class of Brillouin interrogator is the Brillouin Optical Frequency Domain Analyzer (BOFDA). BOFDA operates in the frequency domain and then achieves better spatial resolution than BOTDR or BOTDA configurations. Figure 1.16 represents the schematic principle of the BOFDA interrogator. In this case, the probe laser signal is amplitude-modulated by a sinusoidal frequency, the transfer function is subjected to a Fast Fourier Transform to obtain the time response of the system. The spectra along the fiber is determined trace-by-trace by modifying the frequency between the pump and the probe. The BOFDA spatial resolution is defined by the covered frequency range (equation (1.5)), but the sensing length remains limited by the frequency resolution, this point representing today its major limitation [46]. Actually the performance of the BOFDA remains limited compared to the ones of the BOTDA, and as a consequence, these sensors are not today really implemented in the application field.

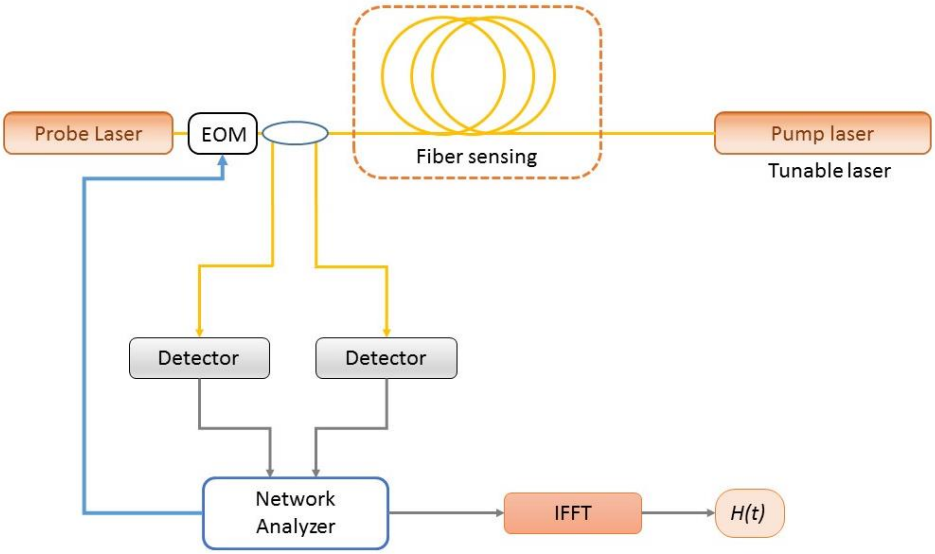

Figure 1.16: Principle of the BOFDA interrogator [28]

TABLE 1.1 summarizes the characteristics of the different commercially-available DOFSs systems. This table explains the orientations and choices made for this PhD thesis work. As IXblue photonics is a company specialized in the tracking and positioning underwater by acoustic techniques, including the offshore market, it was then decided to search for a technology allowing long distances monitoring. Moreover, our objective is that the developed sensor will be able to discriminate between the relative effects of the strain and of the

temperature. This discrimination will be achieved by optimizing the sensing properties of the fiber, basing our study on an approach coupling simulations and experiments. Naturally the research has been oriented on the Brillouin–based sensors, as this phenomenon is sensitive to both the temperature and strain. Using a BOTDA, these two measures can be monitored along distances as long as 100 km with good performances.

TABLE 1.1: CHARACTERISTICS OF THE MAIN DOFSS SYSTEMS [22], [33], [56], [57]

Scattering phenomenon	Technique	Spatial resolution	Sensing range	Temperature accuracy	Strain accuracy	Calibration
Rayleigh	OTDR	1 m	100 km	15 °C	-	Relative measurement
	OFDR	From 1 cm down to 10 µm	From 2 km down to 10 m	0.1 °C	1 µε	Relative measurement ➔ a reference is needed
Brillouin	BOTDR	1 m	20-50 km	10 °C	60 µε	Absolute measurement
	BOTDA	50 cm	100 km	1 °C	20 µε	Absolute measurement
	BOFDA	3 cm	10 m	0.3 °C	10 µε	Absolute measurement
Raman	ROTDR	1 m	100 km	1 °C	-	Relative measurement
	ROFDR	1 m	2.5 km	0.1 °C	-	Relative measurement

1.1.5.4 Recent progresses in Brillouin-based sensing

During this last decade, a lot of progresses have been performed in terms of Brillouin-based sensors for structural health monitoring, the oil and gas industry, etc. The advantages of the DOFs based on the Brillouin scattering are their high temperature and strain sensitivities, and the possibility to monitor long distances. However, the Brillouin DOFs can still be optimized, overcoming the current limitations has been the subject of numerous researches. The first progress concerns the sensing length [49] which, at the start, was 1.2 km (100 m spatial resolution) [24]. Actually with standard BOTDA is it possible to obtain a sensing length of 100 km (1 m spatial resolution) [58]. After that, another technology appeared, called the Brillouin Optical Correlation Domain Analyzer (BOCDA) which allows obtaining a spatial resolution of a few centimeters but for a reduced sensing length [59]. To keep the fiber length over several kilometers, the next idea to improve the spatial resolution is to use several laser pulses instead of one. The DPP-BOTDA (DPP means Differential Pulse Pair) has then been proposed [60]. By playing with the coding and decoding of the laser pulses, sub-metric spatial resolution has been investigated: typically a resolution from 2 cm to 2 m can be obtained for a fiber length of 2 km or 150 km, respectively [61], [62].

Another way of improvement concerns the acquisition time of Brillouin interrogators. Today usual Brillouin interrogators perform a distributed measurement over 150 km of fiber in about 5 min with a spatial resolution of 2 m. In the same time, the temperature and strain measurement accuracies have been improved. By increasing the Signal to Noise Ratio (SNR), the sensitivity of the detector, and the frequency step, the detection precision of the Brillouin peak has been improved. Actually commercial DOFSs have a resolution of 0.1 MHz allowing to reach temperature and strain accuracies of about 1 °C and 2 με respectively.

Finally another big challenge for DOFSs remains the discrimination between the relative time evolutions of the temperature and the strain along the fiber. This subject has been studied intensively in the recent years. Different solutions have been proposed, such as coupling two interrogators based on either Raman and Brillouin scatterings or Rayleigh and Brillouin scatterings. Other techniques have been proposed by working at the fiber level: by using two different optical fibers, polarization maintaining optical fibers (PMF), or sapphire fibers [11], [63]. The most interesting solutions will be detailed in the second part of this chapter. By analyzing them, a decision was done on the solutions that have been investigated during this PhD thesis to discriminate between temperature and strain, while keeping low-attenuation optical fiber to preserve the capacity to probe long distances. The developed solution should also be compatible with commercial BOTDA or BOTDR interrogators.

1.2. Towards the strain and temperature discrimination

As explained along this chapter, reflectometers exploit the light scattering dependence on temperature and strain phenomenon in optical fiber to provide distributed measurements of these parameters. Is it possible to determine the amplitude of one of these two stimuli if the other one is kept under control. Otherwise, it is not possible with the current sensor architectures. Indeed, for the OTDR, we measure the linear attenuation of the fiber, for the OFDR, we measure the Rayleigh spectral shift, and for the BOTDR or BOTDA, we measure the Brillouin frequency peak. Then in the case of DOFSs based on Brillouin or Rayleigh scatterings we have one equation [22], [45] for two unknowns (temperature T and strain ϵ) , as described by the equation (1.60) for the DOFSs based on the Brillouin scattering.

To solve the problem of discrimination we must have a system of at least two equations. To obtain this system, different solutions have been proposed.

1.2.1 Using two fibers

The first solution consists in combining two optical fibers which are probed by a unique DOFS interrogator. Figure 1.17 illustrates this principle of discrimination. The idea is simple but more complex to implement: one of the two fibers has to be mechanically isolated while the second one is "free". The first fiber will then be only sensitive to the temperature while the second one will be sensitive to both temperature and strain [63]. Thanks to this approach, a new set of equations allowing discriminating between the temperature and the strain is obtained:

$$\begin{cases} \nu_1 = C_{T1}T + D \\ \nu_2 = C_{T2}T + C_{\epsilon 1}\epsilon \end{cases} \tag{1.61}$$

where ν_1 and ν_2 are the Brillouin frequency peaks of the fibers 1 and 2 respectively, C_{T1} and C_{T2} are their temperature coefficients, $C_{\epsilon 1}$ is the strain coefficient of fiber 2, and D is a constant due to the strain caused by the packaging of fiber 1.

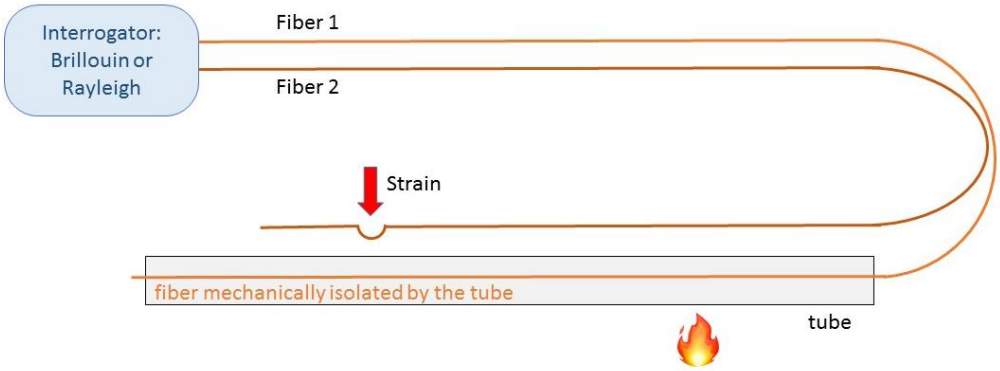

Figure 1.17: Principle of discrimination by two optical fibers

This solution is efficient, but necessitates to use two optical fibers rendering complex its implementation. The worst inconvenient is that this solution is not adaptable to all types of Brillouin or Rayleigh interrogators. Indeed, two inputs are needed for the both fibers. Moreover, in the case of SBS a double-ended interrogator is needed which complicates the setting up of the interrogator. Nevertheless, this system is still commonly used as its capacity of discrimination and sensing length is excellent and as it relies on telecom-grade fibers.

1.2.2 Interrogator

A second discrimination solution has been adopted by working at the interrogator level, keeping a unique optical fiber. Indeed we can find interrogators from Viavi-solutions [64], Neubrex [65], or Febus [66] which are using two different scattering phenomena to solve the discrimination issue. Figure 1.18 illustrates the principle of this discrimination method, choosing to use the Rayleigh and Brillouin scatterings [67], [68]. This solution presents good discrimination capacities [69] exploiting both scatterings to obtain a system of two equations. Another approach has been developed such as combination of Raman and Brillouin [70].

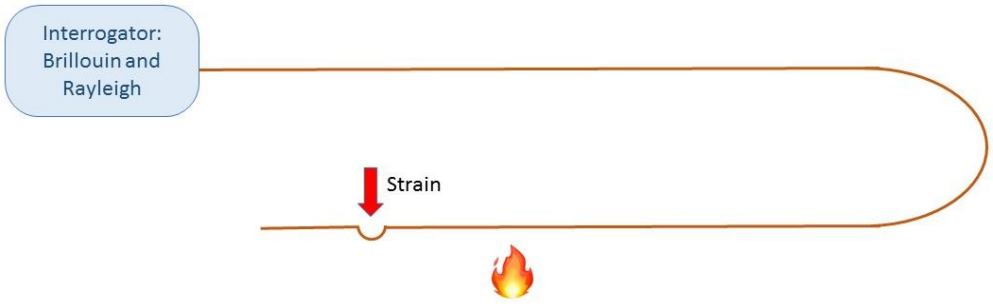

Figure 1.18: principle of discrimination between strain and temperature by using two scattering phenomena

Another technique has been developed by Viavisolutions during this PhD thesis work. Their interrogator, called DTSS for Distributed Temperature Strain Sensor, is based on the measurements of both the Landau-Placzek Ratio (LPR) and the Brillouin frequency peak. During this PhD thesis, a collaboration with Viavi-solutions has been possible and we have tested the performances of their interrogator in harsh environment comprising radiation constraints. A part of the Chapter 3 is dedicated to this study.

1.2.3 Fiber Structure

Another way to distinguish between the temperature and strain effects consists in using exotic specialty fibers. These optical fibers have original refractive index profiles, compositions or different characteristics such as the polarization control. In this last part we propose to discuss how the proposed fiber-based solutions target to achieve this discrimination.

1.2.3.1 Polarization maintaining optical fiber

Different studies have been focused on the potential of Polarization Maintaining Fibers (PMF) to solve this limitation. Indeed, the researchers exploit the idea that, by maintaining the polarization, the Brillouin gain and then the SNR will increase. Then by using the variations of the Brillouin power, its bandwidth, and its frequency peak in function of the strain or the temperature changes a system of equation is obtained that can be used to solve the discrimination problem. This study has been performed with three PMF structures: Panda fiber, Tiger fiber, and Bow Tie fiber [71], [72]. Unfortunately, these techniques only allow to badly discriminate the two parameters with large accuracies (82 με and 4 °C).

Another solution relying on PMF has been described in [73]. In this case, the authors used the PMF birefringence for the discrimination. Indeed, the birefringence is sensitive to both the temperature and the strain. They defined the quantity BireFS which is proportional to the birefringence Δn. Contrary to the Brillouin frequency peak, this quantity has a negative temperature coefficient. As a result, this solution provides a good discrimination with a temperature and strain accuracies of 0.4 °C and 9 με respectively.

The limitations of these PMF-based sensors remain the discrimination level in the first case and the relatively high birefringence PMF fiber and implementation prices in the second case.

1.2.3.2 Multi-peaks

Another solution is based on the characterization of an optical fiber with an optimized Brillouin response. This means that the fiber Brillouin spectrum presents at least two Brillouin frequency peaks. Indeed, if the Brillouin signature consists of two or three Brillouin frequency peaks, we then obtain two or three temperature and strain coefficients. The following equation describes the case of two peaks:

$$\begin{bmatrix} \nu_1 \\ \nu_2 \end{bmatrix} = \begin{bmatrix} C_{T1} & C_{\epsilon 1} \\ C_{T2} & C_{\epsilon 2} \end{bmatrix} \begin{bmatrix} T \\ \epsilon \end{bmatrix} \quad (1.62)$$

where ν_1 and ν_2 are the frequencies of Brillouin peaks 1 and 2 respectively, C_{T1} and C_{T2} are the temperature coefficients of the Brillouin peaks 1 and 2 respectively, and $C_{\epsilon 1}$ and $C_{\epsilon 2}$ are the strain coefficients of the Brillouin peaks 1 and 2 respectively.

1.2.3.2.1 LEAF fiber

The first identified fiber with several Brillouin frequency peaks was the LEAF fiber from Corning [74]. This fiber was designed to compensate the dispersion of the SMF28 fiber for long-distance communications. In terms of Brillouin response, the LEAF fiber presents two Brillouin frequency peaks having temperature coefficients of $C_{T1} = 1.0\, MHz/°C$ and $C_{T2} = 1.19\, MHz/°C$ and strain coefficients of $C_{\epsilon 1} = 0.051\, MHz/\mu\epsilon$ and $C_{\epsilon 2} = 0.051\, MHz/\mu\epsilon$. Then, by applying the equation (1.62), we obtain a discrimination with the following performances: temperature accuracy of 27 °C and 570 με for the strain by considering an error of 2.09 MHz and 3.1 MHz for the first and second peak measurements respectively [75]. Actually this error can be reduced thanks to the improved performances of interrogators (see chapter 3). The LEAF fiber has been studied in another work [76], where the authors studied its discrimination capacity by using both Brillouin peaks as well as the linewidth and the power of each peak. The best solution obtained by selecting the Brillouin frequency peaks and the linewidth of each one discriminates the strain and temperature with an accuracy of 37 με and 1.8°C, respectively.

1.2.3.2.2 Photonic crystal fiber

PCF presents an interest for the simultaneous measurements of strain and temperature. Indeed, it has been demonstrated in [77] that PCF fibers could present several Brillouin frequency peaks. Then by using the equation (1.62) is it possible to discriminate between the strain and temperature. These tests have been performed at 1.32 µm and seems to present a good capacity of discrimination with a remarkable spatial resolution of 15 cm, but the fiber length remains limited to 2 m for these tests. Furthermore, the PCF technology remains very expensive due to the cost of the microstructured optical fiber and limited to short distances.

1.2.3.2.3 Low loss fiber (Telecom grade)

TABLE 1.2 details the main advantages and limitations of the different discrimination technologies. Actually, the different techniques working at the interrogator level have a good capacity of discrimination, but this solution remains expensive due the complexity of interrogation scheme. Concerning the exotic fibers the inconvenients are the same. To solve the discrimination problem with a lower cost solution, I decided to focus the PhD research on the design of a fiber with multiple Brillouin frequency peaks. Indeed, by working at the fiber level it could be possible to produce a solution that is adaptable on every class of interrogator if this last has an operation frequency range that includes all Brillouin frequency peaks. Second the objective is to perform the discrimination along a long distance as those encountered by iXblue in the off-shore domain. It appears then necessary to have a sensor with a fiber exhibiting low optical losses at the operating wavelength of the interrogator (usually 1550 nm).

The main objective of this PhD work is to propose a solution of discrimination by using a multi-peak Brillouin single mode fiber with low attenuation at the telecom wavelengths. Finally, the fiber should ideally be easy to manufacture. To achieve this task, it was chosen to follow an approach coupling simulations of the fiber Brillouin response and experimental characterization of homemade fiber samples. This approach is detailed in Chapters 2 and 3.

TABLE 1.2: MAINS ADVANTAGES AND LIMITATIONS OF THE DISCRIMINATION TECHNOLOGIES OF DOFSS

		Advantages	Limitations
Two fibers	Mechanically isolated	-Good capacity of discrimination -Low losses (high sensing length)	-Number of fiber -Installation in the infrastructure due to the mechanical isolation
Interrogator	-Brillouin + - Raman -Brillouin+ Rayleigh	-Good capacities of discrimination -Low losses (high sensing length)	-Time of acquisition due to the interrogation scheme -Interrogator proprietary -Price of the interrogator
Exotic fiber	PMF	-Low losses (high sensing length) -One fiber	-Limited capacity of discrimination
	PCF PM	-One fiber -Good capacity of discrimination	-Price of the fiber due to the complexity of fabrication (150 €/m *[78]*) -Sensing range for the same reason
Multipeak	PCF		
	LEAF	-One fiber -Adaptable to a large number of commercial interrogators -Low linear losses (high sensing length)	-Capacity of discrimination -Harder to install compared to add a new interrogator
	Fiber of this PhD thesis	-One fiber -Adaptable to a large number of commercial interrogators -Low losses (high sensing length) -Capacity of discrimination -Price of production	-Harder to install compared to add a new interrogator

1.3 Conclusion

In this chapter, the operating principles of the main classes of distributed sensors (DOFSs) exploiting the different light scatterings in the silica-based optical fiber are described. The DOFSs present a high interest in several domains such as the offshore domain, the structural health monitoring, the transport etc. Each of the numerous investigated sensing architecture possesses different advantages and limitations in terms of spatial resolution, time analysis, sensing length, cost and the sensitivity. The objective here, is to propose a solution to discriminate between the temperature and the strain by optimizing only the sensitive optical fiber. Then, choosing the Brillouin-based DOFSs naturally appeared as the logical solution. Indeed, such sensors could have a sensing length of 100 km with a spatial resolution of one meter, and are sensitive to both the strain and temperature. Moreover, previous works showed that the discrimination sounds feasible by using an optical fiber having several Brillouin peaks in its signature. Actually the reported multi-peaks optical fibers do not fulfill the targeted performances in terms of discrimination.

In this PhD thesis, a model of simulation of the Brillouin response of silica-based optical fiber will be developed. After validation of this model, it will be exploited to build an optical fiber structure with two or three Brillouin peaks. Our goal is to achieve good discrimination capacities of temperature and strain while keeping low attenuation at the operating wavelength. Finally two of the modeled fibers will be manufactured by iXblue and tested to confirm our simulation tools and assess the sensor performances.

Summary (EN)

In this first chapter, a state-of-the-art on distributed fiber optic sensors is presented. A market study has demonstrated the importance of developing a new generation of sensors. The objective is to develop a sensor capable of discriminating between temperature and strain relying on a single fiber over long distances. This will be done by using a coupled simulation / experiment approach. In a second part, the Brillouin scattering is presented as well as the various sensor architectures exploiting this phenomenon. Finally, various temperature and strain discrimination techniques are detailed, giving the context around our choice to develop a multi-peak Brillouin fiber

Résumé (FR)

Dans ce premier chapitre, un état de l'art sur les capteurs distribués à fibres optiques est présenté. Une étude de marché a démontré l'importance de développer une nouvelle génération de capteurs. L'objectif est de développer un capteur capable de discriminer à la fois la température et la déformation sur de longues distances, s'appuyant sur une fibre unique. Ceci sera réalisé via une approche couplée simulation/expérience. Dans une deuxième partie, la diffusion Brillouin est introduite ainsi que les différentes architectures de capteurs exploitant ce phénomène. Enfin, différentes techniques de discrimination température/contrainte sont détaillées, donnant le contexte autour de notre choix de développer une fibre présentant plusieurs pics Brillouin.

Riassunto (IT)

In questo primo capitolo, è illustrato lo stato dell'arte dei sensori distribuiti in fibra ottica. Da un'analisi di mercato, è stato dimostrato che l'approccio alla progettazione basato sulla combinazione delle simulazioni con i dati sperimentali può fornire un aiuto significativo allo sviluppo in un'unica fibra di un sensore capace di discriminare contemporaneamente la temperatura e deformazione su lunghe distanze. Nella seconda parte del capitolo, è presentato il fenomeno dello scattering di Brillouin, così come le diverse tecnologie di sensori basate su questo fenomeno. Infine, sono argomentate le diverse tecniche per la discriminazione di temperatura/deformazione evidenziando i vantaggi e gli svantaggi di ognuna di esse, e giustificando la possibilità di sviluppare una fibra ottica caratterizzata da più di un picco Brillouin.

Chapter II: Modeling of the Brillouin signature of optical fibers: validation of the simulation procedure

2.1 Introduction to the selected simulation approach

To discriminate between the spatial and time evolutions of the temperature and the strain using a unique optical fiber, we choose an original approach based on the design of a new architecture of low-loss single-mode optical fibers (SMFs). We start our research on the development of such a low loss (typically less than 1 dB/km) optical fiber by understanding how changes in the fiber compositions and refractive-index profiles can lead to Brillouin signatures exhibiting multiple peaks. Indeed, increasing the number of Brillouin peaks allows obtaining a system of two or more equations rendering possible the discrimination if those Brillouin peaks are associated to different temperature and strain sensitivities[79]. To design this optical fiber, we combine simulations and experiments as recently done by our research group to model the temperature and radiation effects on optical amplifiers [80]. Indeed, qualified simulation tools allow testing the potential of a lot of fiber architectures at a reduced cost compared to an iterative approach based only on successive experiments. As the output of such simulations, the most promising and robust architectures can be identified and can then be manufactured for qualification through experiments.

As explained in Chapter 1, Brillouin light scattering results from the interaction between the incident optical wave and the acoustic wave(s) related to the thermal activity in spontaneous regime [48]. So, to observe this scattering phenomena a phase matching must be satisfied between those different waves. In the single-mode regime, the light propagation follows the LP01 fundamental optical mode whereas several acoustic modes are usually propagating along the fiber. Modeling the Brillouin spectrum implies, first, to calculate the LP01 mode properties at the operating wavelength, second to calculate the properties of the acoustics modes. Such calculations are achieved by solving the optical propagation and mechanical equations in the scalar approximation [81], [82]:

$$\Delta^2 E(x,y) + \left(\frac{2\pi}{\lambda}\right)^2 \left(n(x,y)^2 - n_{eff}^2\right) E(x,y) = 0 \qquad (2.1)$$

$$\Delta^2 U_m(x,y) + \left(\frac{\Omega_m^2}{V_l(x,y)^2} - \beta_{\text{acoustic}}^2\right) U_m(x,y) = 0 \qquad (2.2)$$

where Δ is the transverse Laplacian operator, λ is the wavelength of the incident light, $n(x,y)$ is the 2D Refractive Index Profile (RIP), n_{eff} is the effective index of the optical mode, $E(x,y)$ is the transversal distribution of the electric field, $U_m(x,y)$ is the longitudinal displacement field of the acoustic mode of *m* order, Ω_m is the pulsation of this acoustic mode, V_l is the longitudinal Acoustic Velocity Profile (AVP) in the fiber, and $\beta_{acoustic}$ is the acoustic propagation constant defined by equation (2.3) to respect the phase matching:

$$\beta_{acoustic} = 2\beta_{optic} = \frac{4\pi}{\lambda} n_{eff} \qquad (2.3)$$

To solve these equations we have used a Finite Element Method -2D (FEM-2D) method with COMSOL-Multiphysics™. The main advantages of this software are its ability to deal with Multiphysics systems and the accuracies of the calculations. The related drawback is that this accuracy depends on the fine mesh of the fiber, imposing long simulation runs.

Figure 2.1 reports each step of the modeling of the fiber Brillouin signature with COMSOL™. In 1) the mandatory inputs for the simulation which correspond to the measured fiber RIP, the measured (or deduced from RIP) radial distributions of the dopants (expressed in weight percent, ωt%) and the AVP deduced from the fiber composition, in 2) the COMSOL™ simulation of the optical and acoustic modes considering the fiber geometry and its meshing. In 3) with MATLAB, the calculation of the fiber Brillouin signature by considering the overlapping between the optical mode and the acoustic mode(s) at the wavelength of the interrogator. Each simulation step of this procedure will be further detailed in sections 2.2.1, 2.2.2, and 2.2.3, respectively.

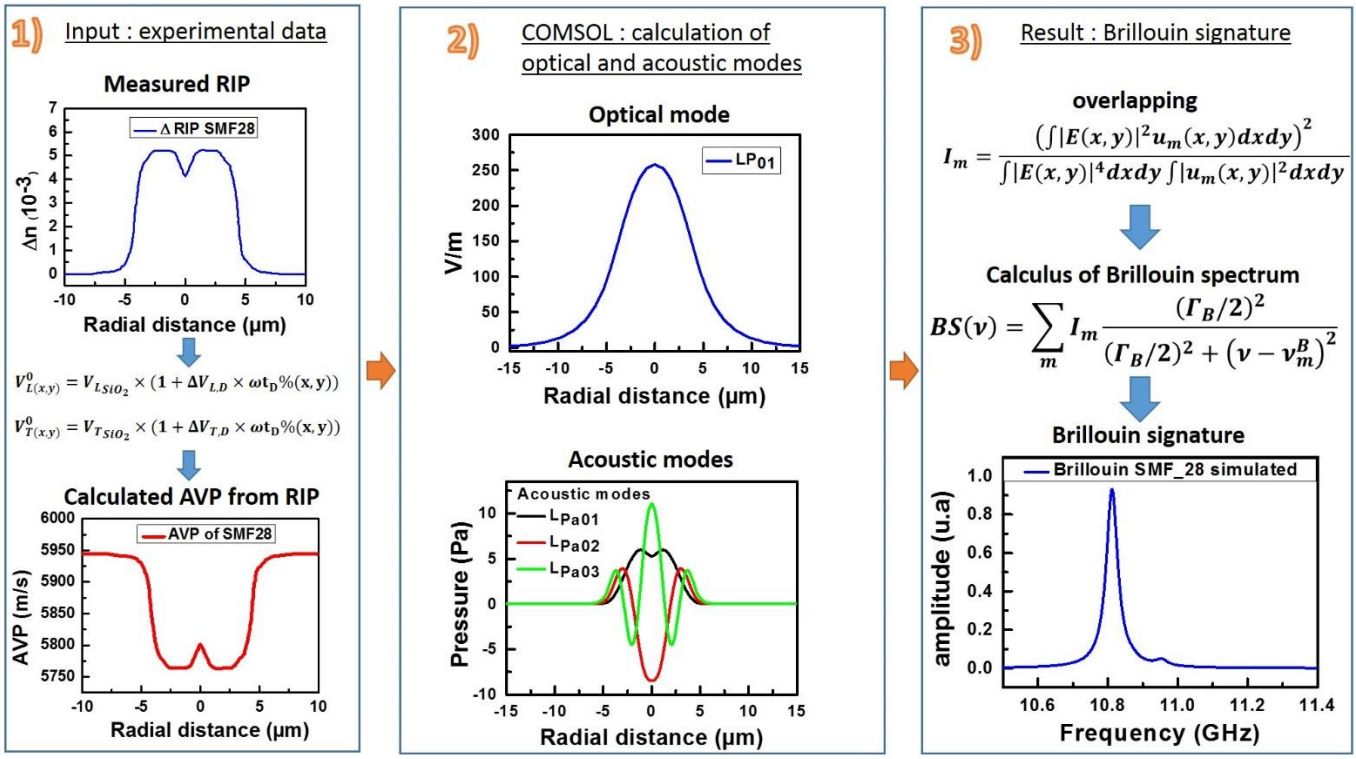

Figure 2.1: Successive simulation steps of the Brillouin signature of the single-mode optical fiber SMF28 from Corning with COMSOL™

2.2 Simulation procedure step-by-step

2.2.1 Calculation of the fundamental mode LP01

2.2.1.1 Calculation of the dopant concentrations

To model the Brillouin signature of optical fibers, it is mandatory to perform some preliminary measurements such as their core and cladding compositions, or more easily their Refractive-Index Profile (RIP). For the first step, we focus on the calculation of the guided mode(s). Most of the Telecom-grade SMFs have Ge-doped silica core and pure-silica cladding. This is the case, for example, of the SMF28 fiber from CORNING that is widely used for telecommunications as it presents low attenuation levels at 1550 nm: ~0.2 dB/km [83]. Knowing or measuring its RIP, it is possible thanks to the literature data reviewed in TABLE 2.1 to deduce the GeO_2 radial distribution (ωt%) along its diameter. If needed, chemical analysis can be performed on an unknown fiber providing the data to calcul its RIP.

TABLE 2.1: INFLUENCE OF THE CONCENTRATION OF DIFFERENT DOPANTS ON THE REFRACTIVE INDEX OF SILICA, DATA EXTRACTED FROM *[84]*

Dopant	**Δn%*/ωt%**
GeO_2	+0.056
F	-0.310
P_2O_5	+0.020
TiO_2	+0.230
Al_2O_3	+0.063
B_2O_3	-0.033

*Δn% is the variation of refractive index in percent

Figure 2.2: Conversion of the refractive index profile (RIP) of the SMF28 fiber from Corning into its radial profile of GeO_2 concentration expressed in weight percent. illustrates the conversion of the SMF28 fiber RIP into its radial distribution of GeO_2. Through this procedure, a concentration level of 5.8 ωt% GeO_2 is found, comparable to the values of 6 ωt% given by other researchers [85]. To convert the concentration from ωt% in to mol% the equation (2.4) is used giving a concentration of 3.4 mol% of GeO_2.

$$\omega t\% = \frac{\text{mol\%} \times \mathrm{M_D}}{\text{mol\%} \times \mathrm{M_D} + (1 - mol\%) M_{SiO2}} \qquad (2.4)$$

where $\mathrm{M_D}$ and M_{SiO2} are the molar masses of the dopant and the silica, respectively.

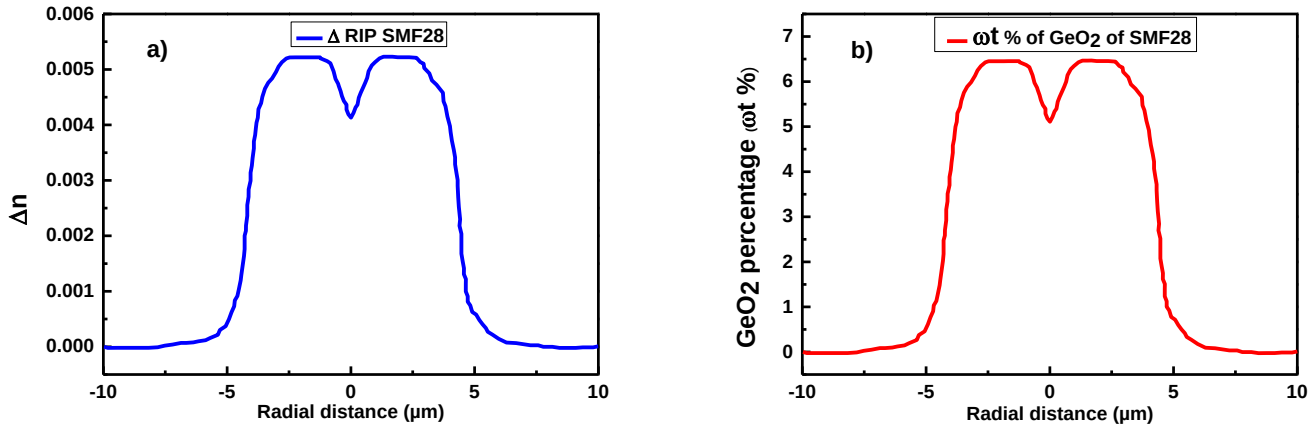

Figure 2.2: Conversion of the refractive index profile (RIP) of the SMF28 fiber from Corning into its radial profile of GeO_2 concentration expressed in weight percent.

2.2.1.2 Calculation of the optical mode

Knowing the SMF28 fiber RIP, we simulate the properties (effective index, radial distribution) of the guided modes at any wavelength. For this we consider some additional fiber characteristics in COMSOL™ such as:

- The core and cladding radius. For SMF28, they are extracted from
- Figure 2.2: Conversion of the refractive index profile (RIP) of the SMF28 fiber from Corning into its radial profile of GeO_2 concentration expressed in weight percent.~5 μm and 62.5 μm, respectively
- Type of material : silica glass
- The mesh details
- The operating wavelength (1550 nm in this example)
- The number of targeted modes, 6 were chosen for this example.

By considering all these parameters, COMSOL-Multiphysics™ calculates the radial or 2D distributions of the electric field of each optical mode.

Figure 2.3: Distribution of the calculated electric field for the LP01 optical mode at 1550 nm in the SMF28 fiber: a) 1D representation, in b) 2D representation in the transverse cross-section of the considered fiber. illustrates the obtained result at 1550 nm for the LP01 optical mode in the SMF28 fiber. As expected, the optical mode is not totally confined in the core

and a non-negligible evanescent part of the light is guided in the cladding. Finally, the calculated effective index for the LP01 mode is of 1.4463 at 1550 nm.

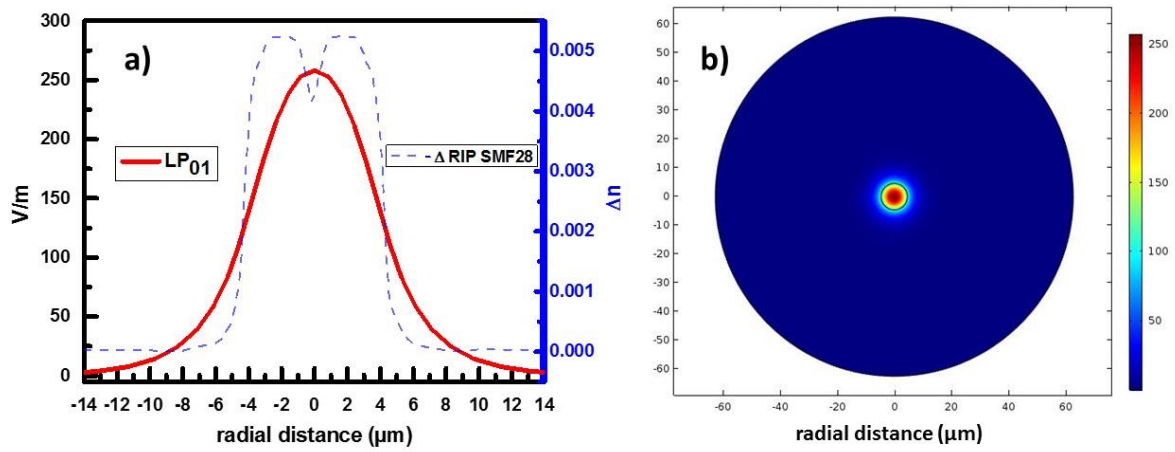

Figure 2.3: Distribution of the calculated electric field for the LP01 optical mode at 1550 nm in the SMF28 fiber: a) 1D representation, in b) 2D representation in the transverse cross-section of the considered fiber.

2.2.2 Calculation of acoustic modes

2.2.2.1 Calculation of the acoustic velocity profile (AVP)

Measuring the fiber composition or its deduction from the RIP (see Section 2.2.1.1) allows determining the AVP. Indeed, the knowledge of the coefficients listed in TABLE 2.2 allows through equations (2.5) and (2.6) to calculate the acoustic velocity for a given glass composition [86]:

$$V^0_{L\,L,SiO_2/D}(x,y) = V^0_{L\,L,SiO_2} \times \left(1 + \Delta V_{L,D} \times \omega t_D\%(x,y)\right) \quad (2.5)$$

$$V^0_{T\,T,SiO_2/D}(x,y) = V^0_{T\,T,SiO_2} \times \left(1 + \Delta V_{T,D} \times \omega t_D\%(x,y)\right) \quad (2.6)$$

where D is the dopant, $V_L{}^0{}_{L,SiO2/D}(x,y)$ is the longitudinal acoustic velocity in the silica-based fiber doped with D, $V_L{}^0{}_{L,SiO2}$ is the one of pure silica. $\Delta V_{L,D}$ is the dependence of longitudinal acoustic velocity on the D dopant concentration $\omega t_D\%(x,y)$ expressed in $\omega t_D\%$. $V^0_{T\,T,SiO_2/D}(x,y)$ is the transversal acoustic velocity of the doped glass while $V^0_{T\,T,SiO_2}$ is the one of undoped silica. Figure 2.4 represents the longitudinal AVP of the SMF28 fiber calculated from its GeO_2 radial profile. Finally, we obtain through equation (2.3) the propagation constant $\beta_{acoustic}$ of the acoustic wave. For the SMF28 fiber, $\beta_{acoustic} = 11.725 \cdot 10^7\ m^{-1}$. Equation (2.2) then gives the acoustic modes.

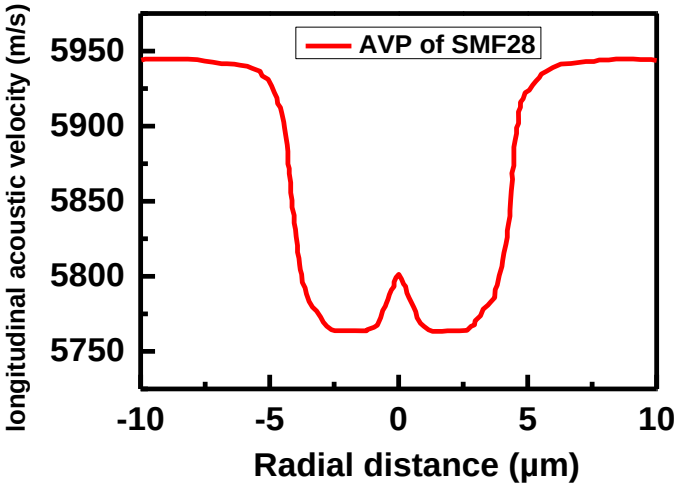

Figure 2.4: Radial acoustic velocity profile (AVP) calculated for the SMF28 fiber basing on its GeO_2-doping radial profile.

TABLE 2.2: INFLUENCE OF THE CONCENTRATIONS OF VARIOUS DOPANTS ON THE ACOUSTIC VELOCITY OF SILICA *[85], [87]–[90]*

Dopants	**V_L^0(m/s)**	**V_T^0(m/s)**	**ΔV_L (m/s) ωt%**	**ΔV_T (m/s) ωt%**
SiO_2	5944	3767	-	-
GeO_2	3310	2233	-0.47	-0.49
F	-	-	-3.60	-3.10
P_2O_5	3936	2471	-0.31	-0.41
Al_2O_3	11000	6250	+0.42	+0.21
B_2O_3	-	-	-1.23	-1.18

2.2.2.2 Calculation of the acoustic modes

Following a procedure similar to the one presented for optical modes, COMSOL was used to calculate the different acoustic modes related to the SMF28 fiber after acquiring the following input parameters:

- The radius of its core and cladding: ~5µm and 62.5µm, respectively
- Type of the material : Silica glass
- The longitudinal AVP
- The mesh
- The propagation constant of the acoustic wave (determined with equation (2.3))
- The number of desired modes, in our case 200

COMSOL^{TM} allows determining either the distribution of the acoustic pressure in the fiber cross section or the longitudinal displacement field of the pressure. Figure 2.5 shows the different acoustic modes obtained by FEM-2D, in a), b), and c) the pressure distributions in the fiber cross section for the LPa01, LPa02, and LPa03 acoustic modes, respectively. In d) the radial distributions of these three acoustic modes are illustrated. The LPa01, LPa02 and LPa03 acoustic modes have frequencies at 10.812 GHz, 10.871 GHz, and 10.954 GHz, respectively. Additional acoustic modes were calculated but they don't contribute to the fiber Brillouin signature as they present a negligible overlap with the LP01 optical mode. As it can be seen in Figure 2.5 d) the three acoustic modes of interest are mostly confined between -6µm and + 6µm. Then, these modes will be at the origin of the Brillouin spectrum as they notably overlap with the fundamental mode.

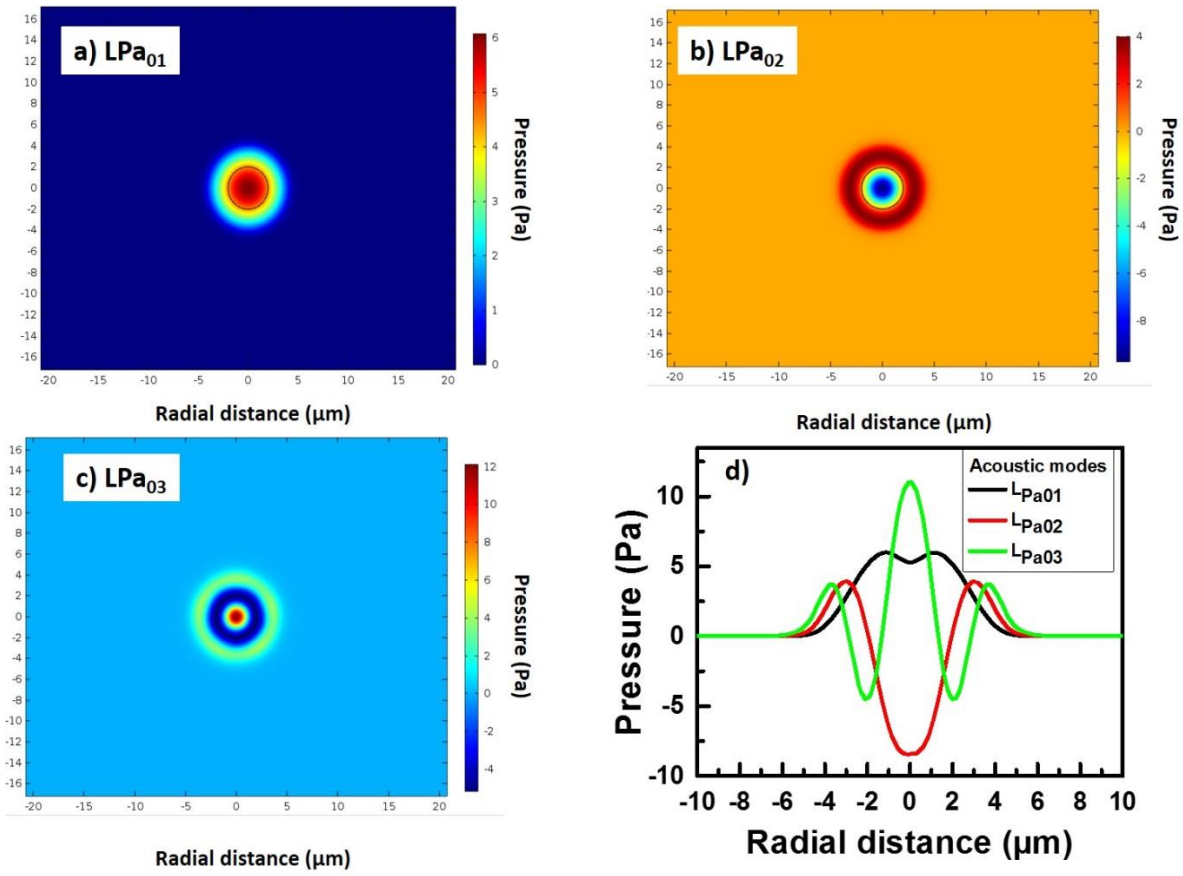

Figure 2.5: Representation of the pressure distribution in the SMF28 fiber cross-section. In a) the LPa01 mode, in b) the LPa02, in c) the LPa03 modes and in d) the radial distributions of these three acoustic modes[91].

2.2.3 Determination of the Brillouin spectrum

The next step consists in calculating the overlap between the optical mode and each of the acoustic modes. The acoustic wave is mitigated by the viscosity of the material expressed by a constant Γ_B which is equal to the inverse of the acoustic phonon lifetime. Such phenomenon can be taken into account by modelling the Brillouin spectrum *BS(ν)* using the Lorentzian function [85], [86] :

$$BS(\nu) = \sum_m I_m \frac{(\Gamma_B/2)^2}{(\Gamma_B/2)^2 + (\nu - \nu_m^B)^2} \qquad (2.7)$$

with:

$$I_m = \frac{(\int |E(x,y)|^2 u_m(x,y) dxdy)^2}{\int |E(x,y)|^4 dxdy \int |u_m(x,y)|^2 dxdy} \qquad (2.8)$$

where I_m is the overlap between the fundamental mode and the acoustic mode of order *m*, *E(x,y)* is the transverse distribution of the electric field of the optical mode, $u_m(x,y)$ the one of the acoustic mode of order *m*, Γ_B is full width at half maximum (typically ~40 MHz). This width is the same for all modes but changes with the nature and concentration of dopants or with the fiber drawing conditions. *v* is the frequency and $\nu^B{}_m$ is the Brillouin frequency of the acoustic mode of *m-th* order. Figure 2.6 illustrates our simulation results for the SMF28 fiber. The calculated Brillouin signature exhibits one peak at 10.812 GHz, a second one at 10.871 GHz with a lower intensity superimposing to the first peak, and a third one with a lower intensity at 10.954 GHz. For comparison, the experimentally measured Brillouin spectrum of this fiber exhibits one main peak at 10.840 GHz and a smaller one at 10.988 GHz. The small differences between the experiments and simulations are explained by the uncertainties on the input parameters especially about the fiber RIP extracted from [85], and a residual strain present during measurement. Anyway, the measured and calculated Brillouin responses are very close. Indeed, the difference between the frequencies of the main Brillouin peak is of 28 MHz (less than 1%).

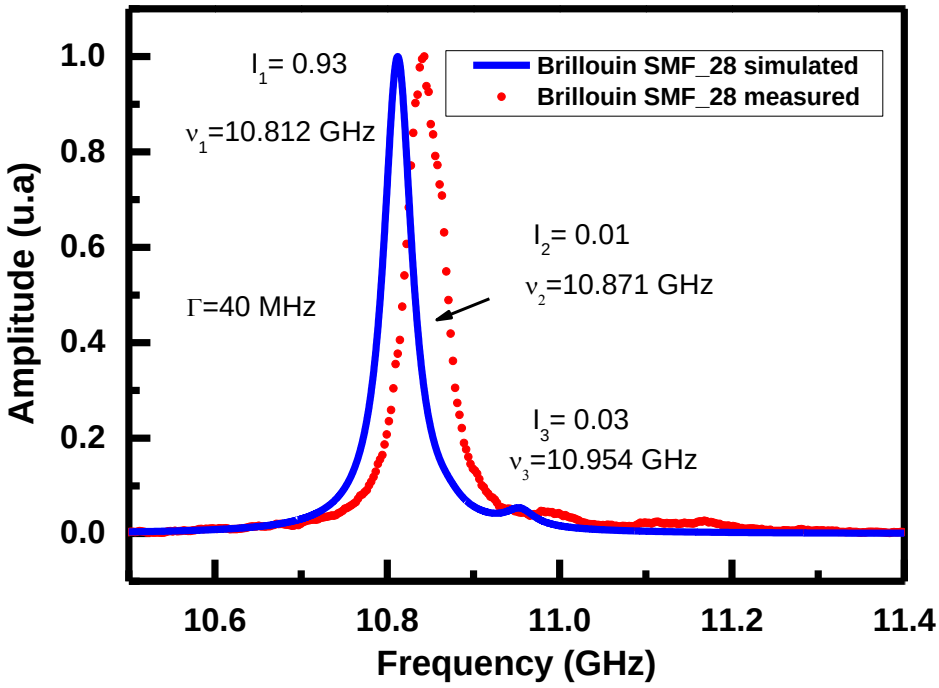

Figure 2.6: Comparison between the theoretical and experimental Brillouin spectra of the SMF28 optical fiber

2.2.4 Determination of the Brillouin temperature and strain coefficients

We defined a procedure for the calculation of the strain and temperature coefficients associated to each Brillouin frequency peak. Figure 2.7 reviews the different steps of this procedure:

- 1) Identification of the different input parameters which are needed for these simulations: examples are the dopant concentration, the glass thermo-optic coefficient, its Young modulus etc.

- 2) Modeling of the strain effect on the RIP and AVP using Comsol™.

- 3) Determination of the strain and temperature coefficients.

Each step of the simulation is further developed in this section.

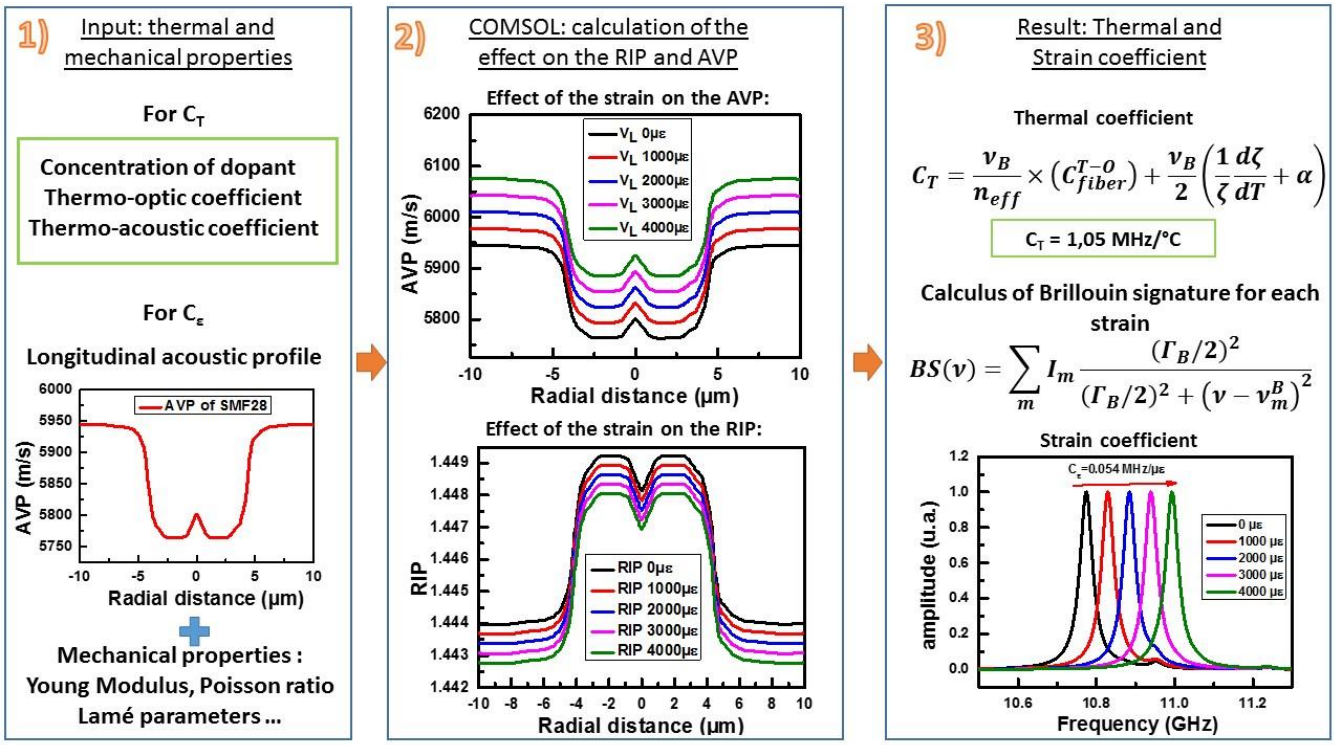

Figure 2.7: Simulation procedure used for the calculation of the temperature and strain coefficients associated to each Brillouin frequency peak.

2.2.4.1 Temperature coefficient

To determine this coefficient, the temperature effects on 1) the glass refractive index and 2) on the acoustic velocity have to be modeled. To characterize these effects an homogenous mixing model was considered [85]-[89].

Thermo-optic coefficient: C^{T-O}

The temperature effect on the refractive index has been studied in the literature, the thermo-optic coefficients for diversely doped glasses are reported in TABLE 2.3. Thanks to the homogenous model the volume percentage f_D of each dopant is given by the equation (2.9) [92]:

$$f_D = \frac{\frac{M_D}{M_{SiO_2}} \times \rho_{SiO_2} \times mol_D\%}{\rho_D + mol_D\% \times \left(\frac{M_D}{M_{SiO_2}}\rho_{SiO_2} - \rho_D\right)} \qquad (2.9)$$

where D corresponds to the dopant, M is the molar mass, $mol_D\%$ is the molar percentage in percent, and ρ the glass density.

TABLE 2.3: REPORTED VALUES OF THE THERMO-OPTIC COEFFICIENTS FOR DIFFERENT GLASSES *[93]–[98]*

Glasses	**$C_D^{T\text{-}O}$ (10^{-6}/°C)**
SiO_2	+10.4
GeO_2	+19.4
Al_2O_3	+13.1
P_2O_5	-92.2
B_2O_3	-35.0
BaO	12.7 or 18.4*
S_rO	-24.5 or -12.4*

* Different values are reported in the literature, these dopants are not investigated in this PhD thesis

In section 2.2.1 we have determined the GeO_2 level in ωt%, but in equation (2.9) we have to convert this value in molar percent (mol%) using equation (2.4). We then calculate the modified refractive index:

$$n(x,y) = f_D(x,y) \times n_D + (1 - f_D(x,y)) \times n_{SiO_2} \qquad (2.10)$$

where n_D is the refractive index of the considered doped glass, typically n_{GeO2}= 1.5871 at 1.55 µm [99], and n_{SiO2} (=1.444 at 1.55 µm) is the silica refractive index. Finally the thermo-optic coefficient is defined as the derivative of the refractive index with respect to the temperature:

$$\frac{dn}{dT} = f_D \frac{dn_D}{dT} + (1 - f_D) \frac{dn_{SiO_2}}{dT} \qquad (2.11)$$

so

$$C_{fiber}^{T-O} = f_D \times C_D^{T-O} + (1 - f_D) \times C_{SiO_2}^{T-O} \qquad (2.12)$$

where C_{fiber}^{T-O} corresponds to the thermo-optic coefficient, C_D^{T-O} is the thermo-optic coefficient of the oxide, and C_{SiO2}^{T-O} the silica thermo-optic coefficient. As an example, in the case of the SMF28 fiber, we considered a GeO_2 concentration of 5.8 ωt% (3.4 mol%), so a volume percentage of 0.0358. These input parameters lead to a calculated thermo-optic coefficient $C_{SMF28}^{T-O}=10.72\times10^{-6}$ /°C for this fiber.

Thermo-acoustic coefficient: C^{T-A}

In the case of fiber sensing, we are interested only by the longitudinal acoustic velocity. So we focused our investigation on the thermo-acoustic coefficient C^{T-A} of this velocity that depends on the Young modulus and on the material density [84], [92]:

$$V_L = \sqrt{\frac{\lambda + 2\mu}{\rho}} = \sqrt{\frac{\zeta}{\rho}} \qquad (2.13)$$

where λ and μ correspond to the Lamé parameters with $\lambda=1.6\times10^{10}$ Pa and $\mu=3.1\times10^{10}$ Pa for the silica, ρ is the density (2200 kg/m^3 for the silica), and ζ the Young modulus (73 GPa for silica). If we derive equation (2.13) with respect to the temperature we obtain the equation (2.14) [100]:

$$\frac{1}{\zeta}\frac{d\zeta}{dT} = \frac{1}{\rho}\frac{d\rho}{dT} + \frac{2}{V_L}\frac{dV_L}{dT} \qquad (2.14)$$

and

$$\frac{1}{\rho}\frac{d\rho}{dT} = -\frac{1}{v_{ol}}\frac{dv_{ol}}{dT} = -\alpha \qquad (2.15)$$

where v_{ol} is the volume and α is the expansion coefficient of the material. So, in this case we can write:

$$C_{fiber}^{T-A} = \frac{dV_L}{dT} = \frac{V_L}{2}\left(\frac{1}{\zeta}\frac{d\zeta}{dT} + \alpha\right) \qquad (2.16)$$

with $\frac{1}{\zeta}\frac{d\zeta}{dT} = 18 \times 10^{-5}$ /°C for the silica and germanium, and α =5.6×10^{-7}/°C for the silica and α=7×10^{-6}/°C for the germanium [101]. Regarding these coefficient values we can consider that the acoustic velocity change is mainly related to the temperature dependence of the Young modulus.

Calculus of the temperature coefficient: C_T

The Brillouin frequency is defined by [102]:

$$\nu_B = \frac{2n_{eff}V_{L_{eff}}}{\lambda} \qquad (2.17)$$

where ν_B is the Brillouin frequency, λ is the wavelength of the optical signal. We have shown that both the refractive index and the acoustic velocity depend on the temperature. By considering a weakly guiding fiber we have $\frac{dn_{eff}}{dT} \approx \frac{dn}{dT}$ and $\frac{dV_{L_{eff}}}{dT} \approx \frac{dV_L}{dT}$, leading to:

$$C_T = \frac{d\nu_B}{dT} = \frac{2n_{eff}}{\lambda}\frac{dV_L}{dT} + \frac{2V_{L_{eff}}}{\lambda}\frac{dn}{dT} \qquad (2.18)$$

so

$$C_T = \nu_B\left(\frac{1}{n_{eff}}\frac{dn}{dT} + \frac{1}{V_{L_{eff}}}\frac{dV_L}{dT}\right) \qquad (2.19)$$

And finally:

$$C_T = \frac{\nu_B}{n_{eff}}C_{fiber}^{T-O} + \frac{\nu_B}{2}\left(\frac{1}{\zeta}\frac{d\zeta}{dT} + \alpha\right) \qquad (2.20)$$

Concerning the SMF28 fiber, its experimentally-measured temperature coefficient is 1.05 MHz/°C. Using our simulation we found a temperature coefficient value of 1.0551 MHz/°C, very close to the experimental value.

2.2.4.2 Strain Coefficient

To calculate the strain coefficient associated to the Brillouin frequency peak, the effects of the strain on the fiber RIP and on the AVP have to be considered. By knowing how the RIP and AVP change when an external strain is applied to the fiber we can calculate the shifts of the Brillouin frequency for different strain levels. Then, the strain coefficient is calculated by performing a linear regression on all the acquired Brillouin frequencies.

The generalized Hooke's law gives a lot of information in the mechanical domain as the existence of a linear relationship between the strain and the stress in the linear elastic domain. Strain and the stress are connected by a tensor which depends on the material elastic modulus [103], [104]:

$$[\sigma] = C[\epsilon] \qquad (2.21)$$

where [σ] is the stress second-order tensor, ε is the strain second order tensor, and *C is a fourth-order tensor* called elastic tensor. In isotropic linear elastic materials the elastic tensor can be written as:

$$C_{i,j,k,l} = \left[\lambda_L \delta_{ij}\delta_{kl} + \mu_L\left(\delta_{ik}\delta_{jl} + \delta_{il}\delta_{jk}\right)\right] \qquad (2.22)$$

where λ_L and μ_L are the Lamé parameters, $\delta_{i,j}$ is the Kronecker delta function, and i,j,k,l correspond to the 3 directions x,y and z. So by combining equations (2.22) and (2.21) the following equation can be inferred [105]:

$$\begin{bmatrix}\sigma_{xx}\\ \sigma_{yy}\\ \sigma_{zz}\\ \sigma_{xy}\\ \sigma_{yz}\\ \sigma_{xz}\end{bmatrix} = \begin{bmatrix}\lambda_L + 2\mu_L & \lambda_L & \lambda_L & 0 & 0 & 0\\ \lambda_L & \lambda_L + 2\mu_L & \lambda_L & 0 & 0 & 0\\ \lambda_L & \lambda_L & \lambda_L + 2\mu_L & 0 & 0 & 0\\ 0 & 0 & 0 & \mu_L & 0 & 0\\ 0 & 0 & 0 & 0 & \mu_L & 0\\ 0 & 0 & 0 & 0 & 0 & \mu_L\end{bmatrix} \times \begin{bmatrix}\epsilon_{xx}\\ \epsilon_{yy}\\ \epsilon_{zz}\\ 2\epsilon_{xy}\\ 2\epsilon_{yz}\\ 2\epsilon_{xz}\end{bmatrix} \qquad (2.23)$$

The Young modulus ζ and the Poisson ratio ν can be defined by the Lamé parameters:

$$\zeta = \mu_L \frac{3\lambda_L + 2\mu_L}{\lambda_L + \mu_L} \quad (2.24)$$

$$\nu = \frac{\lambda_L}{2(\lambda_L + \mu_L)} \quad (2.25)$$

As a result, equation (2.23) can be rearranged and the following equations can be obtained:

$$\begin{bmatrix} \epsilon_{xx} = \frac{1}{\zeta} \times [\sigma_{xx} - \nu(\sigma_{yy} + \sigma_{zz})] \\ \epsilon_{yy} = \frac{1}{\zeta} \times [\sigma_{yy} - \nu(\sigma_{xx} + \sigma_{zz})] \\ \epsilon_{zz} = \frac{1}{\zeta} \times [\sigma_{zz} - \nu(\sigma_{xx} + \sigma_{yy})] \\ \epsilon_{xy} = \frac{1+\nu}{\zeta}\sigma_{xy} \\ \epsilon_{yz} = \frac{1+\nu}{\zeta}\sigma_{yz} \\ \epsilon_{xz} = \frac{1+\nu}{\zeta}\sigma_{xz} \end{bmatrix} \quad (2.26)$$

In the case of optical fiber, we consider that the stress is uniformly applied along the longitudinal axis (x). Finally we obtain:

$$\begin{bmatrix} \epsilon_{xx} = \frac{1}{\zeta}\sigma_{xx} \\ \epsilon_{yy} = \epsilon_{zz} = -\nu\frac{\sigma_{xx}}{\zeta} \\ \epsilon_{xy} = \epsilon_{yz} = \epsilon_{xz} = 0 \end{bmatrix} \quad (2.27)$$

As a result, when a stress is applied along one direction the equation (2.21) can be simplified by:

$$\sigma = \zeta\epsilon \quad (2.28)$$

Following this calculation procedure we can model the effects of an external stress on the fiber AVP and RIP.

2.2.4.2.1 Acousto-elastic effect: effect of the strain on the AVP

By stressing the fiber both density and the elasticity of the silica material change and then modify the AVP. Taking into account the Hook's law, the following equation can be obtained:

$$\sigma(\epsilon) - \sigma^0 = C^0(\epsilon - \epsilon^0) + C'(\epsilon - \epsilon^0)^2 + C''(\epsilon - \epsilon^0)^3 + \cdots \quad (2.29)$$

The constants C^0, C' and C'' are defined at the state 0 (without stress and at room temperature) and depend only on this state. The first coefficient C^0 corresponds to the linear approximation (near of the state 0). The constants C' and C'' correspond to the higher orders: quadratic and cubic or orders 3 and 4. In the case of the developed sensor the first-order approximation was considered:

$$\sigma(\epsilon) - \sigma^0 = C^0(\epsilon - \epsilon^0) \quad (2.30)$$

To calculate the acousto-elastic coefficient, we use the studies of Murnaghan [106], [107] concerning the nonlinear elasticity in isotropic material. For an isotropic solid subjected to a uniaxial stress, the longitudinal and transverse acoustic velocities propagating in the same direction than the applied stress can be described in function of this stress [108]:

$$V_L^\sigma = \sqrt{\frac{\lambda_L + 2\mu_L}{\rho}\left[1 + \frac{\sigma}{(\lambda_L + 2\mu_L)(3\lambda_L + 2\mu_L)}\left(\frac{\lambda_L + \mu_L}{\mu_L}(4\lambda_L + 10\mu_L + 4m) + \lambda_L + 2l\right)\right]} \quad (2.31)$$

$$V_T^\sigma = \sqrt{\frac{\mu_L}{\rho}\left[1 + \frac{\sigma}{\mu_L(3\lambda_L + 2\mu_L)}\left(4\lambda_L + 4\mu_L + m + \frac{\lambda_L p}{4\mu_L}\right)\right]} \quad (2.32)$$

where V_L^σ, V_T^σ are the longitudinal and transverse acoustic velocities after applying a stress, l,m,p are the Murnaghan coefficients (elastic coefficients of the material of the third order) with l=11.95×10^{10} Pa, m=7.47×10^{10} Pa, and p=-4.15×10^{10} Pa for silica [85]. The residual internal stress of the fiber changes the acoustic velocity. By considering the Taylor series representation of the equations (2.31) and (2.32) and taking into account the linear term the following equations can be derived:

$$V_L^\sigma = V_L^0\,(1 + K_L\sigma) \tag{2.33}$$

$$V_T^\sigma = V_T^0\,(1 + K_T\sigma) \tag{2.34}$$

where V_L^0, V_T^0 are the longitudinal and transverse acoustic velocities for the unstressed fiber. K_L and K_T are the longitudinal and transverse acousto-elastic coefficients defined by :

$$K_L = \frac{1}{2(\lambda_L + 2\mu_L)(3\lambda_L + 2\mu)}\left(\frac{\lambda_L + \mu_L}{\mu_L}(4\lambda_L + 10\mu_L + 4m) + \lambda_L + 2l\right) \tag{2.35}$$

$$K_T = \frac{1}{2\mu_L(3\lambda_L + 2\mu_L)}\left(4\lambda_L + 4\mu_L + m + \frac{\lambda_L p}{4\mu_L}\right) \tag{2.36}$$

For a stress applied along the longitudinal axis we can calculate the new AVP:

$$V_L^\sigma = V_L^0\,(1 + K_L\zeta\epsilon) \tag{2.37}$$

$$V_T^\sigma = V_T^0\,(1 + K_T\zeta\epsilon) \tag{2.38}$$

Concerning the SMF28 fiber example, Figure 2.8 illustrates the evolution of its AVP for five different applied strains: 0, 1000, 2000, 3000, and 4000 με. The Young modulus used for the calculation of the new AVP is the one of the fiber and not the one of silica. To calculate this Young modulus value, we have used the equation (2.39). The same calculations are done for the Poisson ratio, the density, and the Lamé parameters:

$$\zeta_{fiber}(x,y) = \rho_{fiber}(V_T^0(x,y))^2\,\frac{3(V_L^0(x,y))^2 - 4(V_T^0(x,y))^2}{\left[\left(V_L^0(x,y)\right)^2 - \left(V_T^0(x,y)\right)^2\right]^2} \tag{2.39}$$

$$\nu_{fiber}(x,y) = \frac{(V_L^0(x,y))^2 - 2(V_T^0(x,y))^2}{2[(V_L^0(x,y))^2 - (V_T^0(x,y))^2]} \tag{2.40}$$

$$\rho_{fiber}(x,y) = f_D(x,y)\,\rho_D + [1 - f_D(x,y)]\rho_{SiO_2} \tag{2.41}$$

$$\lambda_{L\,fiber}(x,y) = \frac{\zeta_{fiber}(x,y)\,\nu_{fiber}(x,y)}{\left(1 + \nu_{fiber}(x,y)\right)\left(1 - 2\nu_{fiber}(x,y)\right)} \tag{2.42}$$

$$n_{L_{fiber}}(x,y) = \frac{\zeta_{fiber}(x,y)}{2\left(1 + \nu_{fiber}(x,y)\right)} \tag{2.43}$$

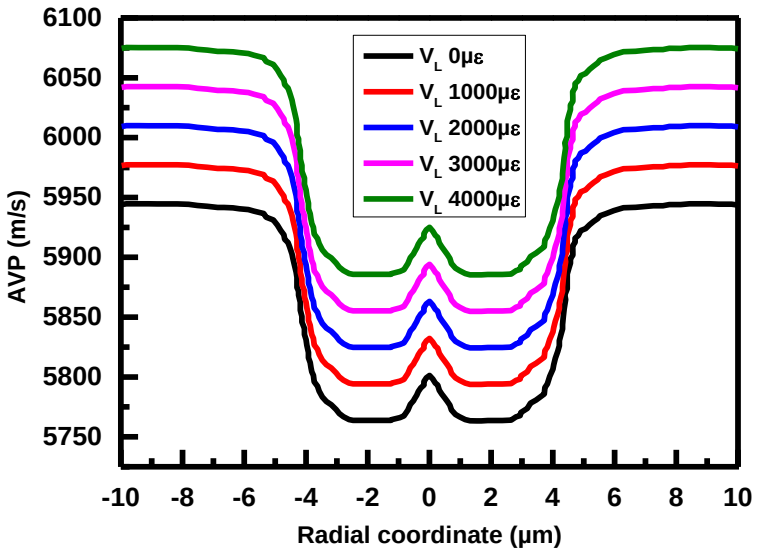

Figure 2.8: evolution of the Acoustic Velocity Profile (AVP) of the SMF28 fiber for different strains applied along its longitudinal axis

2.2.4.2.2 Photo-elastic effect: effect of the strain on the RIP

Concerning the effect of the stress on the refractive index we have used the equation (2.44) [109], [110] to model it:

$$n^{\sigma} = n^{0} - C \times \sigma \qquad (2.44)$$

where n^{σ} is the new refractive index after applying the stress, n^{0} is the RIP at the state 0. C is the photo-elastic coefficient and its value is equal to 4.2×10^{-12} Pa for silica. By injecting equation (2.28) in the equation (2.44) we can calculate the RIP for each strain. Figure 2.9 shows the RIP for each of the strains applied to the SMF28 fiber. In this figure, a silica refractive index equal to 1.444 at 1.55 µm has been used [111]. Contrary to the AVP, the RI value decreases with the strain.

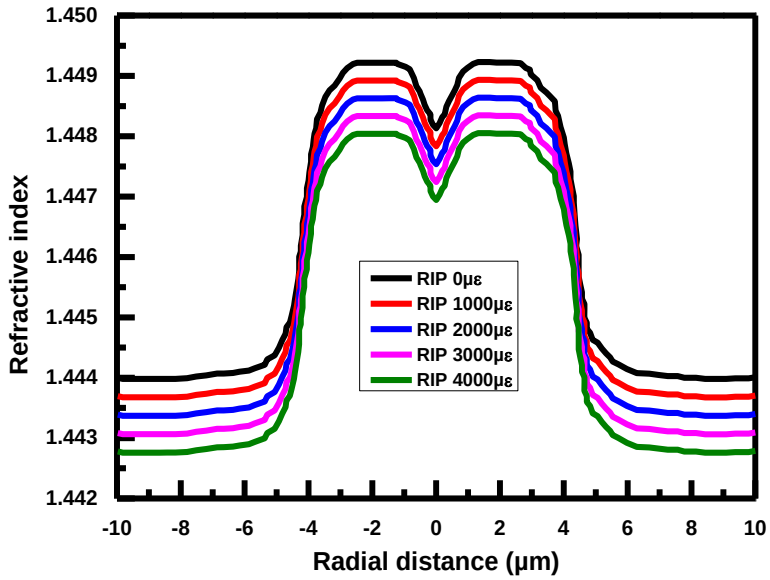

Figure 2.9: Evolution of the RIP of the SMF28 fiber when different strains are applied along the longitudinal axis

Having the new RIP and AVP for each strain, we can calculate the Brillouin spectra for the different applied strains. Figure 2.10 illustrates such simulations for the SMF28 fiber. Its calculated strain sensitivity coefficient C_ε is 0.054 MHz/µε close to the experimental value measured as 0.05MHz/µε. Simulation only exceeds by 8% the experimental data. Such difference is considered as acceptable especially as the measurement errors related to the ± 0.64 MHz precision of the used BOTDA are here not considered.

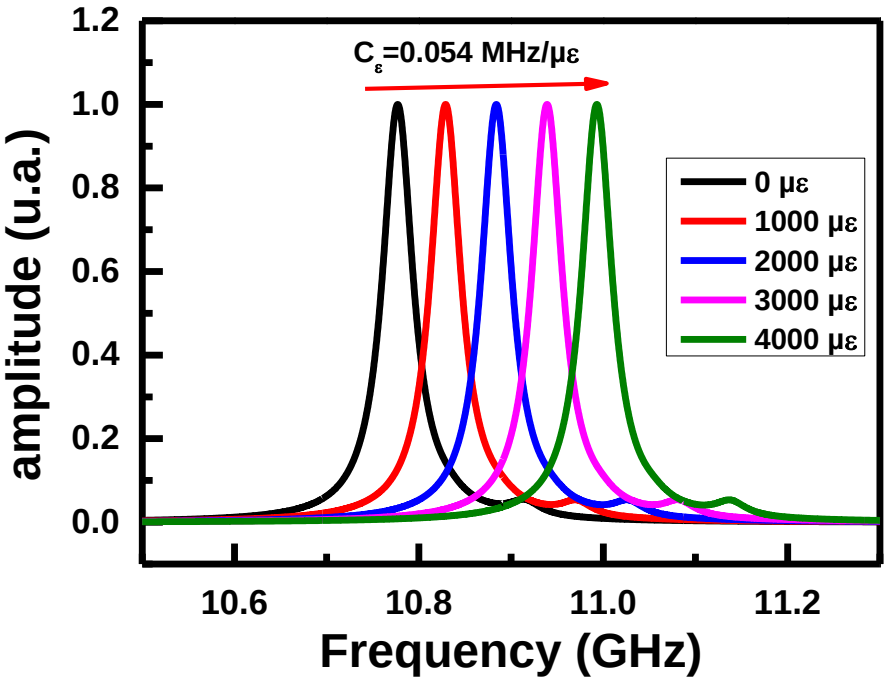

Figure 2.10: Calculated evolution of the SMF28 fiber Brillouin spectrum versus the external strain.

2.2.5 Validation of the simulation: Impact of the core dopants

We have demonstrated that our simulation procedure allows calculating the Brillouin frequency, strain and temperature sensitivity coefficients in a way representative of the experiments for the Telecom-grade SMF28 germanosilicate fiber. In order to fully characterize the robustness of our codes, the Brillouin signatures of several SMFs diversely doped in their cores have been calculated. The different core dopants were the phosphorus pentoxide (P_2O_5), Germanium dioxide (GeO_2), and fluorine (F). TABLE 2.4 describes those different samples[1]. Their RIPs have been measured by the Inter Fiber Analysis (IFA from Interfiber Analysis) at iXblue Photonics. This commercial setup is based on a Michelson interferometer so that by measuring the phase of the light it is possible to determine the RIP of the fiber at 963 nm with a spatial resolution of 0.164 µm and an error of about 10^{-4} for the refractive index [113]. It is important to notice that the RIP is measured on uncoated fiber samples.

[1] This work has been presented during the Workshop on Specialty Optical Fiber (WSOF 2017) in Cyprus, 2017 [112].

TABLE 2.4: SET OF OPTICAL FIBERS WITH DIFFERENT CORE DOPING SELECTED TO EVALUATE THE ROBUSTNESS OF THE SIMULATION TOOLS.

Name of Sample	Dopant in core	Dopant in cladding	Type of coating	Manufacturer
SMF_P1	P_2O_5 (≈ 30ωt%)	Silica	Acrylate	iXblue
SMF_P2	P_2O_5 (≈ 50ωt%)	Silica	Acrylate	iXblue
SMF28	GeO_2 (≈ 6ωt%)	Silica	Acrylate	Corning
SMF_GeH	GeO_2 (≈ 20ωt%)	Silica	Acrylate	iXblue
SMF_F1	F (≈ 0.2ωt%)	F (≈ 3ωt%)	Acrylate	iXblue
SMF_F2	F (≈ 0.2ωt%)	F (≈ 3ωt%)	Polyimide	iXblue

2.2.5.1 Phosphorus doped fiber

To validate our model on P_2O_5-doped fibers, two fibers have been selected. SMF_P1 is doped at 30 ωt% (P_2O_5) and SMF_P2 is doped at 50 ωt%. By following the previously described model, the Brillouin spectra as well as the temperature and strain sensitivity coefficients have been calculated. All results concerning these two fibers are given in TABLE 2.5 and TABLE 2.6. Simulated Brillouin frequencies and strain coefficients well agree with experimental results: differences of less than 1% for the Brillouin frequency and 2.3% for the strain coefficient are obtained. Concerning the temperature coefficient, the difference is larger, around 10%. As a conclusion, the simulation still provide results representative to experiments.

TABLE 2.5: COMPARISON BETWEEN THE CALCULATED AND MEASURED BRILLOUIN FREQUENCIES FOR THE TESTED PHOSPHORUS-DOPED FIBERS

Sample name	Brillouin frequency (measured; GHz)	Brillouin frequency (simulated; GHz)	Difference (%)
SMF_P1	10.140	10.059	0.8
SMF_P2	10.142	10.114	0.3

TABLE 2.6 : COMPARISON BETWEEN THE CALCULATED AND MEASURED STRAIN AND TEMPERATURE SENSITIVITY COEFFICIENTS FOR THE TWO TESTED PHOSPHORUS-DOPED FIBERS

Sample name	Strain coefficient measured (MHz/με)	Strain coefficient simulated (MHz/με)	Difference (%)	Temperature coefficient measured (MHz/°C)	Temperature coefficient simulated (MHz/°C)	Difference (%)
SMF_P1	0.043	0.042	2.3	0.71	0.80	11.3
SMF_P2	0.044	0.043	2.3	0.69	0.78	11.5

2.2.5.2 Germanium doped fiber

Two different GeO_2-doped fibers have been considered. The first one is the SMF28 detailed in parts 2.3 and 2.4. The second one (SMF_GeH) has a higher GeO_2 concentration into its core. TABLE 2.7 and TABLE 2.8 compare the obtained simulation results with the experimental ones. As for the P_2O_5-doped fibers, the calculated Brillouin frequencies are really close to the measured ones. Concerning the strain sensitivity coefficient, the difference between modeling and experiments is around 8.0% for both fibers. For the temperature sensitivity coefficient, the difference appears slightly larger for the SMF_GeH (10.0%) than the SMF28 (1.0%). For this type of fibers, the simulations provide valuable results too.

TABLE 2.7: COMPARISON BETWEEN THE CALCULATED AND MEASURED BRILLOUIN FREQUENCIES FOR THE TWO TESTED GE-DOPED FIBERS

Sample name	Brillouin frequency (measured ; GHz)	Brillouin frequency (simulated; GHz)	Difference between experiment and simulation (%)
SMF28	10.840	10.812	0.3
SMF_GeH	10.205	10.204	0.01

TABLE 2.8: COMPARISON BETWEEN THE CALCULATED AND MEASURED STRAIN AND TEMPERATURE SENSITIVITY COEFFICIENTS FOR THE TESTED GE-DOPED FIBERS

Sample name	Strain coefficient measured (MHz/με)	Strain coefficient simulated (MHz/με)	Difference (%)	Temperature coefficient measured (MHz/°C)	Temperature coefficient simulated (MHz/°C)	Difference (%)
SMF28	0.050	0.054	7.4	1.05	1.055	0.5
SMF_GeH	0.044	0.048	8.3	1.10	0.99	10.0

2.2.5.3 Fluorine-doped fiber

Finally, the last investigated dopant is the Fluorine. Once again two samples have been tested: SMF_F1 and SMF_F2. These fibers have the same RIP (they are from the same preform) but different coatings: acrylate coating for SMF_F1 and polyimide coating for SMF_F2. The difference between the calculated and measured Brillouin frequencies is below 1.3% for both fibers as reported in TABLE 2.9. Concerning the strain and temperature sensitivity coefficients the larger error is observed for the SMF_F2: 9.0% for both the strain and temperature sensitivity coefficients (TABLE 2.10). In both cases the simulation still valuable predictions. Moreover this confirms that the coating nature seems able to influence the fiber strain and temperature coefficients, or at least it affects the quality of the strain transfer in our experimental setup. This observation may be explained by the difference between the Young modulus of the acrylate and polyimide, or by different internal stress distributions for the two fibers [114]–[116].

TABLE 2.9: COMPARISON BETWEEN THE CALCULATED AND MEASURED BRILLOUIN FREQUENCIES FOR THE TWO TESTED FLUORINE-DOPED FIBERS

Sample name	Brillouin frequency (measured ; GHz)	Brillouin frequency (simulated; GHz)	Difference (%)
SMF_F1	11.063	10.923	1.3
SMF_F2	11.069	10.923	1.3

TABLE 2.10: COMPARISON BETWEEN THE CALCULATED AND MEASURED STRAIN AND TEMPERATURE SENSITIVITY COEFFICIENTS FOR THE TWO TESTED F-DOPED FIBERS

Sample name	Strain coefficient measured (MHz/με)	Strain coefficient simulated (MHz/με)	Difference (%)	Temperature coefficient measured (MHz/°C)	Temperature coefficient simulated (MHz/°C)	Difference (%)
SMF_F1	0.053	0.054	1.9	1.27	1.2	5.5
SMF_F2	0.049	0.054	9.3	1.32	1.2	9.1

2.2.5.4 Effect of the dopant on the sensing performances

In order to optimize the Brillouin-based sensor performance, different core dopants have been investigated. Figure 2.11 shows for each sample a) the Brillouin frequency, b) the strain sensitivity coefficients, and c) the temperature sensitivity coefficients. For each case, red dots concern the calculated results and black squares the experimental ones. It is worth to notice that the fluorine doped fiber SMF_F1 exhibits the best sensing potential due to its larger strain and temperature sensitivity coefficients compared to other samples. Indeed, a large value for the coefficients means that the sensor will be more sensitive for the temperature and strain measurements.

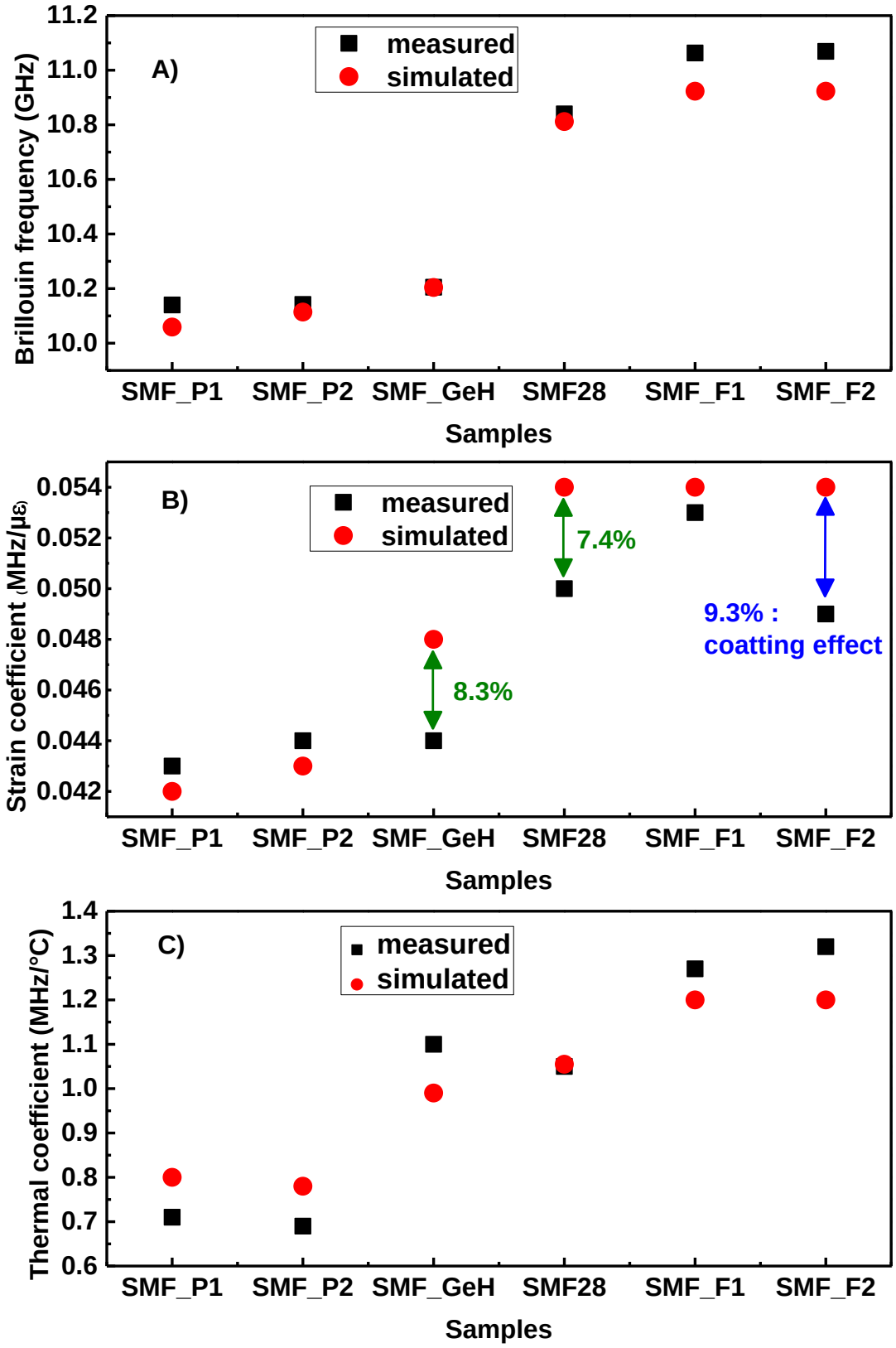

Figure 2.11: Comparison between the Brillouin characteristics of the diversely doped optical fibers. a) Brillouin frequency, b) strain sensitivity coefficient, c) temperature sensitivity coefficient. Simulation results (red dots) and measurements (black squares)

2.2.6 Partial conclusion

A methodology has been selected to model the Brillouin signature of an optical fiber. The correctness of this approach has been evaluated by benchmarking the simulation results to their experimental counterparts. The first step consists in predicting the fiber Brillouin spectrum knowing its refractive index profile (RIP) and its composition. From these data, the optical and the acoustic modes can be calculated and then the Brillouin signature is determined. Finally, by using the Hooke's equation and a homogenous model, the strain and temperature coefficients associated to the Brillouin frequencies have been calculated. Our simulation results have been compared to the experimental data reported in the literature for the SMF28 fiber from CORNING. Simulation and experiments nicely agree. This comparison was then extended to additional optical fibers being diversely doped in their core with either GeO_2, P_2O_5, or F. Some of the considered samples have the same composition but different types of coatings, either acrylate or polyimide. For this set, the calculated and measured Brillouin spectra are again very close for all tested fibers, the largest difference being of 1.3% for one of the investigated F-doped fibers. Concerning the temperature and the strain coefficients, the difference between the experiments and simulations is slightly larger than the one reported for the Brillouin spectrum but remains clearly acceptable. The maximum difference observed for the temperature coefficients is of 11.0% for one of the tested P_2O_5-doped fibers and of 9.0% for the strain coefficient of one of our F-doped fibers. A possibility to further improve the accuracy of simulation could be to consider the temperature dependence of the fiber Young modulus. Another important result concerns the coating impact on the Brillouin signature. As highlighted by the comparison between two F-doped fibers drawn from the same preform with either an acrylate or a polyimide coating, a noticeable difference between their strain coefficients is observed. Different tests will be suggested in section 3 to better characterize the fiber coating effect on its Brillouin signature.

The impact of other parameters on the quality of the Brillouin modeling will now be studied: the effect of varying the cladding composition, the impact of the dopant concentration and the variation of the RIP. The objective of this study was to demonstrate that playing with these different parameters, it appears possible to design a low-loss optical fiber with a Brillouin spectrum having several Brillouin frequency peaks opening the way to the targeted strain and temperature discrimination.

2.2.7 Investigation of multi-peak fiber

Our objective was to develop an optical fiber with at least two Brillouin peaks, ideally three. One commercial optical fiber exhibits such characteristic: the LEAF fiber from CORNING [117]. Another solution could regard the implementation of a few mode optical fiber: in this way the high-order optical modes enable more degree of freedom due to their different overlappings with the acoustic modes. In our case, we focus the attention on a standard single mode fiber architecture. A patent [118] shows that a solution could be the implementation of one or more dopant in the fiber cladding. The idea is to better confine acoustic modes in the fiber core to increase the overlap between these acoustic mode and the optical mode.

2. 2.7.1 Different adjustable parameters

To investigate a multi-peak fiber, the impact of different fiber parameters will be tested such as the core dopant or the structure of the RIP. Indeed, for the RIP, the refractive index difference between the core and the cladding, the shape of the RIP, the size of the doped inner cladding can be adjusted within the ranges allowed by the Modified Chemical Vapor Deposition (MCVD) fabrication process. An example of the measured RIP for a germanosilicate optical fiber, fiber SMF_C2, with a F-doped cladding is illustrated in Figure 2.12. As it can be seen, the refractive index is lowered between 2.5 µm and 12.5 µm (inner cladding) compared to the rest of the cladding (outer cladding). This is achieved by doping the inner cladding with F. The core of this fiber is doped with GeO_2 and the RIP in the core follows a trapezoidal shape. A total of six single-mode germanosilicate fibers have been tested with similar RIPs but varying their cladding compositions. The characteristics of all these fibers are detailed in TABLE 2.11.

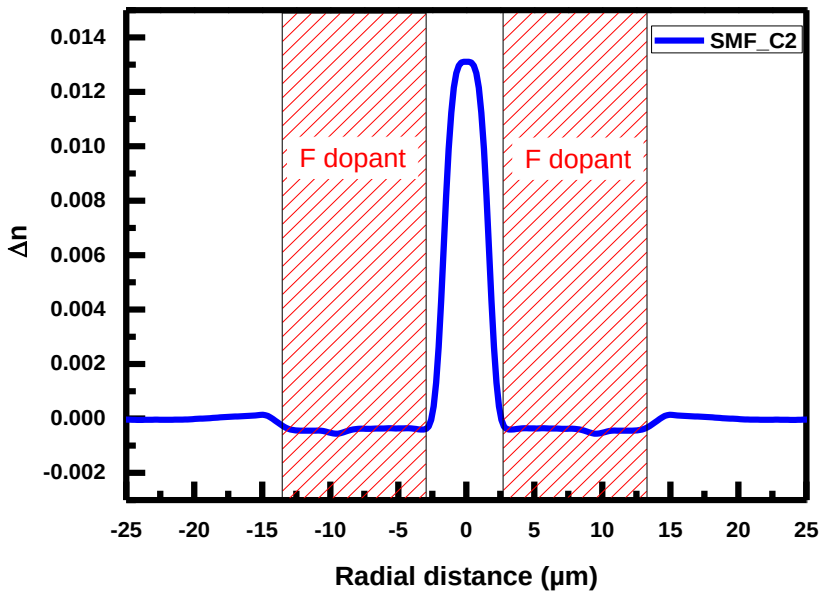

Figure 2.12: Measured refractive index profile (RIP) of GeO_2-doped SMF_C2 fiber with F-doping in its inner

TABLE 2.11: CHARACTERISTICS OF THE SEVEN TESTED SAMPLES: GERMANOSILICATE SMFS WITH VARIOUS CODOPINGS IN THEIR INNER CLADDINGS

Sample Name	SMF_C1	SMF_C2	SMF_C3A	SMF_C3B	SMF_C4	SMF_C5
Core dopant	Ge	Ge	Ge	Ge	Ge	Ge
Cladding dopant	P, F	F	Ge, P, F	Ge, P, F	Ge, F	Ge, P
Drawing tension (g)	140	140	140	20	140	140

2.2.7.2 Determination of the Brillouin frequencies

The methodology to simulate these fiber Brillouin responses remains the one described in paragraphs 2.1 to 2.4. The sole difference is that for these new fibers, different dopant combinations have been considered. The codopant concentrations in the fiber claddings have been measured by the EMPA (Electron MicroProbe Analysis) method [119].

Knowing the exact fiber composition and applying the homogenous method, the fiber RIP and AVP have been calculated.

$$n_{mix(x,y)} = f_{D1(x,y)} \times n_{D1} + f_{D2(x,y)} \times n_{D2} + \cdots + f_{Dn(x,y)} \times n_{Dn} + \left(1 - f_{D1(x,y)} - f_{D2(x,y)} - \cdots - f_{Dn(x,y)}\right) \times n_{SiO_2} \quad (2.45)$$

Where $n_{mix(x,y)}$ is the calculated RIP, D_1 D_2 and D_n correspond to dopant 1, 2 and n respectively, and f_{D1}, f_{D2} and f_{D3} are the volume percentages for each dopant.

$$V^0_{L\,L,SiO_2/D1\ldots D_n}(x,y) = V^0_{L\,L,SiO_2}(x,y) \times \left(1 + \Delta V_{L,D1} \times \%\omega t_{D1}\%_{(x,y)} + \Delta V_{L,D2} \times \%\omega t_{D2}\%_{(x,y)} + \cdots + \Delta V_{L,D_n} \times \%\omega t_{D_n}\%_{(x,y)}\right) \quad (2.46)$$

$$V^0_{T\,T,SiO_2/D1\ldots D_n}(x,y) = V^0_{T\,T,SiO_2}(x,y) \times \left(1 + \Delta V_{T,D1} \times \omega t_{D1}\%_{(x,y)} + \Delta V_{T,D2} \times \omega t_{D2}\%_{(x,y)} + \cdots + \Delta V_{T,D_n} \times \omega t_{D_n}\%_{(x,y)}\right) \quad (2.47)$$

where $\Delta V_{T,Dn}$ is the variation of the transversal acoustic velocity of the dopant D_n, and $\omega t_{D1}\%_{(x,y)}$ is the concentration in weight percent of the same dopant. To calculate the Brillouin frequency, the equation set detailed in paragraphs 2.1 and 2.2 together with the AVP determined through equations (2.46) and (2.47) have been taken into account. For the SMF_C2 RIP, the simulation reveals the presence of three discernable Brillouin peaks (see Figure 2.13) with associated Brillouin frequencies corresponding at ν_{1s}= 10.331 GHz, ν_{2s}= 10.644 GHz and ν_{3s}= 10.959 GHz (blue line). For comparison the experimental Brillouin signatures are located at ν_{1e}= 10.343 GHz, ν_{2e}= 10.650 GHz and ν_{3e}= 11.034GHz (red line). This confirms a very good agreement between simulations and experiments with differences of about 0.1%, 0.1% and 0.7% for the peaks 1, 2, and 3, respectively.

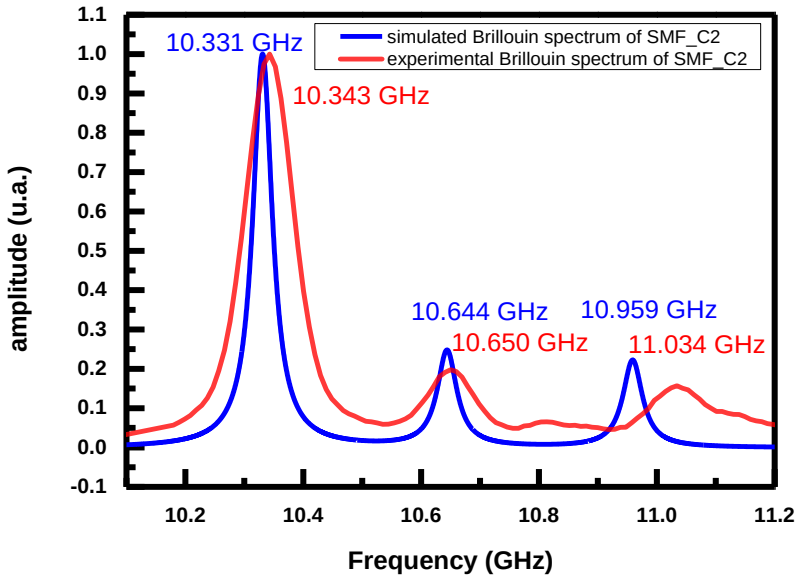

Figure 2.13: Brillouin Signature of germanium doped SMF_C2 fiber with fluorine in cladding. In blue the simulated Brillouin spectrum, and in red the measured Brillouin spectrum of SMF_C2

2.2.7.3Determination of the sensitivity coefficients

2.2.7.3.1. Temperature coefficient

Thermo-optic coefficient: $C^{T\text{-}O}$

For the general case of a fiber glass doped with more than one dopant, the effect of each doping element on the thermo-optic coefficient has to be calculated to obtain the temperature coefficient:

$$\frac{dn_{mix}}{dT} = f_{D1}\frac{dn_{D1}}{dT} + f_{D2}\frac{dn_{D2}}{dT} + \cdots + f_{Dn}\frac{dn_{Dn}}{dT} + (1 - f_{D1} - f_{D2} - \cdots - f_{Dn})\frac{dn_{SiO_2}}{dT} \quad (2.48)$$

then

$$C^{T-O}_{fiber\_mix} = f_{D1} \times C^{T-O}_{D1} + f_{D2} \times C^{T-O}_{D2} + \cdots + f_{Dn} \times C^{T-O}_{Dn} + (1 - f_{D1} - f_{D2} - \cdots - f_{Dn}) \times C^{T-O}_{SiO_2} \quad (2.49)$$

Thermo-acoustic coefficient: $C^{T\text{-}A}$

As for the thermo-optic coefficient, the thermo-acoustic coefficient changes with the fiber composition. The Young modulus is related to the silica acoustic velocity that depends on the dopant concentration. In the case of the multi-peak fibers, the effective acoustic velocity changes for each acoustic mode. It means that equation (2.20) becomes:

$$C_{T_m} = \frac{\nu_{B_m}}{n_{eff}} C_{fiber\_mix}^{T-O} + \frac{\nu_{B_m}}{2}\left(\frac{1}{\zeta}\frac{d\zeta}{dT} + \alpha\right) \qquad (2.50)$$

Where C_{T_m} is the temperature coefficient corresponding to the peak number m and ν_{B_m} is the frequency of this peak. We calculated, through equation (2.50), for the SMF_C2 fiber the three temperature coefficients: C_{T1}=1.01 MHz/°C, C_{T2}=1.04 MHz/°C, and C_{T3}=1.07 MHz/°C. Through experiments, those coefficients have been found as: C_{T1}=1.11 MHz/°C, C_{T2}=1.09 MHz/°C, and C_{T3}=1.12 MHz/°C leading to differences of 9.0%, 4.6%, and 4.5%, respectively. These differences between simulation and experiments remain acceptable for the targeted applications.

2.2.7.3.2 Strain Coefficient

For the strain coefficient, the simulation procedure is unchanged compared to the fiber doped with a unique dopant, we used Equations (2.37) and (2.38) with the acoustic velocity calculated by using Equations (2.46) and (2.47). The results are presented in part 2.8.1.2

2.2.8 Validation of the simulation: Impact of the dopant in the cladding

To validate the pertinence of our tools to conceive a fiber exhibiting several Brillouin peaks, we have then modeled the Brillouin signatures of the seven fibers and compared with our calculation results with measurements made on these fibers with a BOTDA[2].

[2] . These results were presented at the 2018 Optical Fiber Sensor (OFS) conference in Lausanne (CH) [120].

2.2.8.1. Effect of the cladding co-dopants

2.2.8.1.1 Brillouin Frequency peak

The obtained simulation results, in terms of overlap between optical and acoustic modes, are summarized in TABLE 2.12. Each of the fibers has the same GeO_2 level in its core, but these fibers differ in terms of their cladding composition. Their normalized Brillouin spectra are given in Figure 2.14. As it can be seen, all fibers exhibit three discernable Brillouin peaks at different frequency values and different amplitudes. The variation of the relative peak amplitudes is due to the different overlaps between the optical mode and the three acoustic modes (LPa01, LPa02 and LPa03).

TABLE 2.12: CALCULATED OVERLAPS BETWEEN THE OPTICAL MODE AND THE ACOUSTIC MODES FOR THE SEVEN TESTED FIBER SAMPLES

Sample name	Modal overlap between LP01 optical and LPa01 acoustic (%)	Modal overlap between LP01 optical and LPa02 acoustic (%)	Modal overlap between LP01 optical and LPa03 acoustic (%)
SMF_28	92.93	1.3	3.2
SMF_C1	61.56	16.7	11.3
SMF_C2	65.56	16.0	14.5
SMF_C3A	64.89	16.4	11.4
SMF_C4	67.60	14.1	15.2
SMF_C5	67.25	14.6	16.3

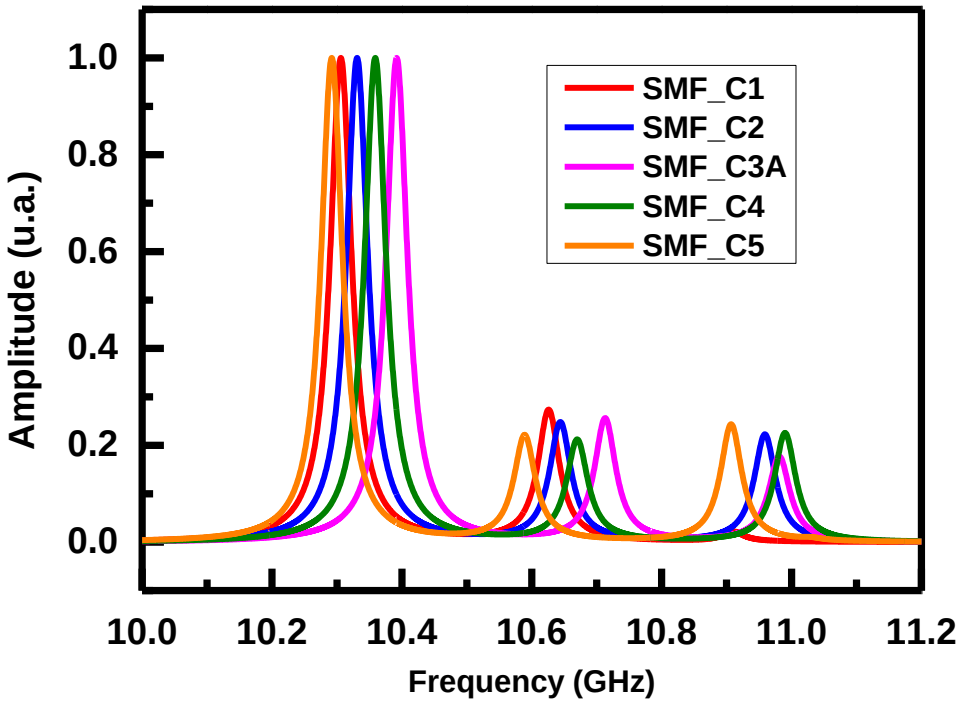

Figure 2.14: normalized calculated Brillouin spectra of the six germanosilicate optical fibers differently doped in their inner claddings

The comparison between the simulations and the experiments is reported in TABLE 2.13 and represented in Figure 2.15 showing a) the first, b) the second, and c) the third Brillouin frequencies. For all plots red and black squares correspond to the simulation outputs and experimental results, respectively. The blue squares represents ±5% error on the experimental results. The good agreement between all these data demonstrates that our prediction tools are very accurate even for complex fiber architectures.

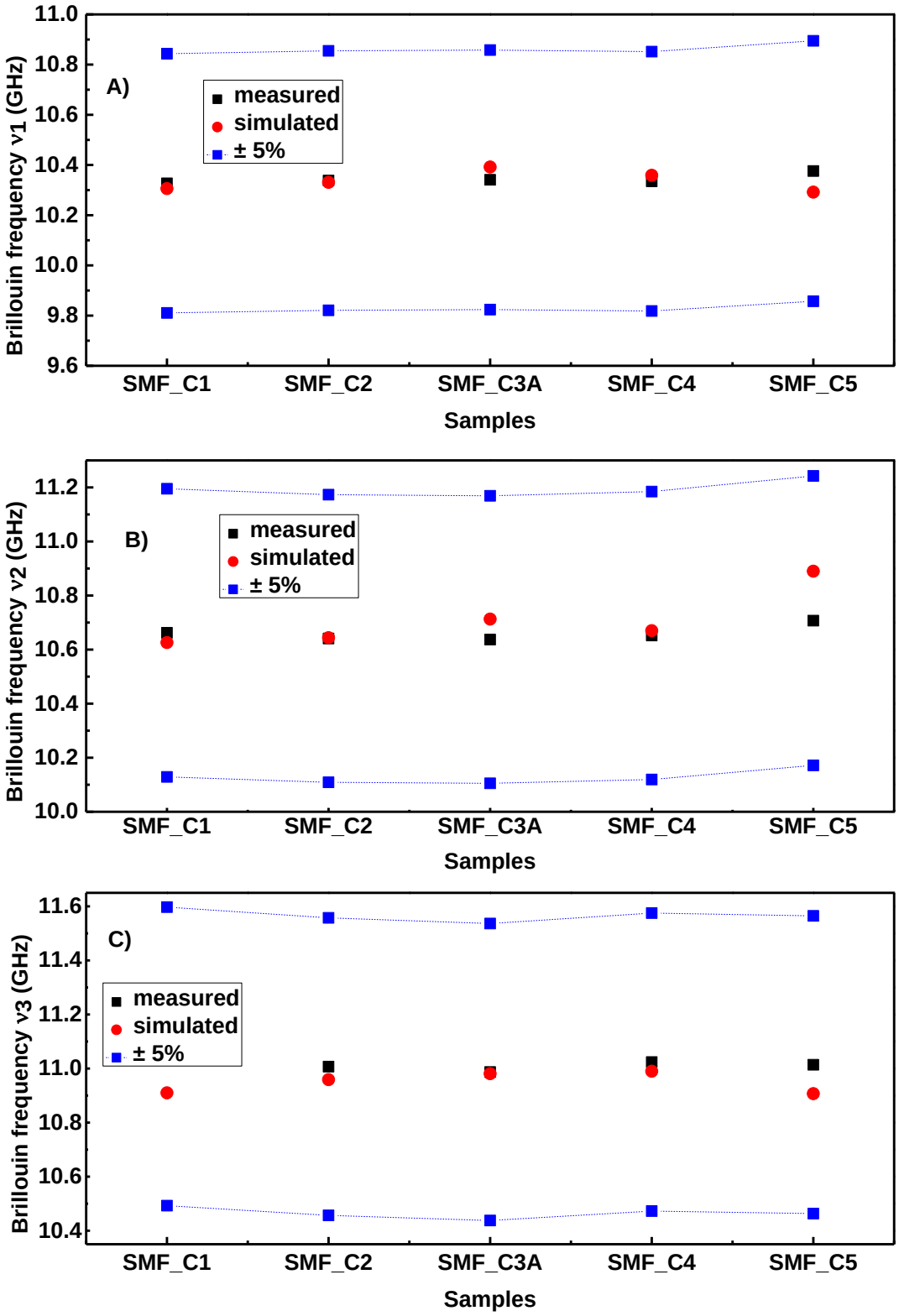

Figure 2.15: Brillouin peak frequencies measured for each sample. a) First peak, b) second peak, c) third peak frequencies. Red and black squares represent the calculated and the experimental results, respectively. The blue squares correspond to the ±5% to experimental results.

TABLE 2.13: COMPARISON BETWEEN THE MEASURED AND SIMULATED BRILLOUIN SIGNATURES OF THE FIBERS UNDER TEST.

Sample	Peak 1 exp (GHz)	Peak 1 sim (GHz)	Diff (%)	Peak 2 exp (GHz)	Peak 2 sim (GHz)	Diff (%)	Peak 3 exp (GHz)	Peak 3 sim (GHz)	Diff (%)
SMF_C1	10.327	10.306	0.2	10.662	10.626	0.3	11.045	10.910	1.2
SMF_C2	10.343	10.331	0.1	10.650	10.644	0.7	11.034	10.959	0.7
SMF_C3A	10.341	10.392	0.5	10.637	10.713	0.7	10.987	10.981	0.1
SMF_C5	10.335	10.359	0.2	10.652	10.67	0.2	11.024	10.99	0.3
SMF_C6	10.376	10.292	0.8	10.707	10.589	1.1	11.014	10.907	1.0

2.2.8.1.2 Temperature and strain coefficients

For a given fiber and for each of its three Brillouin frequency peaks, different values of the strain and temperature coefficients have been obtained. Figure 2.16 reports the acquired results. For each plot, the red dots and black squares correspond to the theoretical and the experimental results, respectively. The blue squares correspond to the ±10.0% estimated experimental, related to the interrogator frequency step. TABLE 2.14 reports all the strain coefficients, the difference between experiments and simulation remains below 9.0%. To discriminate between the temperature and strain distributions along a multi-peak optical fiber, it is mandatory that those peaks possess sufficiently different coefficients. By comparing the Ge-doped fibers with various cladding dopants, it can be observed that they present comparable strain coefficient values for the first “main” Brillouin frequency. The largest measured difference is of 5.4% while a maximum difference of 2.2% is expected from the simulations. For the second peak, a larger difference of up to 16% is experimentally obtained, larger than what could be expected (2.8%) from the simulations. Finally for the third peak, the maximal measured difference is about 11.0% to be compared to the value of 3.4% for the simulation.

TABLE 2.14: COMPARISON BETWEEN THE MEASURED AND CALCULATED STRAIN COEFFICIENTS OF THE SIX GERMANOSILICATE FIBERS DIFFERENTLY DOPED IN THEIR INNER CLADDING

Sample	$C_{\varepsilon 1}$ (MHz/με) exp	$C_{\varepsilon 1}$ (MHz/με) sim	Diff (%)	$C_{\varepsilon 2}$ (MHz/με) exp	$C_{\varepsilon 2}$ (MHz/με) sim	Diff (%)	$C_{\varepsilon 3}$ (MHz/με) exp	$C_{\varepsilon 3}$ (MHz/με) sim	Diff (%)
SMF_C1	0.0505	0.0492	2.6	0.0472	0.0518	8.9	0.0539	0.0536	0.6
SMF_C2	0.0506	0.0497	1.8	0.0515	0.052	0.9	0.0555	0.055	0.9
SMF_C3A	0.0538	0.0503	6.5	0.0561	0.0533	5	0.0606	0.0558	7.9
SMF_C4	0.0521	0.0498	4.4	0.0538	0.052	3.3	0.0561	0.0555	1.1
SMF_C5	0.0532	0.0493	7.3	0.0543	0.0518	4.6	0.0556	0.0551	0.9

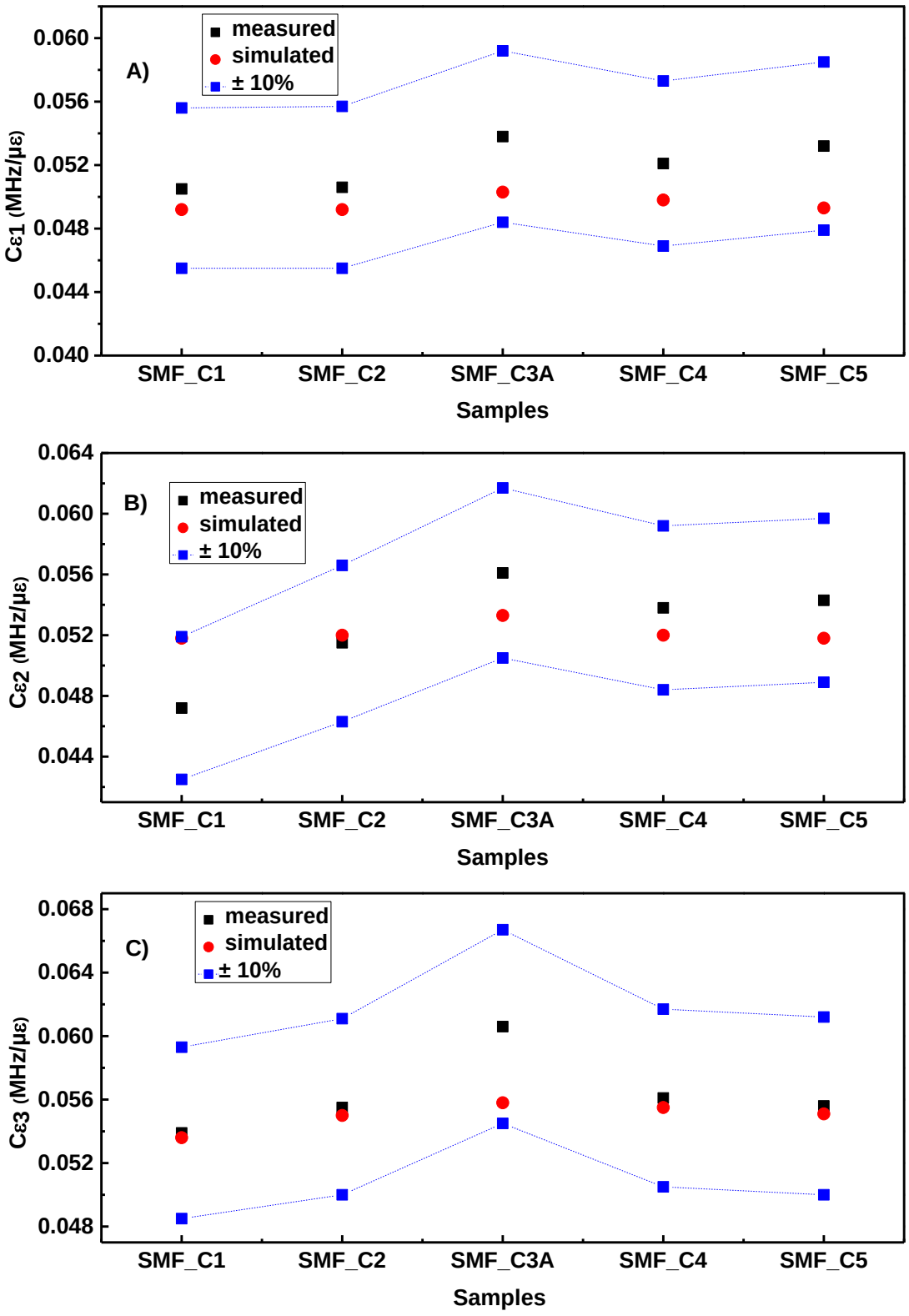

Figure 2.16 Strain sensitivity coefficient of each fiber sample. a) Strain coefficient of the first b) the second, c) the third Brillouin frequency peaks. The blue squares correspond to the ±10 % error associated to the experimental results.

Figure 2.17 shows the temperature sensitivity coefficient associated to each Brillouin frequency peak of the different fibers. As for the strain sensitivity coefficient, red dots and black squares correspond to the simulated and measured results, respectively. The blue squares correspond to the ±10% error associated with the BOTDA measurements. Results reported in TABLE 2.15 highlight a larger difference between experiments and simulations for the temperature sensitivity coefficient than for the strain one. Typically, we obtain a difference of about 10% between the simulations and the measurements, with the largest difference of ~15% for the third peak of SMF_C4 and the lowest difference of ~4.5% for the third peak of the SMF_C2. These results are consistent with those presented in section 2.5 on more simple fiber architectures. Here again, the quality of the simulation remains acceptable to evaluate the potential of a fiber structure for sensing. The comparison of the temperature coefficients of the first Brillouin peak of all samples provides a maximal difference of 6.2% for the experimental results and of only 1% for the simulation results. Concerning the second Brillouin frequency peak, the maximum difference between all samples is 20.8% for the experimental results and 1% for the simulation results. Finally, for the third temperature coefficient, the maximum difference between all samples is 10.4% for the experimental results and 1% for the simulated results. Despite this 20% difference between the experimental temperature coefficients, we cannot consider that the dopant influence this parameter notably. Indeed the measurement error of the Brillouin frequency by our BOTDA is of about 0.5 MHz while this 20% correspond to a variation of 0.2 MHz. As a summary, even if varying the doping in the inner cladding does not greatly influence the temperature and strain coefficients, these small differences can be used to optimize the discrimination efficiency between strain and temperature measurements.

TABLE 2.15: COMPARISON BETWEEN THE MEASURED AND CALCULATED TEMPERATURE COEFFICIENTS OF THE SIX GERMANOSILICATE FIBERS DIFFERENTLY DOPED IN THEIR INNER CLADDING

Sample	C_{T1} (MHz/°C) exp	C_{T1} (MHz/°C) sim	Diff (%)	C_{T2} (MHz/°C) exp	C_{T2} (MHz/°C) sim	Diff (%)	C_{T3} (MHz/°C) exp	C_{T3} (MHz/°C) sim	Diff (%)
SMF_C1	1.06	1	5.7	0.99	1.04	4.8	1.24	1.06	14.5
SMF_C2	1.11	1.01	9	1.09	1.04	4.6	1.12	1.07	4.5
SMF_C3A	1.09	1.01	7.3	1.2	1.04	13.3	1.23	1.07	13
SMF_C4	1.12	1.01	9.8	0.95	1.04	8.7	1.25	1.07	14.4
SMF_C5	1.13	1.004	11.2	1.02	1.03	4.6	1.2	1.06	11.6

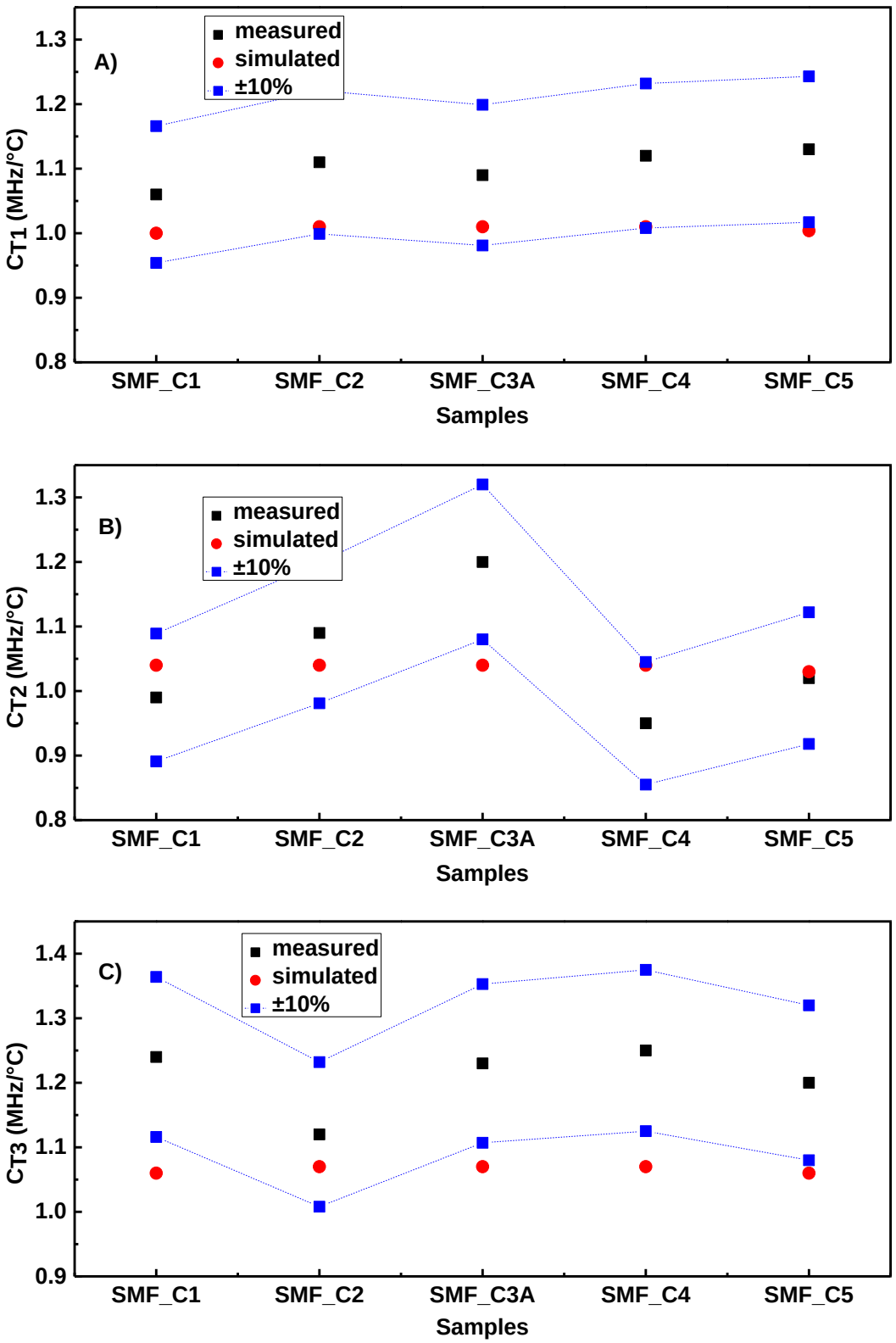

Figure 2.17: temperature sensitivity coefficient of each sample, a) First, b) second, c) third Brillouin frequency peaks. Blue dots correspond to the ±10 % error associated with the experimental results.

2.2.8.2 Effect of drawing tension

2.2.8.2.1 Brillouin frequency

By using two fibers from the same preform but differently drawn, we can study the drawing impact on the fiber Brillouin response. To this aim, we have measured the RIP of both the SMF_C3A and the SMF_C3B drawn at 140 g and 20 g, respectively. Their modeled Brillouin responses are given in Figure 2.18 and their characteristics are compared with the experimental results in TABLE 2.16. As for the previous studies, the calculated and measured Brillouin responses are in excellent agreement (difference < 1%).

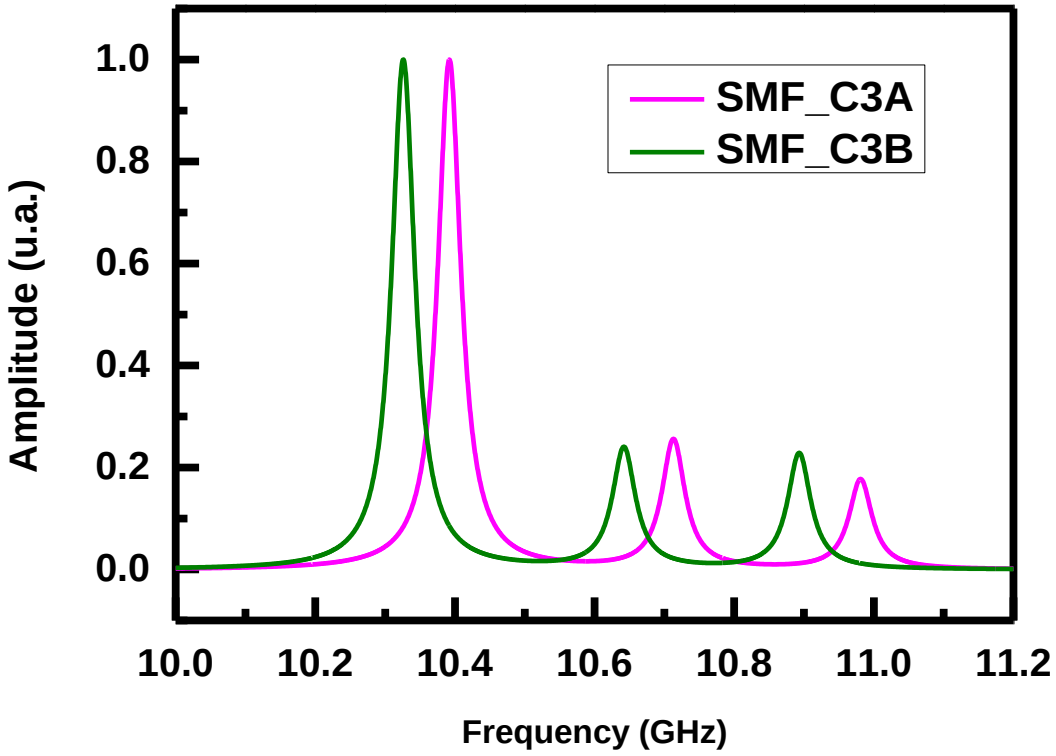

Figure 2.18: Calculated Brillouin spectra of two fibers drawn from the same preform but with differents tensions: SMF_C3A drawn at 140g and SMF_C3B drawn at 20g

TABLE 2.16: COMPARISON BETWEEN THE CALCULATED AND MEASURED FREQUENCIES FOR THE BRILLOUIN FREQUENCIES OF THE TWO FIBERS DRAWN WITH DIFFERENT TENSIONS (140G, 20G) FROM THE SAME PREFORM.

Sample	Peak 1 exp (GHz)	Peak 1 sim (GHz)	Diff (%)	Peak 2 exp (GHz)	Peak 2 sim (GHz)	Diff (%)	Peak 3 exp (GHz)	Peak 3 sim (GHz)	Diff (%)
SMF_C3A	10.341	10.392	0.5	10.637	10.713	0.7	10.987	10.981	0.1
SMF_C3B	10.39	10.326	0.6	10.688	10.642	0.4	11.042	11.03	0.1

2.2.8.2.2 Effect of drawing on temperature and strain coefficient

The influence of the drawing tension on the strain and temperature sensitivity coefficients has been investigated too. TABLE 2.17 and TABLE 2.18 compare the calculated and measured strain and temperature sensitivity coefficients. Concerning the strain coefficient, we obtain a mean difference of 7 % with a maximum of 8 % (peak n°1 SMF_C3B) and a minimum of 5% (peak n°2 SMF_C3A). For the temperature sensitivity coefficient, this difference is around 11% with a maximum of 14.4% for the SMF_C3B peak n°3 and with a minimum of 7.3% for the SMF_C3A peak n°1. Then, we can suggest that the drawing tension influence is on the order of 10.0% on the strain and temperature coefficients. This variation is low but may be used to increase the discrimination performance of the fiber. A more detailed study on this topic will be developed in section III.

TABLE 2.17: COMPARISON BETWEEN THE CALCULATED AND MEASURED STRAIN COEFFICIENTS OF THE TWO FIBERS DRAWN WITH DIFFERENT TENSIONS (140G, 20G) FROM THE SAME PREFORM.

Sample	SMF_C3A	SMF_C3B
$C_{\varepsilon 1}$ (MHz/με) experimental	0.0538	0.0543
$C_{\varepsilon 1}$ (MHz/με) simulated	0.0503	0.0497
Difference (%)	6.5	8
$C_{\varepsilon 2}$ (MHz/με) experimental	0.0561	0.0533
$C_{\varepsilon 2}$ (MHz/με) simulated	0.0566	0.0523
Difference (%)	5.0	7.6
$C_{\varepsilon 3}$ (MHz/με) experimental	0.0606	0.0598
$C_{\varepsilon 3}$ (MHz/με) simulated	0.0558	0.056
Difference (%)	7.9	6.4

TABLE 2.18: COMPARISON BETWEEN THE CALCULATED AND MEASURED TEMPERATURE COEFFICIENTS OF THE TWO FIBERS DRAWN WITH DIFFERENT TENSIONS (140G, 20G) FROM THE SAME PREFORM.

Sample	SMF_C3A	SMF_C3B
C_{T1} (MHz/°C) experimental	1.09	1.11
C_{T1} (MHz/°C) simulated	1.01	1
Difference (%)	7.3	9.8
C_{T2} (MHz/°C) experimental	1.2	1.12
C_{T2} (MHz/°C) simulated	1.04	1.04
Difference (%)	13.3	8.7
C_{T3} (MHz/°C) experimental	1.23	1.25
C_{T3} (MHz/°C) simulated	1.07	1.08
Difference (%)	13.0	14.4

2.3 Conclusion

In this chapter we succeed to simulate the Brillouin signatures of very different single-mode optical fibers. To achieve this we used the COMSOL^{TM} software based on the Finite Element Method. By knowing the composition of the fiber we have been able to calculate the refractive-index profile (RIP) and the acoustic velocity profile (AVP), and then use them as input parameters for the COMSOL simulation. We have demonstrated that our simulation of the Brillouin signature matches very well with the experiments. The difference remains below 1% for the different types of fibers. In a second time we have determined the strain and the temperature coefficients of each sample and, as for the Brillouin signature, the simulation quite well reproduces the experiment results. Moreover, this study has shown that the pure-silica-core optical fiber exhibits the highest strain or temperature sensitivities. Another important result concerns the effect of the fiber coating on its strain coefficient. The polyimide coating seems more interesting, polyimide fibers offering higher strain coefficient than acrylate one. After the validation of our simulation, we have investigated the effect of changing the cladding composition in order to conceive optical fiber with multi Brillouin peaks signature. The most important result concerns our ability to identify structures of MCVD optical fibers exhibiting several Brillouin peaks. The second result deals with the effects of the dopant and of the drawing tension on the fiber Brillouin response. Indeed, both factors seems to be of interest to tailor the value of the strain sensitivity coefficient corresponding to the Brillouin frequencies. All these parameters could be further improved to optimize the performance of our discriminating sensor.

Finally, we can consider the simulation procedure as fully validated and can now use the codes to conceive optical fibers with architectures optimized to offer Brillouin signatures with the most promising discrimination capabilities. This work will be presented in the next chapter of the PhD Thesis.

Summary (EN)

In this chapter, a simulation model of the Brillouin response in an optical fiber has been developed. The simulation model takes into account the composition of the fiber and the distribution of dopants. The results obtained with the simulation are very close to the experimental results as regards the Brillouin frequency, the temperature coefficients or the strain coefficients. A first part shows the impact of the dopants incorporated in the fiber core on the Brillouin response. The second part of the chapter focuses on the effect of dopants present into the cladding, thus opening the way to the manufacturing of optical fibers with a multi-peak Brillouin signature through MCVD process.

Résumé (FR)

Dans ce chapitre, un modèle de simulation de la réponse Brillouin dans une fibre optique a été développé. Le modèle de simulation prend en compte la composition de la fibre et la répartition des dopants. Les résultats obtenus par simulation sont très proches de ceux acquis expérimentalement aussi bien concernant la fréquence Brillouin, les coefficients de température ou encore les coefficients de déformation. Une première partie montre l'impact des dopants en cœur sur la réponse Brillouin. La deuxième partie du chapitre est focalisée sur l'effet des dopants dans la gaine, et ouvre ainsi la voie à la réalisation de fibres optiques avec une signature Brillouin multi-pics par le procédé MCVD.

Riassunto (IT)

In questo capitolo, è illustrato il modello matematico utilizzato per la simulazione della risposta Brillouin in fibra ottica. Esso considera la composizione della fibra ottica e della distribuzione dei droganti al suo interno. I risultati della simulazione hanno fornito valori della frequenza di Brillouin e dei coefficienti di temperatura e di deformazione molto prossimi a quelli ricavati sperimentalmente. Nella prima parte del capitolo è evidenziato l'impatto sulla risposta di Brillouin dei droganti presenti nel nucleo della fibra ottica. La seconda parte è invece focalizzata sullo studio dell'effetto dei droganti all'interno del materiale che costituisce il mantello della fibra ottica nonché della possibilità di sviluppare fibre ottiche caratterizzate da una risposta di Brillouin con picchi multipli.

Chapter III: Strain and temperature discrimination along a single optical fiber

The considered Optical Fiber Sensors (OFSs) combine the analysis of the scattering phenomena (Brillouin, Rayleigh, and Raman) to reflectometry technologies to provide spatially and time-resolved measurements of temperature or strain along the optical fibers. Actually their main limitation remains their capacity to discriminate between the relative contributions of the temperature and the strain to the observed change of the backscattered light of an optical fiber. Different solutions have been developed to achieve this discrimination such as combining two types of interrogators based on two scattering phenomena: Brillouin and Raman [121], or Rayleigh and Brillouin [122], or Raman and Rayleigh [123]. Another solution relies on the use of Polarization Maintaining (PM) fibers as explained in chapter 1. A third mitigation technique has been suggested in literature: it appears possible to use a single-mode optical fiber having a Brillouin signature characterized by several Brillouin peaks [118], [124], these peaks being associated with different strain and temperature sensitivities. Such fiber can be done by using exotic core doping or complex refractive index profile. The major inconvenient of this approach is the resulting increase of the fiber linear attenuation and a poor compatibility with telecom-grade equipment. To compensate the dispersion of Telecom-grade G652 fibers, CORNING has developed the NZ-dispersion LEAF fiber, that exhibits a Brillouin signature with two frequency peaks and low linear attenuation. However, previous research showed that the uncertainties associated to the sensor discrimination remains too large for practical use [124]. In this PhD thesis, we have designed, and manufactured a low-loss single-mode specialty optical fiber. Its Brillouin spectra should have several frequency peaks, to improve the discrimination capability between the strain and temperature influences along several kilometers.

3.1 Selected approach

To design a fiber structure able to achieve the discrimination, it is mandatory to be able to predict the Brillouin response of a given fiber architecture. For this purpose, the simulation tools presented and validated in the Chapter 2 have been used. Regarding the number of variables that are known to affect the fiber signature, a sole experimental and iterative approach sounds unrealistic while the use of simulation should be more timely efficient and should allow to explore a lot of possible structures before selecting the one to be manufactured by iXBlue Photonics.

The simulation strategy to develop this optical fiber is, first, to test the potential of the various fiber core and cladding compositions which are classically used in the Telecom domain. We decided to push the use of Germanium and Fluorine to guaranty low-loss performance at around 1550 nm. Then the fiber structure, especially its refractive index profile, has been optimized to obtain the most interesting Brillouin features. To perform this, we have defined the allowed variation range for each of the free parameters in our model (detailed in part 3.2). To this aim, we used an optimization method close to the Monte-Carlo ones. The statistical analysis of the obtained results strengthens the robustness of the selected fiber architectures. As it will be further detailed, from this theoretical analysis, two fiber structures differing in terms of composition and refractive-index profile, have been selected for manufacturing. At this stage, it was decided to also investigate the impact of the drawing parameters on the Brillouin signature of these two fibers to understand how this manufacturing step affects the fiber sensor capacities. Furthermore, this also evaluate the robustness of the simulated Brillouin spectrum versus the fiber manufacturing process. After fabrication, the characteristics of each fiber sample have been measured and compared to the simulation outputs. Finally, we studied the performances of these different fibers in terms of discrimination.

In parallel to this research activity, we evaluated the potential of another solution based on a novel interrogator that appears on the market during the PhD thesis. This single-ended interrogator from Viavi-Solutions combines Rayleigh and Brillouin measurements to discriminate the relative contributions of temperature and strain along a single optical fiber. We investigate the capability of this sensor to maintain its performances when the sensing optical fiber is irradiated with either γ-rays or X-rays.

3.2 Optimization of the Brillouin signature of low-loss single mode optical fibers

3.2.1 Simulation parameters and range of interest

To develop a fiber with several Brillouin frequency peaks, we got inspired by the results of the section 2.8 were it was shown that some of the tested samples exhibited experimental Brillouin signatures with three clear frequency peaks. Based upon this knowledge, we have investigated the impact of varying the following parameters:

- The GeO_2 concentration in the fiber core: variation between 10 and 38.5 ωt%.
- The F concentration in the cladding: variation between 0 and 2 ωt%.
- The core size: variation of the core radius from 1.2 to 2 µm.
- The trapezoidal core refractive-index profile: the size ratio for the top over the base was comprised between 0.3 and 0.9.
- Radius of the doped cladding: from size of the core radius to 25 µm

All these parameters affect the fiber refractive index profile (RIP) and the Acoustic Velocity Profile (AVP). Figure 3.1 illustrates how the RIP and the AVP evolve when these parameters vary: in a) the RIP (blue line) and the AVP (red line) are given for a step-index fiber doped with 35 ωt% of GeO_2 in core (diameter of 3.6µm, 2 ωt% of fluorine in the cladding (radius of 25µm). In b) the RIP (blue line) and the AVP (red line) of another fiber doped at 10 ωt% of GeO_2 in the core (2.6 µm diameter) and with a ratio for the trapezoidal core of 0.3. Inside these two extreme simulation cases we have evaluated the characteristics of 176 fibers, calculating their Brillouin signatures to identify the structures leading to several Brillouin frequency peaks.

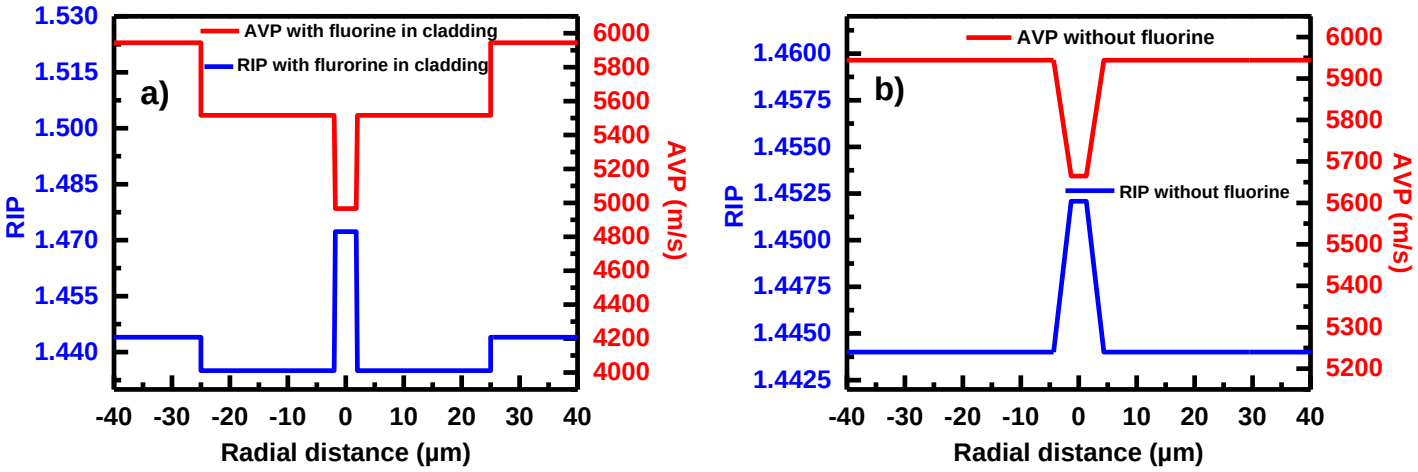

Figure 3.1: RIP (blue line) and AVP (red line) of the two extreme fiber architectures investigated by simulation.See text for more details

In particular, we obtained

- only one structure with an unique Brillouin frequency peak
- four structures having two Brillouin frequency peaks,
- 152 cases with three Brillouin frequency peaks,
- 19 fiber structures with four Brillouin frequency peaks.

3.2.1.1 Amplitude of the Brillouin frequency peak:

To select the best configuration(s) we have studied the effect of the different variables on the amplitude of the different Brillouin frequency peaks. Indeed, this amplitude is crucial as in the case of spontaneous Brillouin interrogators (BOTDR) for which the amplitude should be sufficient to maintain a good signal to noise ratio. Figure 3.2 and Figure 3.3 show the dependences of the peak amplitudes to the GeO_2 concentration and the core radius, respectively. For both figures, in a) is represented the amplitude of the first Brillouin frequency peak ν_1, in b) the amplitude of the second Brillouin frequency peak ν_2, and in c) and d) the amplitude of the third and fourth Brillouin frequency peaks ν_3 and ν_4, respectively. An opposite behavior is observed regarding the amplitudes of the first and the third Brillouin frequency peaks. Indeed, the amplitude of ν_1 increases with the germanium concentration

while the one of ν_3 decreases with it. The same trend can be observed when the size of the core changes: the amplitude of ν_1 increases with the core size while the one of ν_3 decreases. Regarding the second Brillouin frequency peak ν_2, increasing the GeO_2 concentration reduces its amplitude, the behavior is the same concerning the effect of the core size. Finally, the peak amplitude of the fourth Brillouin frequency seems not influenced by the concentration of GeO_2. However, a slight effect of the core size on the amplitude of ν_4 can be observed (see Figure 3.3). The size of the doped cladding, the fluorine concentration, and the trapezoidal shape ratio do not influence the amplitudes of the different Brillouin frequency peaks.

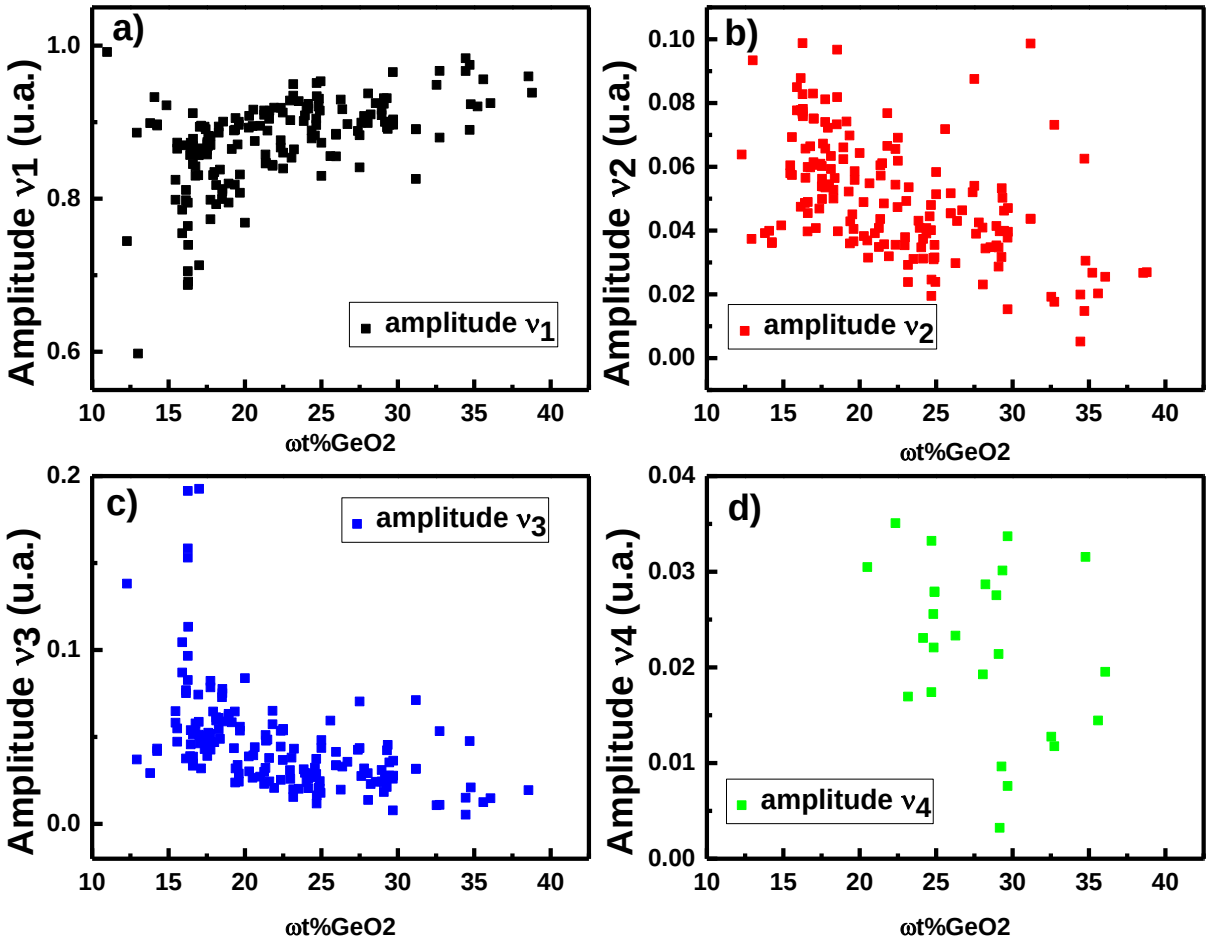

Figure 3.2: impact of the germanium core concentration on the amplitude of the Brillouin frequency peak, in a) the first peak, in b) the second peak, in c) the third peak, and in d) the fourth peak

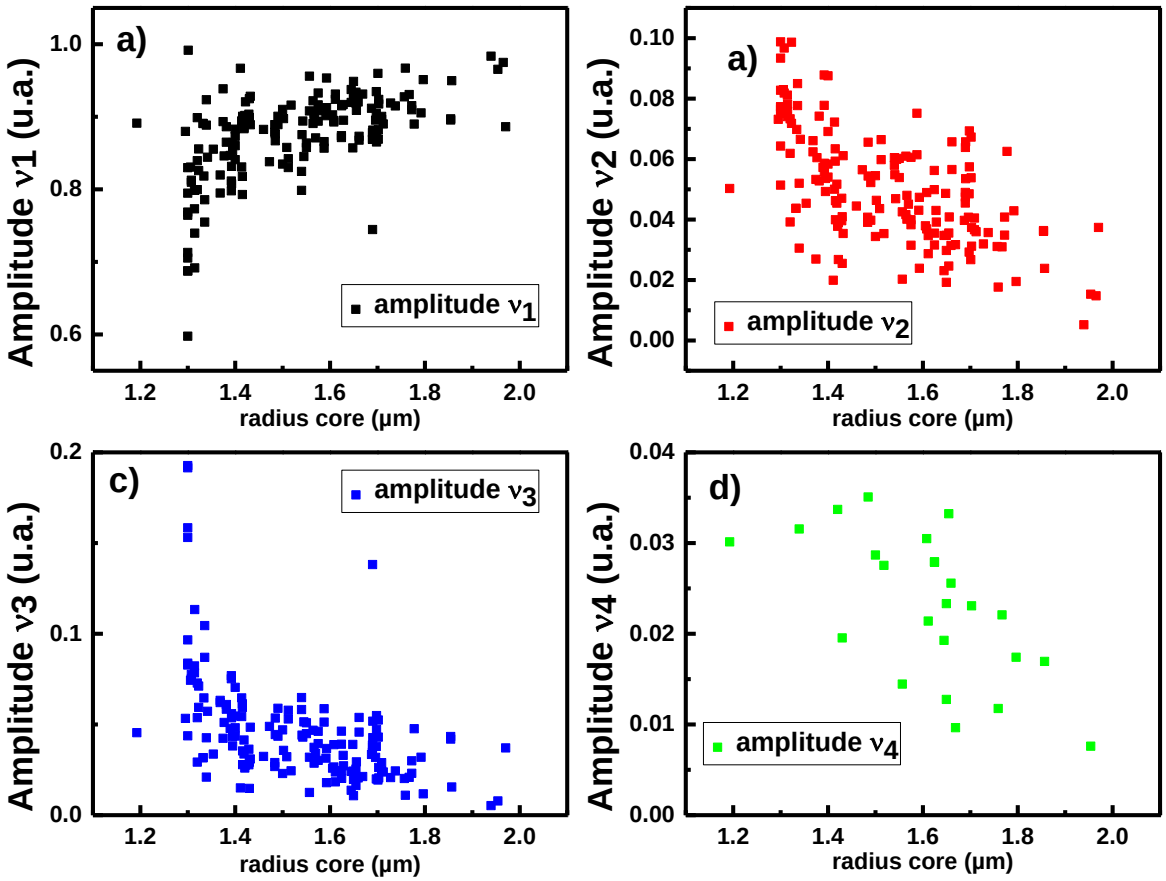

Figure 3.3: impact of the core radius on the amplitude of the Brillouin frequency peak. In a) the first peak, in b) the second peak, in c) the third peak, and in d) the fourth peak

3.2.1.2 Strain and Temperature coefficients

In second time, we have studied the effect of those different parameters on the strain and temperature coefficients. Figure 3.4 gives the dependence of the strain coefficient in a) and the evolution of the temperature coefficient in b) with the GeO_2 core concentration. The black, red, blue, and purple dots correspond to the coefficients of the Brillouin frequency peaks ν_1, ν_2, ν_3, and ν_4 respectively. These results show that the strain and temperature coefficients decrease for larger GeO_2 concentrations. To obtain the best performance in terms of discrimination, it is important to combine the coefficients with biggest value and with the largest difference. Figure 3.5 shows how the difference between the strain coefficients, expressed in percentage, depends on the core size. In a) is given the difference between $C\varepsilon_1$ and $C\varepsilon_2$, and in b) the difference between the $C\varepsilon_1$ and $C\varepsilon_3$. The smaller is the core diameter

the largest is the difference. The other tested variables don't influence so strongly the difference between the strain and temperature coefficients.

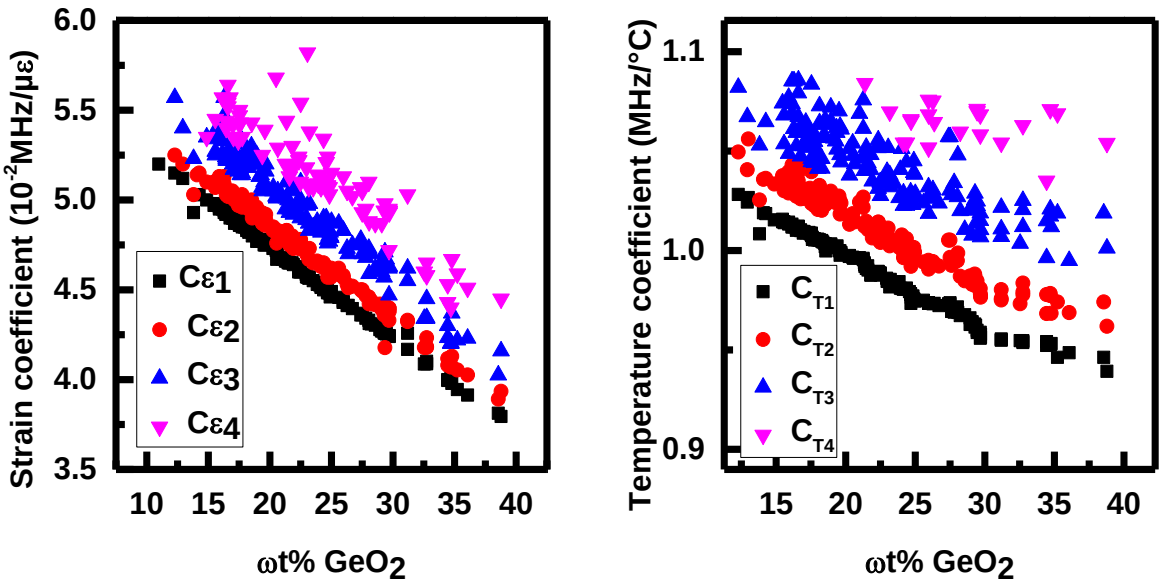

Figure 3.4: Impact of the GeO_2 concentration on: a) strain coefficient and, b) temperature coefficient

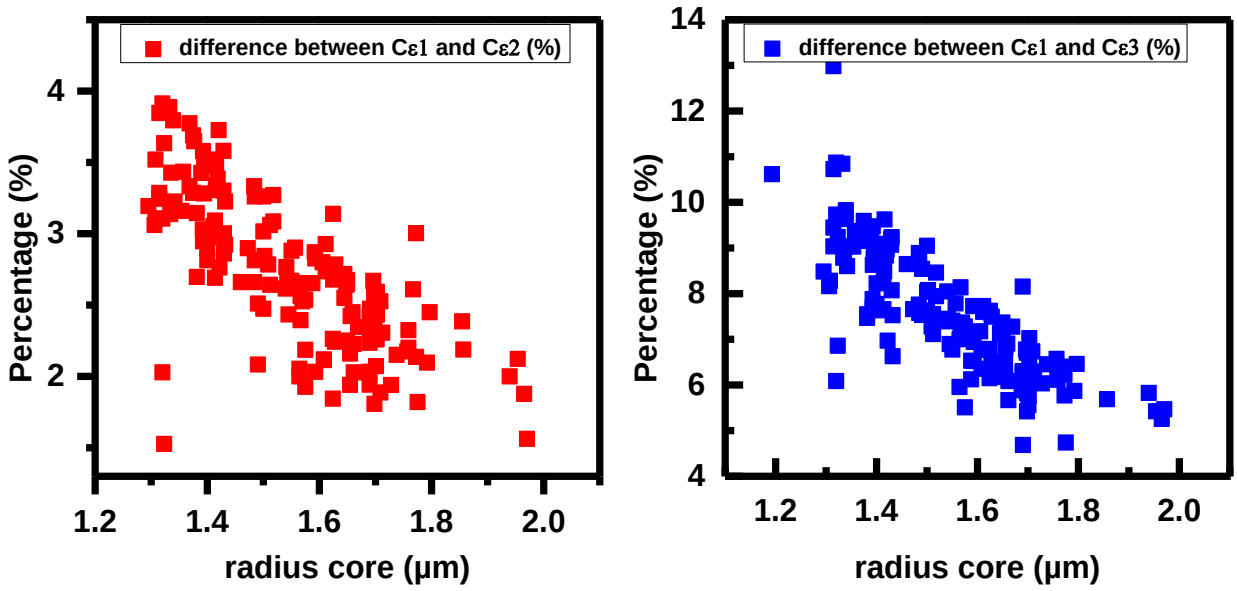

Figure 3.5: Impact of the radius core on: a) the difference between the first and the second strain coefficients and, b) the difference between the first and the third coefficients

From this preliminary set of results, it has been decided to reduce the variable ranges as follow:

- GeO_2 concentration in the fiber core: variation between 15 and 18 ωt%.
- F concentration in the cladding: variation between 0 and 0.2 ωt%.
- Core size: variation of the core radius from1.3 to 1.6 µm.
- Size ratio for the top over the base was comprised between 0.7 and 0.9.
- Size of the cladding radius doped from size of the core radius to 25 µm

We reduced the maximum allowed quantity of GeO_2 to ensure sufficient amplitudes for the second and third Brillouin frequency peaks while achieving simultaneously high values of temperature and strain coefficients. The core radius is reduced to optimize the difference between the strain sensitivities of the three peaks.

3.2.2 Fiber optimization for Temperature / Strain discrimination

Within the reduced range of variation, another simulation run (90 cases) has been performed to optimize the optical fiber structure, with the following results obtained:

- 10 fibers possess signatures with two Brillouin frequency peaks,
- 2 fibers have Brillouin spectra with four frequency peaks,
- 78 fibers exhibit Brillouin spectra with three frequency peaks.

These two simulation cycles allowed to estimate the robustness of the fiber structure needed to obtain the multi-peak response. Indeed 86% of our 266 simulation cases give Brillouin signature with the needed three frequency peaks. A signature with four peaks can seem promising for the discrimination but the low occurrence of such case (8 %) demonstrate the weak robustness of those profiles in view of their manufacturing.

In terms of strain and temperature coefficients, Table 3.1 reports the analyzed amplitude of variation for each of these coefficients during the second cycle of simulation. It is worthwhile to note that the variation range of the strain coefficient is lower than 10 kHz/µε for the 90

cases and 35 kHz/°C for the temperature coefficient. This confirms the robustness of the fiber response versus the simulation criteria.

TABLE 3.1: MAXIMUM DIFFERENCE FOR THE TEMPERATURE AND THE STRAIN COEFFICIENTS OBSERVED FOR THE 90 FIBER STRUCTURES MODELED DURING THE SECOND RUN OF SIMULATION

$\Delta C\varepsilon_1$ (kHz/με)	$\Delta C\varepsilon_2$ (kHz/με)	$\Delta C\varepsilon_3$ (kHz/με)	ΔC_{T1} (kHz/με)	ΔC_{T2} (kHz/με)	ΔC_{T3} (kHz/με)
5.0	2.2	8.3	10.1	20.0	34.2

3.2.3 Selection of two promising fiber structures

The final objective of the simulation work was to select two different fiber profiles in view of their manufacturing by iXBlue Photonics. It was decided that the first fiber should contain germanium in its core and fluorine in its cladding, while the second should have a Ge-doped core and a pure silica cladding. To select both the targeted fiber composition and RIPs, the criteria was their theoretical capacities of discrimination between the strain and temperature distributions.

3.2.3.1 Germanium and fluorine doped fiber

Composition:

Considering the previous simulation results, we selected the fiber structure with the Ge and F doping, its main characteristics are listed in TABLE 3.2. Figure 3.6 illustrates in a) its theoretical RIP and in b) its theoretical AVP.

TABLE 3.2: CHARACTERISTICS OF THE GEF DOPED FIBER

GeO_2 ωt%	F ωt%	Core diameter (μm)	Ratio between the top and the base	Cladding diameter (μm)
17.33	0.16	3.2	0.78	23.9

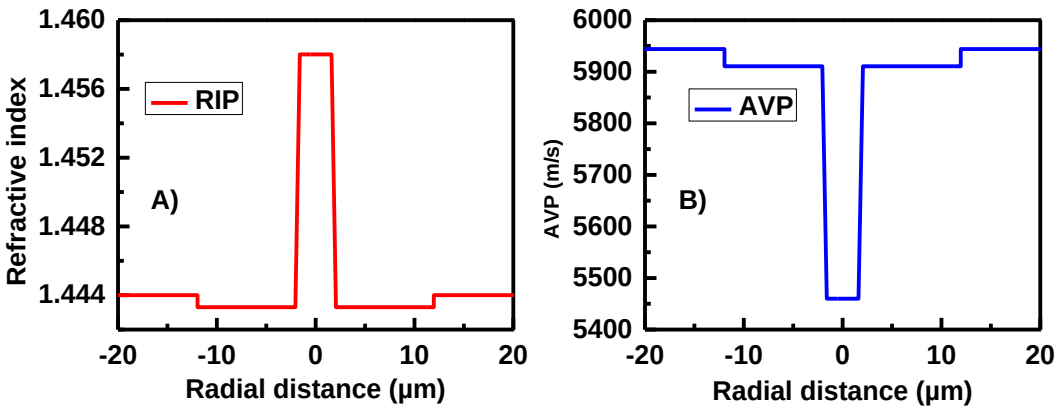

Figure 3.6: a) Theoretical Refractive Index Profile (RIP) and b) acoustic velocity (AVP) of the GeF-doped fiber

Brillouin spectrum and coefficient:

Knowing the radial distributions of the two dopants, we calculated the normalized Brillouin spectrum (see Figure 3. 7) thanks to the simulation codes detailed in Chapter 2. We observe the presence of the three Brillouin frequency peaks as expected. Their strain and temperature coefficients are detailed in TABLE 3.3. A maximum difference of 16.0% between the $C\varepsilon_1$ and $C\varepsilon_3$ and a maximum difference of 5.0% between C_{T1} and C_{T3} have been calculated.

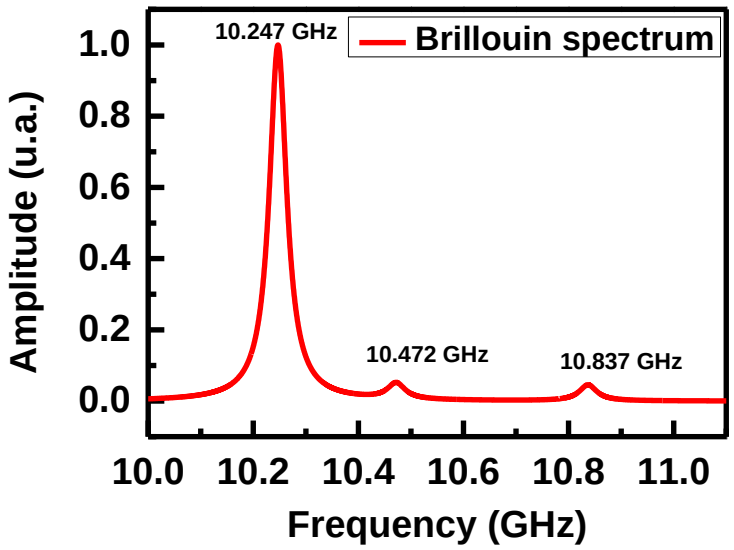

Figure 3. 7: Calculated Brillouin spectrum of the GeF-doped fiber

TABLE 3.3: SENSOR CHARACTERISTICS OF THE GEF-DOPED FIBER

	Frequency (GHz)	Cε (MHz/με)	C_T (MHz/°C)
Peak 1	10.247	0.0447	1.01
Peak 2	10.472	0.05	1.03
Peak 3	10.837	0.0519	1.06

Fiber light guiding properties:

Finally we have modeled the fiber guiding properties at 1310 nm and 1550 nm. TABLE 3.4 summarizes the simulated spectral dependence of the macrobending losses. Due to the limited size of the core, it was important to verify that the fiber could be practically used and then verify that the bending losses at 1.55µm remain negligible. It can be seen that the macrobending losses are negligible, moreover the linear losses are comparable with the SMF28 fiber (0.18 dB/km) [125]

TABLE 3.4: OPTICAL SPECIFICATION OF GEF-DOPED FIBER

	1310	1550
Linear loss (dB/km)	0.33	0.19
Bending loss (radius diameter:32 mm for 1 turn)	< 0.01dB/km	< 0.01dB /km
Confinement Factor (%)	90.8	85.1
MFD	5.0	5.9 µm
Dispersion (ps/km.nm)	-25.1	-13.0
Zero dispersion wavelength	1841 nm	
Cutoff wavelength	900 nm	

3.2.3.2 Germanium doped fiber

TABLE 3.5 describes the Ge-doped fiber that possesses a pure silica cladding (instead of a F-doped cladding for the GeF sample). Figure 3.8 shows its theoretical RIP in a) and VAP in b).

TABLE 3.5: CHARACTERISTICS OF THE GERMANIUM DOPED

GeO_2 ωt%	F ωt%	Core diameter (µm)	Ratio between the top and the base	Cladding diameter (µm)
17.5	0	2.8	0.8	62.5

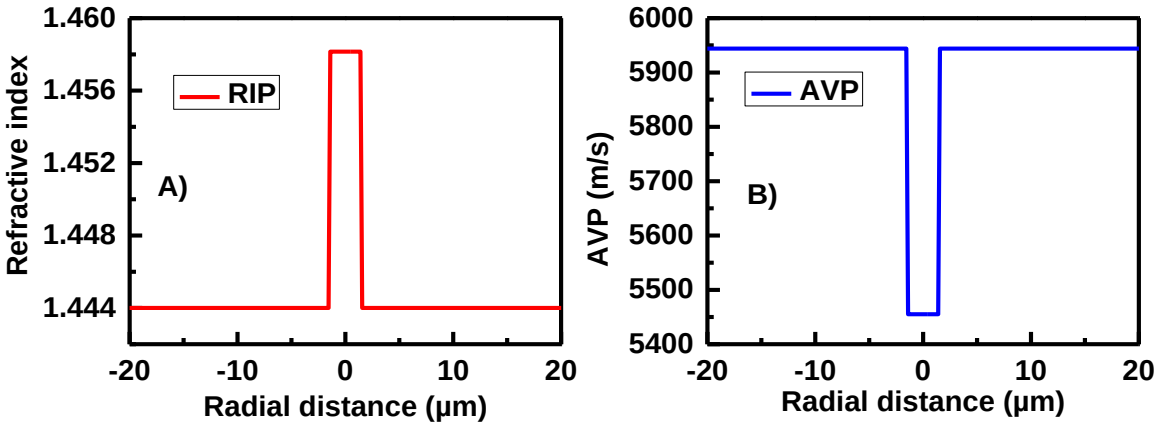

Figure 3.8: a) theoretical refractive index profile (RIP) and b) acoustic velocity profile (AVP) of the Ge-doped fiber

Figure 3. 9 gives the calculated and normalized Brillouin spectrum of this optical fiber highlighting the three different Brillouin peak frequencies. TABLE 3.6 listed the strain and the temperature coefficients associated to the three peaks. The maximum difference is 10% between the $C\varepsilon_1$ and $C\varepsilon_3$ coefficients and 8% between the C_{T1} and C_{T3} coefficients.

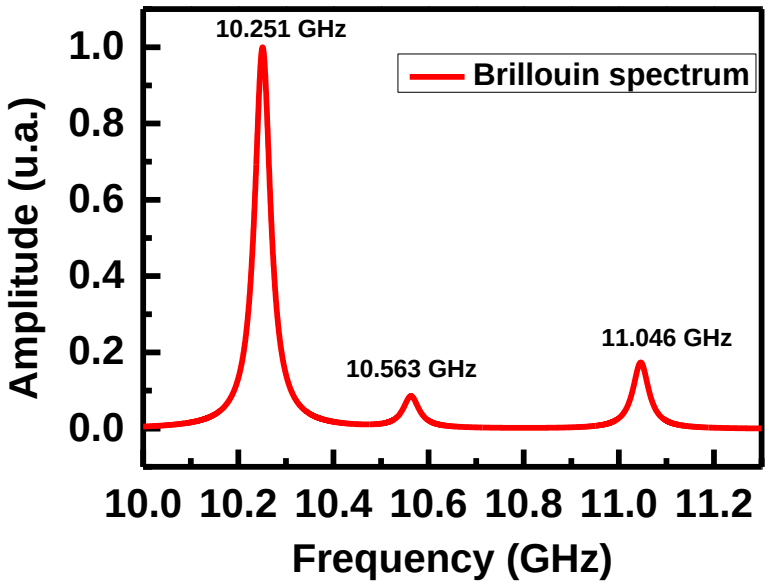

Figure 3. 9: Calculated Brillouin spectrum of the Ge-doped fiber

TABLE 3.6: SENSOR CHARACTERISTICS OF THE GE-DOPED FIBER

	Frequency (GHz)	Cε (MHz/με)	C_T (MHz/°C)
Peak 1	10.251	0.0484	1.00
Peak 2	10.563	0.0496	1.04
Peak 3	11.046	0.0538	1.08

Fiber light guiding properties:

In terms of macro-bending sensitivity, we calculated an excess loss of 20 dB/km at 1.55µm for a curvature radius of 32mm as given in TABLE 3.7, it correspond to a losses of 4×10^{-3} dB for 1 turn. This value is acceptable in comparison with the Leaf fiber which present a bending loss of 0.5 dB for one turn of radius of 32 mm at 1500 nm [126].

TABLE 3.7: OPTICAL SPECIFICATION OF GE-DOPED FIBER

	1310 nm	1550 nm
Linear loss (dB/km)	0.33	0.19
Bending loss (radius diameter: 32 mm for 1 turn)	<0.01 dB/km	20 dB/km
Confinement Factor (%)	80.3	70.5
MFD	5.2 µm	7.0 µm
Dispersion (ps/km.nm)	-41.3	-23.0
Zero dispersion wavelength	1813 nm	
Cutoff wavelength	780 nm	

3.2.3.3 Tolerance study

The selected RIP for the fibers are quite complex, as a consequence we have to ensure that the interesting sensing properties of the fiber are maintained even if the RIPs of the manufactured fiber differ slightly (within the process uncertainties) of the ideal ones. We then performed a tolerance study considering that the possible modifications (iXblue's feedback) may occur during the manufacturing (which correspond to variations 1, 2, 3, and 4 in Figure 3.10) with respect to the theoretical profile:

- The experimental RIP may be more triangular in shape than targeted
- Possible deviations from the theoretical ratio between the top and the base of the core.
- Slight variation of the cladding and core sizes

These variations could be, for example, explained by the diffusion of the dopants (fluorine or germanium) during the preform deposition and the fiber drawing. The fiber preforms have been realized using the modified chemical vapor deposition (MCVD) process [127]. An example of the impact of these possible variations on the fiber RIP is illustrated in Figure 3.10 where the dashed line represents the theoretical RIP and the colored lines the calculated possible deviations due to the manufacturing process.

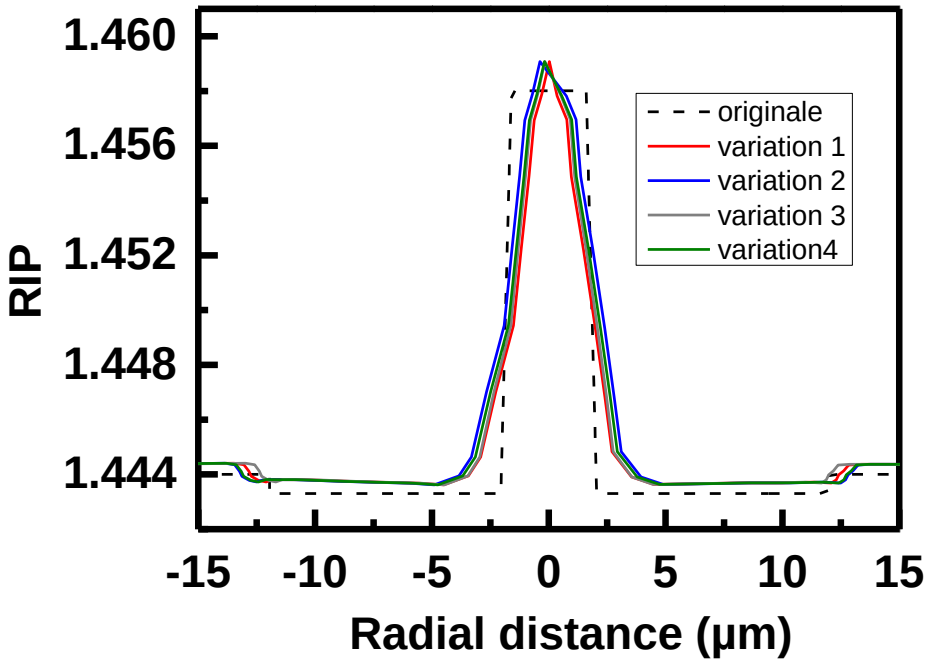

Figure 3.10: modified RIP by transformation for the manufacturing GeF-doped fiber

Figure 3.11 illustrates the different Brillouin spectra associated to the four possible RIPs and in TABLE 3.8 the different strain and temperature coefficients of the different peaks are reported. In all cases, three Brillouin frequency peaks can be observed, however with a lower amplitude for the third Brillouin frequency peak. Concerning the strain coefficient we obtain the largest difference with the original fiber of: 13% for $C\varepsilon_1$, 10% for $C\varepsilon_2$, and 14 % for $C\varepsilon_3$. In terms of temperature coefficients the maximum difference is: 1% for C_{T1}, 3% for C_{T2}, and 3% for C_{T3}. From this tolerance study, the fiber RIP for the GeF has been validated in view of its fabrication. Similar approach was applied for the Ge-doped fiber that leads to the validation of its RIP too.

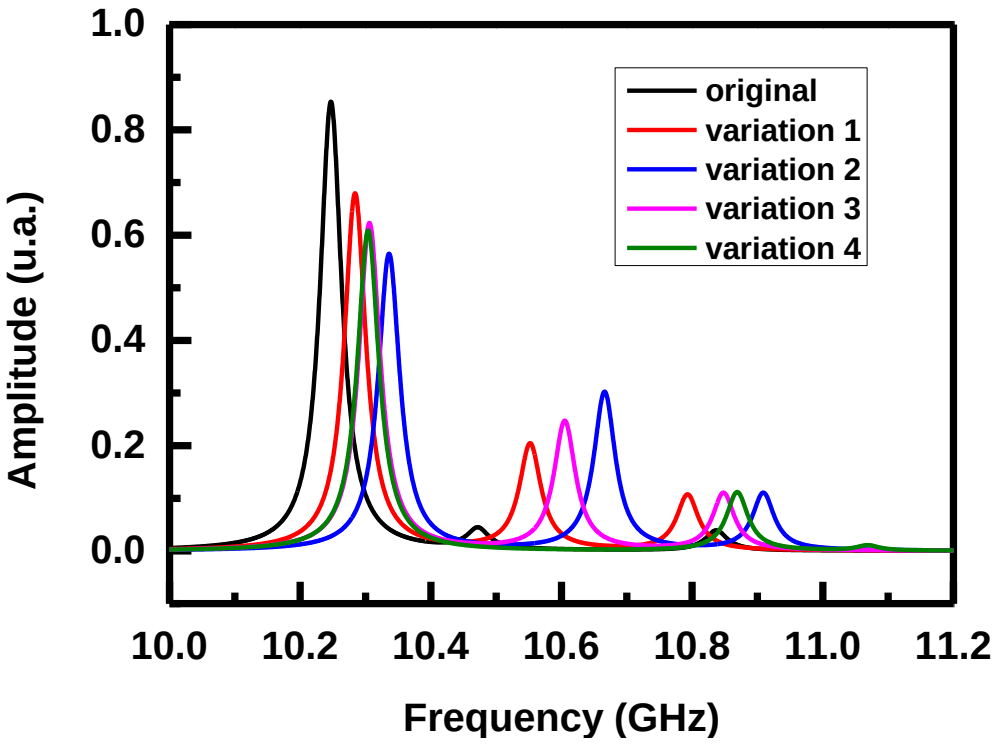

Figure 3.11: Comparison between the theoretical Brillouin spectrum of the GeF-doped fiber with those of the modified RIPs

TABLE 3.8: STRAIN AND TEMPERATURE COEFFICIENTS ASSOCIATED WITH THE FOUR MODIFIED RIPS AND AVPS.

	$C\varepsilon_1$ (MHz/με)	$C\varepsilon_2$ (MHz/με)	$C\varepsilon_3$ (MHz/με)	C_{T1} (MHz/°C)	C_{T2} (MHz/°C)	C_{T3} (MHz/°C)
Original	0.045	0.050	0.052	1.01	1.03	1.06
Variation 1	0.049	0.051	0.053	1.00	1.04	1.08
Variation 2	0.049	0.052	0.055	1.01	1.05	1.07
Variation 3	0.049	0.051	0.053	1.01	1.06	1.09
Variation 4	0.051	0.055	0.059	1.01	1.04	1.06

3.3 Simulation of the performances of the manufactured optical fibers

Different sets of the two fibers have been produced from the same preform with different drawing tensions and drawing speeds with the idea to quantify the drawing effect on their Brillouin responses. Three different drawing conditions (speed and tension) have been tested for each kind of fibers for a total of six samples. Changing the drawing speed is known to affect the sizes of the core and of the cladding.

3.3.1 Germanium -doped fiber

The first produced optical fiber is the germanium doped fiber. TABLE 3.9 details the characteristics of the samples differently drawn: SMFS_Ge1, SMFS_Ge2, and SMFS_Ge3. Figure 3. 12 compares their measured RIPs to the simulated one (detailed in part 3.2.3) and labelled as SMFS_Ge0. The RIP has been measured with the IFA setup (described in chapter 2 part 2.2.5 page 77). The variation of the core and cladding sizes between the samples is due to the applied changes in the drawing speed. The three samples have RIP very close to the theoretical targeted one. We note a slightly larger Δn, typically 15×10^{-3}, for the manufactured fiber to be compared to the ideal value of 14×10^{-3}. The ratio between the top and the bottom of the trapezoidal core is of ~0.4 instead of 0.8.

TABLE 3.9: CHARACTERISTICS OF THE MANUFACTURED GE-DOPED FIBER SAMPLES

Name of sample	Tension drawing (g)	Diameter core size (µm)	Diameter cladding size (µm)	Ge Concentration in core (ωt%)
SMFS_Ge1	40	2.9±0.1	122±1	15.8±0.5
SMFS_Ge2	100	3.0±0.1	125±1	15.8±0.5
SMFS_Ge3	200	3.1±0.1	128±1	15.8±0.5

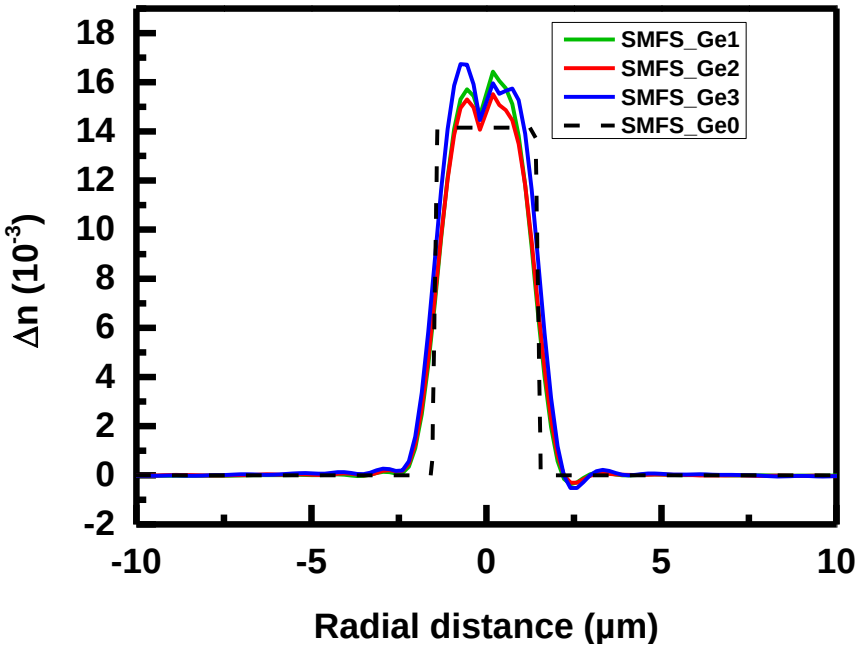

Figure 3. 12: Comparison between the RIPs of the manufactured Ge-doped fiber samples and the theoretical one

3.3.1.1 Theoretical Brillouin spectrum

Thanks to the experimental data provided by iXblue Photonics we have been able to simulate the Brillouin spectrum of the fabricated Ge-doped samples represented in Figure 3.13 and detailed in TABLE 3.10. The three SMFS_Ge samples are associated with a Brillouin signature comprising three frequency peaks. For the first and main Brillouin peak ν_1, a maximum difference of 0.6% is obtained between the ideal profile and real ones, for the second and third peaks ν_2 and ν_3, we calculated 0.8% and 1.1 % of maximum of difference between the theory and the experiments.

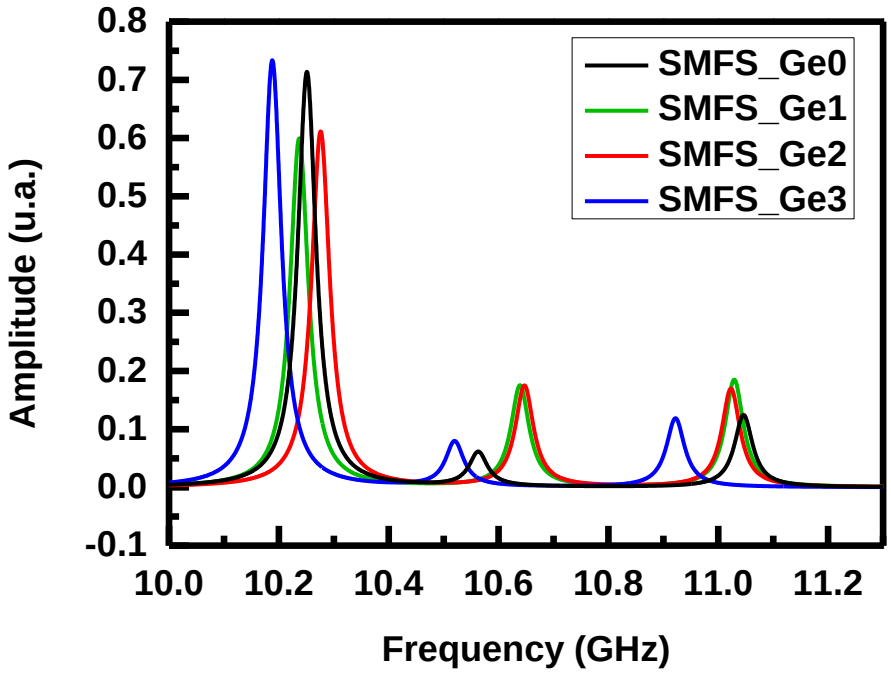

Figure 3.13: Brillouin spectra of the three different manufactured samples of the Ge-doped fiber. The spectrum of the theoretical fiber is given for comparison

TABLE 3.10*:* CALCULATED BRILLOUIN FREQUENCY PEAKS OF THE THREE DIFFERENT MANUFACTURED SAMPLES OF THE GE-DOPED FIBER. THESE DATA ARE COMPARED TO THE IDEAL PROFILE FIBER

Name of sample	ν_1 (GHz)	ν_2 (GHz)	ν_3 (GHz)
SMFS_Ge0	10.251	10.563	11.046
SMFS_Ge1	10.237	10.639	11.029
SMFS_Ge2	10.276	10.647	11.023
SMFS_Ge3	10.188	10.520	10.922

3.3.1.2 Temperature and strain coefficients

Concerning the temperature and strain coefficients of the manufactured Ge-doped fibers, TABLE 3.11 reports their coefficient values for each of the Brillouin frequency peaks and also gives for comparison those calculated for the theoretical fiber (SMFS_Ge0). As we can see, the temperature coefficients are very close for the ideal case and manufactured samples: the difference remains below 0.01 MHz/°C, maximum difference is observed between the

SMFS_Ge0 and the SMFS_Ge3. This good correspondence was expected as the temperature coefficient depends on the fiber composition.

TABLE 3.11: TEMPERATURE COEFFICIENTS OF THE THREE DIFFERENT MANUFACTURED SAMPLES OF THE GE-DOPED FIBER. THE COEFFICIENTS OF THE THEORETICAL FIBER ARE GIVEN FOR COMPARISON

Name of sample	C_{T1} (MHz/°C)	C_{T2} (MHz/°C)	C_{T3} (MHz/°C)
SMFS_Ge0	1.0	1.04	1.08
SMFS_Ge1	1.0	1.04	1.08
SMFS_Ge2	1.0	1.04	1.08
SMFS_Ge3	1.0	1.03	1.07

The same analysis is done for the strain coefficients and the corresponding results are reported in TABLE 3.12. However, it can be observed a maximum difference of 1.2% between the $C\varepsilon_1$ of SMFS_Ge1 and SMFS_Ge0. The maximum difference for the $C\varepsilon_2$ is between the SMFS_Ge0 and the SMFS_Ge2 and the corresponding value is 3.8%, for the $C\varepsilon_3$ this difference is 2.4% and concerns the SMFS_Ge1.

TABLE 3.12: STRAIN COEFFICIENTS OF THE THREE DIFFERENT MANUFACTURED SAMPLES OF THE GE-DOPED FIBER. THE COEFFICIENTS OF THE THEORETICAL FIBER ARE GIVEN FOR COMPARISON

Name of sample	$C\varepsilon_1$ (MHz/με)	$C\varepsilon_2$ (MHz/με)	$C\varepsilon_3$ (MHz/με)
SMFS_Ge0	0.0484	0.0496	0.0538
SMFS_Ge1	0.0484	0.0513	0.0551
SMFS_Ge2	0.0490	0.0515	0.0547
SMFS_Ge3	0.0480	0.0500	0.0531

3.3.2 GeF-doped fiber

Figure 3.14 compares the RIP of the manufactured SMFS_F samples of the GeF-doped fiber with the one of its theoretical structure (SMFS_F0). TABLE 3.13 reports the main

characteristics of those samples, here again obtained from the same preform by varying the drawing tension and speed. As for the SMFS_Ge sample, the theoretical and real RIPs are close. The measured ratio between the top and the bottom of the trapezoidal core is of ~0.4 (0.64 targeted). Concerning the refractive index, we obtain a Δn of 16×10^{-3} SMFS_F1 and SMFS_F3, and a Δn of 17×10^{-3} for SMFS_F3, for the SMFS_F0 we have targeted a Δn of 14.5×10^{-3} at 1550 nm.

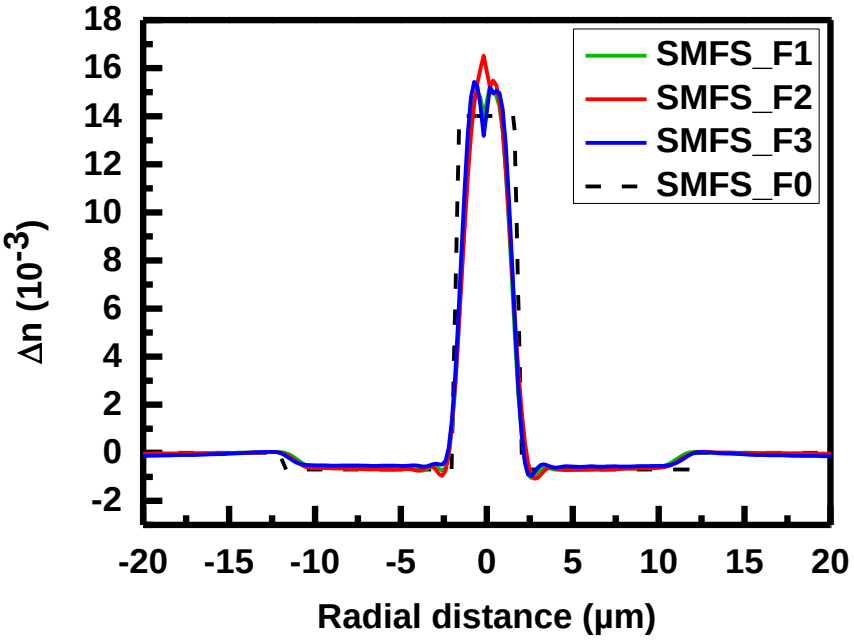

Figure 3.14: Comparison between the RIP of the manufactured GeF-doped fiber samples and the ideal one (SMFS_F0)

TABLE 3.13: CHARACTERISTICS OF THE MANUFACTURED GEF-DOPED FIBER SAMPLES

Name of sample	Tension drawing (g)	diameter core size (µm)	Cladding diameter size (µm)	Ge Concentration in core	F Concentration in cladding	Diameter doped cladding (µm)
SMFS_F1	40	3.0±0.1	122±1	15.8±0.5	0.16±0.05	23.8
SMFS_F2	70	3.1±0.1	125±1	15.8±0.5	0.16±0.05	24.2
SMFS_F3	200	3.2±0.1	128±1	15.8±0.5	0.16±0.05	24.6

3.3.2.1 Theoretical Brillouin Spectrum

From the measured RIP, we calculated the Brillouin spectrum of each manufactured sample and compared them to the theoretical one in Figure 3.15. The exact values of the different Brillouin frequency peaks are given in TABLE 3.14 for all samples. All samples present Brillouin signature with three Brillouin frequency peaks. Compared to the targeted profile, the experimental ones present larger amplitudes for the second and the third peaks. However, the amplitude of the first peak is lower than expected. In terms of peak frequencies, the largest difference between the theoretical and the real fibers are: 0.2%; 1.7% and 1.7% for the first, second and third Brillouin frequency peaks, respectively. As for the first fiber, the experiments are very close to the simulation.

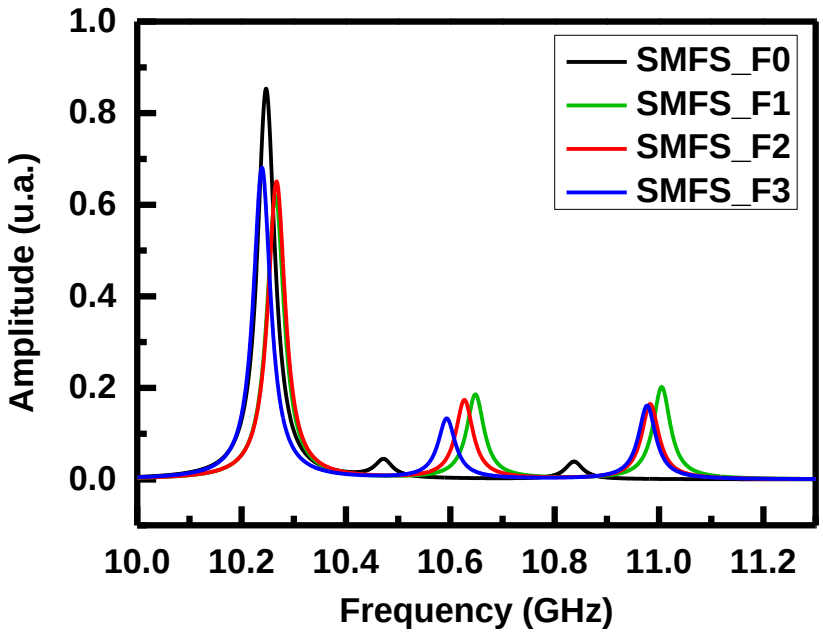

Figure 3.15: Simulated Brillouin spectrum of the germanium fluorine doped fiber samples

TABLE 3.14: BRILLOUIN FREQUENCY PEAK OF THE GERMANIUM FLUORINE DOPED FIBER SAMPLES

Name of sample	ν_1 (GHz)	ν_2 (GHz)	ν_3 (GHz)
SMFS_F0	10.247	10.472	10.837
SMFS_F1	10.265	10.648	11.005
SMFS_F2	10.267	10.627	10.983
SMFS_F3	10.239	10.593	10.977

3.3.2.2 Temperature coefficients

We have compared the temperature coefficients calculated for the different Brillouin peaks of the manufactured SMFS_F samples to those calculated for the ideal fiber. All the coefficient values are detailed in TABLE 3.15, the biggest difference of 1.9 % corresponds to a 0.02Mhz/°C difference between the C_{T2} of SMFS_F1 and the SMFS_F0.

TABLE 3.15: TEMPERATURE COEFFICIENTS OF THE THREE DIFFERENT MANUFACTURED SAMPLES OF THE GEF-DOPED FIBER. THE COEFFICIENTS OF THE THEORETICAL FIBER ARE GIVEN FOR COMPARISON

Name of sample	C_{T1} (MHz/°C)	C_{T2} (MHz/°C)	C_{T3} (MHz/°C)
SMFS_F0	1.01	1.03	1.06
SMFS_F1	1.00	1.05	1.07
SMFS_F2	1.00	1.04	1.07
SMFS_F3	1.00	1.03	1.07

3.3.2.3 Strain coefficients

We have then calculated the values of the strain coefficients for the manufactured samples and compare them with those from ideal profile in TABLE 3.16. A maximum difference of 9.6%, 2.6%, and 6.0% are observed for the $C\varepsilon_1$, $C\varepsilon_2$, and $C\varepsilon_3$ respectively with the SMFS_F0.

TABLE 3.16: STRAIN COEFFICIENTS OF THE THREE DIFFERENT MANUFACTURED SAMPLES OF THE GEF-DOPED FIBER. THE COEFFICIENTS OF THE THEORETICAL FIBER ARE GIVEN FOR COMPARISON

Name of sample	$C\varepsilon_1$ (MHz/με)	$C\varepsilon_2$ (MHz/με)	$C\varepsilon_3$ (MHz/με)
SMFS_F0	0.0447	0.050	0.0519
SMFS_F1	0.0483	0.0513	0.0550
SMFS_F2	0.0490	0.0513	0.0546
SMFS_F3	0.0486	0.0510	0.0542

3.3.3 Partial Conclusion

The objective was to create a fiber sensor which is able to discriminate the strain and the temperature changes along a single optical fiber. To achieve this, we have exploited the simulation tools validated in chapter 2 to statistically study the impact of different variables such as the Ge and F dopant concentrations, the fiber refractive-index profile on the Brillouin response. Basing on the existing results given in Chapter 2, we first define the variation ranges for these different variables and then performed a first cycle of 176 simulations. As output, 152 simulations correspond to fiber structures associated with Brillouin spectra comprising three clearly discernable peaks. Moreover, we have seen that the Ge concentration influences the peak amplitude as well as the values of the strain and temperature coefficients. The core size influences it too and also the relative strain coefficients between the Brillouin frequency peaks. From this first step, it has been decided to perform another cycle of 90 simulations, reducing the possible variation range for those parameters. We have then obtained 78 fibers presenting Brillouin spectra with three peaks. This statistical approach also allows us to test the robustness of our approach as 86% of the 266 simulation cases results in spectra with three Brillouin peaks. From this data set, we have selected two structures of single-mode fiber, the first one is a Ge-doped fiber, and the second one Ge-doped core fiber with F-doped cladding. From their theoretical RIPs, a tolerance study has been done using as input the possible process variations expected by iXblue. This confirmed us that the chosen RIPs are robust, and that even considering the manufacturing uncertainties, the Brillouin signature with the three peaks should be maintained, with strain and temperature coefficients close to those targeted.

Finally, the two structures have been realized as preforms and from each preform iXblue has produced three different samples by varying the drawing tension and speed, allowing to characterize their influence on the Brillouin responses. The RIP of each sample has been measured with the IFA and using these real RIPs, the expected Brillouin responses have been compared to those predicted for the ideal fiber profile. Next step consists in characterizing experimentally the response of each sample and compare those results to our predictions.

3.4 Experiments: Multi-peaks fibers

3.4.1 Qualification of the optical fibers

3.4.1.1 Losses

For their characterization, IXblue Photonics packaged 100 m of each fiber by coiling it on a standard support with a diameter of 15 cm. The losses of these fibers have been measured at 1310 nm and 1550 nm using an Optical Time Domain Reflectometer (OTDR) from Viavi solution [128]. Figure 3.16 shows the OTDR traces at 1.55µm (black line) and 1.31µm (blue line) for the SMFS_Ge1 sample. The measured attenuations are detailed in TABLE 3.17. The SMFS_Ge fiber has losses around 1 dB/km with the highest value of 1.36 dB/km for the SMFS_Ge1 at 1.31 µm. Concerning the SMFS_F samples the losses are globally slightly lower than for the SMFS_Ge sample, highest attenuation being also measured for the SMFS_F1 at 1.31 µm. This result is easily explained, indeed, the attenuation is higher at 1.31 µm than 1.55 µm [128] due to the wavelength dependence of the Rayleigh losses. Moreover, the SMFS_Ge1 has a smallest core diameter with a similar Δn compared to the SMFS_Ge2 and SMFS_Ge3, so the effect of the bending is more important in this case [129], [130]. We observe the same phenomenon for the case of SMFS_F samples. These attenuation values are sufficient for sensing on long distances, typically using an interrogator with an optical budget of 10 dB we can perform a strain or temperature measurement over a range of 10 km.

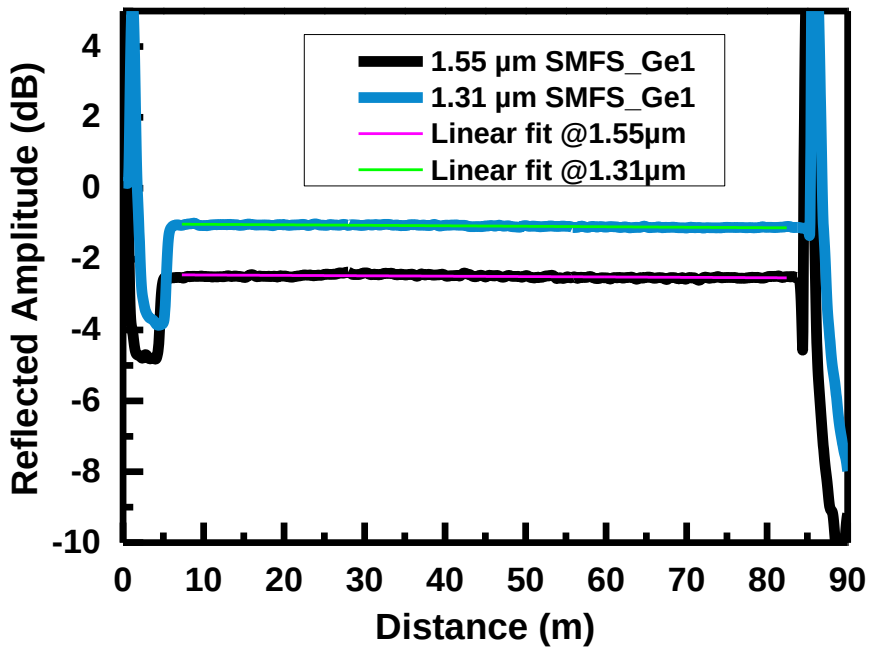

Figure 3.16: Measured losses by OTDR of the SMFS_Ge1 sample at the two telecom wavelengths 1310 and 1550 nm

TABLE 3.17: MEASURED ATTENUATIONS FOR THE SMFS_GE AND SMFS_F SAMPLES AT 1.31µM AND 1.55µM

Ge-doped fiber		
Theoretical losses without bending	@1.31µm: 0.33 dB/km	@1.55µm: 0.19 dB/km
Sample	Losses @ 1.31µm (dB/km)	Losses @ 1.55µm (dB/km)
SMFS_Ge1	1.36	1.09
SMFS_Ge2	1.17	1.10
SMFS_Ge3	0.98	0.70
GeF-doped fiber		
Theoretical losses without bending	@1.31µm: 0.33 dB/km	@1.55µm: 0.19 dB/km
Sample	Losses @ 1.31µm (dB/km)	Losses @ 1.55µm (dB/km)
SMFS_F1	1.62	1.08
SMFS_F2	0.97	0.71
SMFS_F3	0.60	0.54

3.4.1.2 Germanium Fluorine fiber

3.4.1.2.1 Brillouin spectrum

The first tested samples were the SMFS_F samples. The Brillouin spectrum of each fiber has been measured between 10.0 and 11.5 GHz, with a BOTDA from OZ optics [131]. The pulse was selected at 30 ns. Figure 3.17 presents the spectrum measured by the BOTDA for the SMFS_F1 sample. As predicted by simulation, three Brillouin frequency peaks are observed. Similar responses are measured for the other SMFS_F samples. After the measurement of the Brillouin spectrum, we performed another measurement by focusing on each Brillouin frequency peak. Figure 3.18 shows the measurement by the BOTDA, in a) of

the first Brillouin frequency peak, in b) of the second peak and in c) of the third peak. In this BOTDA configuration we have a frequency step of 0.64 MHz (best resolution) contrary to the first measurement where the frequency step was equal to 3.84 MHz. For each peak we have extracted the Brillouin frequency using a Lorentzian fitting represented in red in Figure 3.18 and given by the following formula:

$$Lorentzian = A * \frac{1}{1 + \left(\frac{\nu - \nu_0}{\frac{\Gamma}{2}} \right)^2} \qquad (3.1)$$

where A is the amplitude, ν and ν_0 are the frequency and the central frequency respectively, and Γ the full width at half maximum (FWHM). For the third peak we have use two Lorentzian fits to calculate its frequency. The same method of calculation has been applied for all fibers. TABLE 3. 18 reports the frequencies of the Brillouin peaks with the associated errors. The error corresponds to the standard deviation of all measurements, indeed, the Brillouin spectra have been measured for 101 different spatial positions. It appears that the frequencies of the second and the third peak decrease with increasing values of the drawing tension and speed (10.610 GHz into 10.574 GHz).

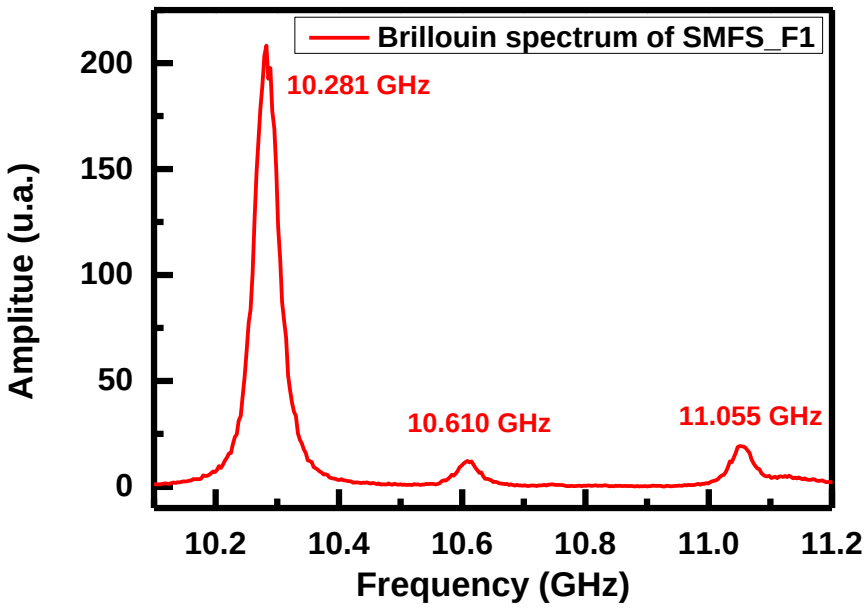

Figure 3.17: BOTDA measured Brillouin spectrum of the SMS_F1

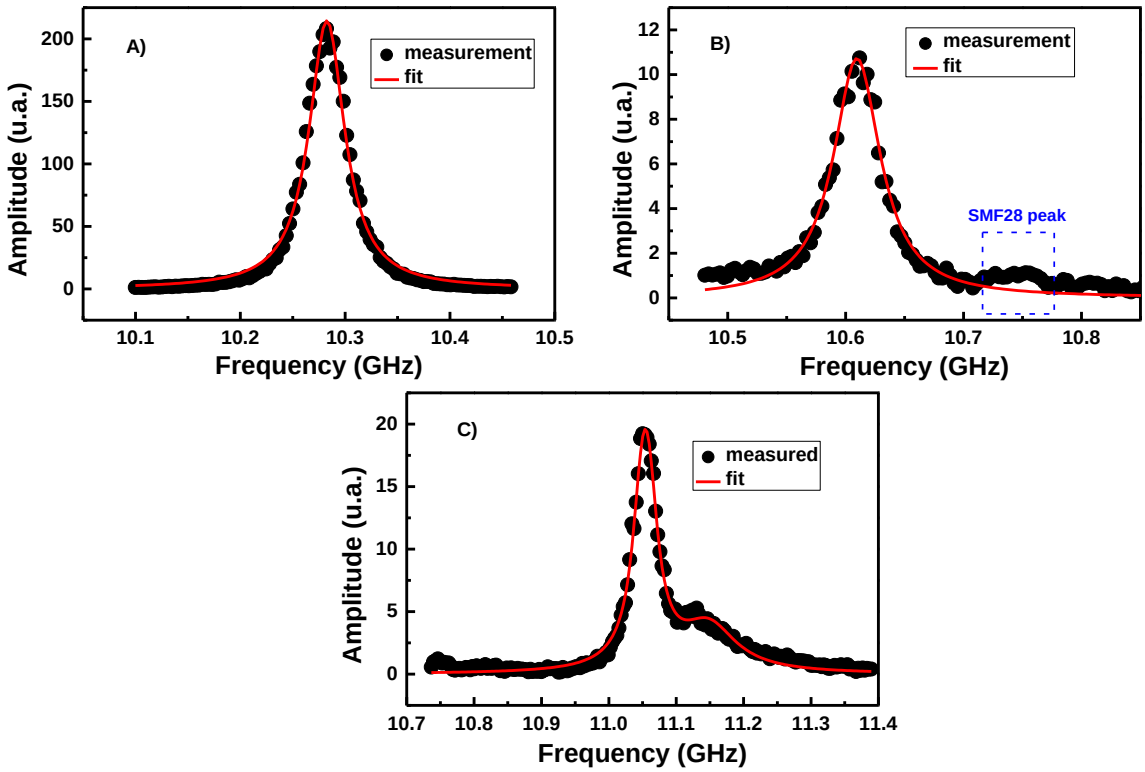

Figure 3.18: measured Brillouin frequency peaks of the SMFS_F1. In a) the first Brillouin peak, in b) the second peak, and in c) the third peak.

TABLE 3. 18: MEASURED FREQUENCIES FOR THE BRILLOUIN PEAKS OF THE SMFS_F SAMPLES

Sample	ν_1 (GHz)	ν_2 (GHz)	ν_3 (GHz)
SMFS_F1	$10.281\pm1\cdot10^{-3}$	$10.610\pm0.34\cdot10^{-3}$	$11.055\pm0.41\cdot10^{-3}$
SMFS_F2	$10.291\pm0.22\cdot10^{-3}$	$10.608\pm0.45\cdot10^{-3}$	$11.050\pm0.68\cdot10^{-3}$
SMFS_F3	$10.242\pm0.05\cdot10^{-3}$	$10.574\pm0.35\cdot10^{-3}$	$11.030\pm0.52\cdot10^{-3}$

3.4.1.2.2 Thermal coefficient

After characterizing the Brillouin spectrum, calibration procedure has been done to extract the temperature and strain coefficients for each Brillouin peak of each fiber sample. To do this iXblue has coiled, for each fiber, one sample on a quartz support applying a successive coiling tension, as represented in Figure 3.19. The choice of the quartz support is explained by its low deformation during a thermal treatment and then reduced strain parasitic impact during the

temperature coefficient measurement. Five coiling tensions have been selected: 17 g, 67 g, 117 g, 167 g, and 217 g (which correspond to 158.1 με, 623.1 με, 1088.1 με, 1553.1 με and 2018.1 με). These pipes in quartz have been placed inside the oven with type K thermocouples. Five steps of temperature have been applied on the fiber: 30 °C, 40 °C, 50 °C, 60 °, and 70 C. With this set-up we can highlight any crossing effect between the strain and the temperature on the Brillouin spectrum. Figure 3.20 illustrates the spatial variation of the first Brillouin peak frequency along the tested sample. The effects of coiling tension and temperature are clearly observable and we can easily determine the differently strained fiber parts with the BOTDA. For each zone, we have considered 101 spatial points and have calculated the temperature coefficient for each point. Figure 3.21 gives the evolution of the temperature coefficient for each tension step, with the associated error calculated by a standard deviation. The biggest variation for the C_{T1} is between the tension 2 (623.1 με) and tension 5 (2018.1 με) and corresponds to a variation of 1.8% (0.02 ± 0.005MHz/°C). Concerning the C_{T2} the biggest variation is between the tension 1 (158.1 με) and tension 3 (1088 με) and corresponds to a difference of 11.6% (0.16 ± 0.07 MHz/°C). Finally, the largest variation has been measured for temperature coefficient C_{T3} between tension 2 (623.1 με) and tension 5 (2018.1 με) and is equal to 5.3% (0.07 ± 0.04 MHz/°C). In view of these results, we can say that the temperature coefficients are not affected by the strain up to 2018.1 με. In this case we have calculated the temperature coefficient associated to each peak and to each tension for the three samples, and we have performed an average. These values of temperature coefficient are reported in TABLE 3.19. We can observe a difference of the temperature coefficient between the different samples. Indeed, the maximum measured difference for C_{T1} is 0.19 ±0.02 MHz/°C (16%) and concerns the SMFS_F2 and the SMFS_F3 samples. For C_{T2} and C_{T3} the maximum difference is 0.11 ±0.064 MHz/°C (8.3%) and 0.14 ±0.046 MHz/°C (11.1%) and concern the SMFS_F1 and SMFS_F3 for C_{T2} and SMFS_F1 and SMFS_F2 for $C_{T3,}$ respectively. So a small variation of the temperature coefficient is observed by varying the fiber drawing conditions but none tendency can be easily pointed out. Moreover, the internal stress is included in our simulation based on the IFA measurement, contrary to the simulation work of Yolande Sikali Mamdem [85] which includes the measured internal strain.

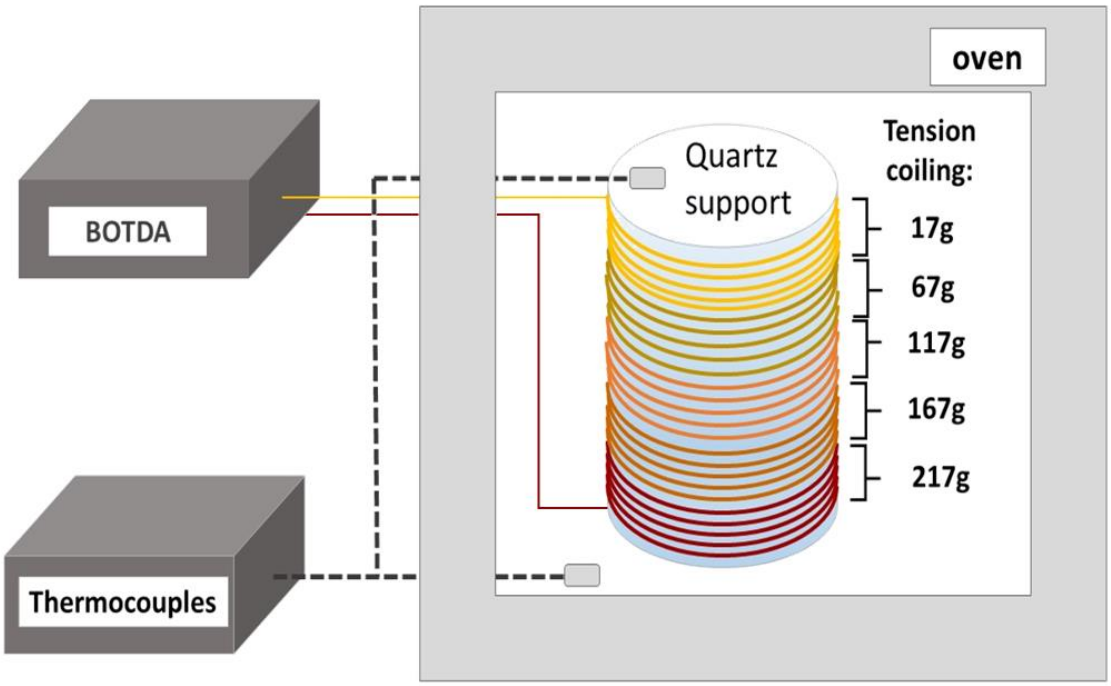

Figure 3.19: experimental set-up used to characterize the temperature and strain coefficients

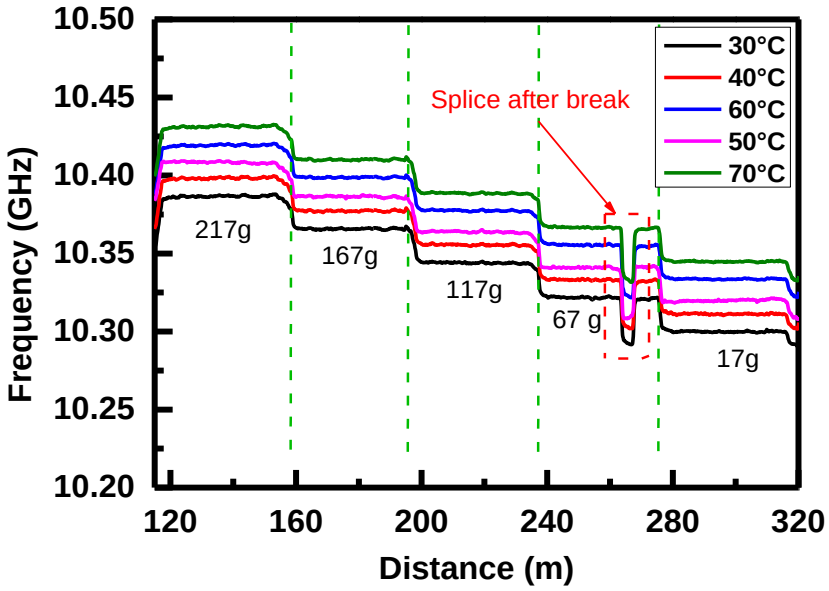

Figure 3.20: Spatial evolution of the frequency of the first Brillouin peak measured on the packaged SMFS_F1 sample at different coiling tensions and different temperatures

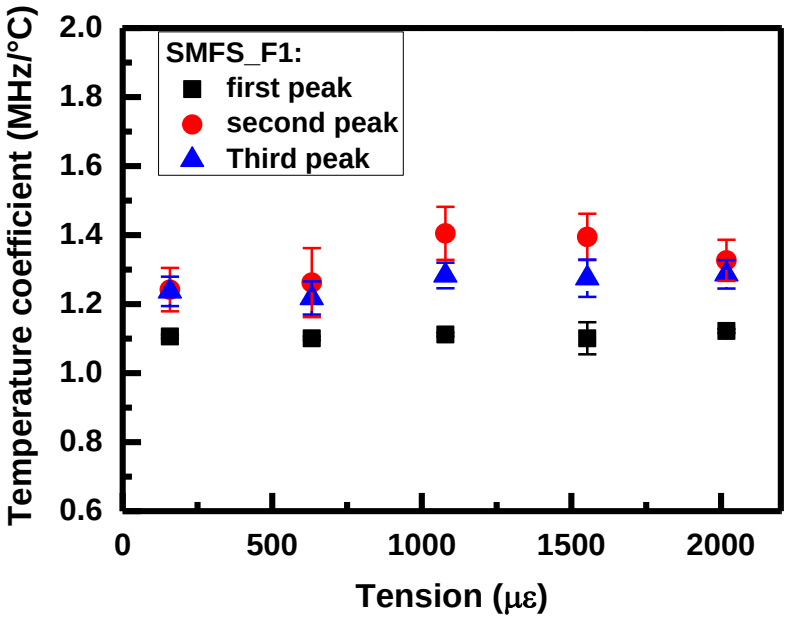

Figure 3.21: Evolution of the temperature coefficients of the three Brillouin frequency peaks at different tensions for SMFS_F1 sample.

TABLE 3.19: EXPERIMENTAL MEASUREMENTS OF THE TEMPERATURE COEFFICIENTS OF THE BRILLOUIN PEAKS OF THE SMFS_F SAMPLES

Sample	C_{T1} (MHz/°C)	C_{T2} (MHz/°C)	C_{T3} (MHz/°C)
SMFS_F1	1.11±0.014	1.32±0.060	1.26±0.045
SMFS_F2	0.99±0.02	1.31±0.034	1.12±0.046
SMFS_F3	1.18±0.012	1.21±0.064	1.26±0.043

3.4.1.2.3 Strain coefficient

For the strain coefficient we also characterized the temperature impact on their values. As for the temperature coefficient we have represented the strain coefficients measured at the different temperatures (Figure 3.22) for the three Brillouin peaks. Concerning $C_{\varepsilon 1}$ the biggest difference is 1.4% (0.0007 MHz/με) between the measurements at 40°C and 60°C. For the strain coefficient $C_{\varepsilon 2}$ and $C_{\varepsilon 3}$ the maximum difference is 2.7% (0.0014 MHz/ με) and 7% (0.0042 MHz/ με) respectively, and corresponds to 40°C and 60°C temperature steps for $C_{\varepsilon 2}$

and to 50°C and 60°C temperature step for $C_{\varepsilon 3}$. As expected, no major temperature effect on the strain coefficient values is observed. TABLE 3.20 reports the strain coefficients of the SMFS_F samples, the same procedure was used for their calculation and the ones of the temperature coefficients. We observe a strain coefficient variation between the different samples. The maximum variation of $C_{\varepsilon 1}$, $C_{\varepsilon 2}$, and $C_{\varepsilon 3}$ is 9% (0.0045 MHz/ με), 16% (0.0087 MHz/ με), and 19% (0.11 MHz/ με) respectively. These differences concern the SMFS_F2 and SMFS_F3 for $C_{\varepsilon 1}$, SMFS_F2 and SMFS_F1 for $C_{\varepsilon 2}$, and SMFS_F1 and SMFS_2 for $C_{\varepsilon 3}$. From these variations we cannot conclude on a particular effect of the drawing tension and speed on the strain coefficient.

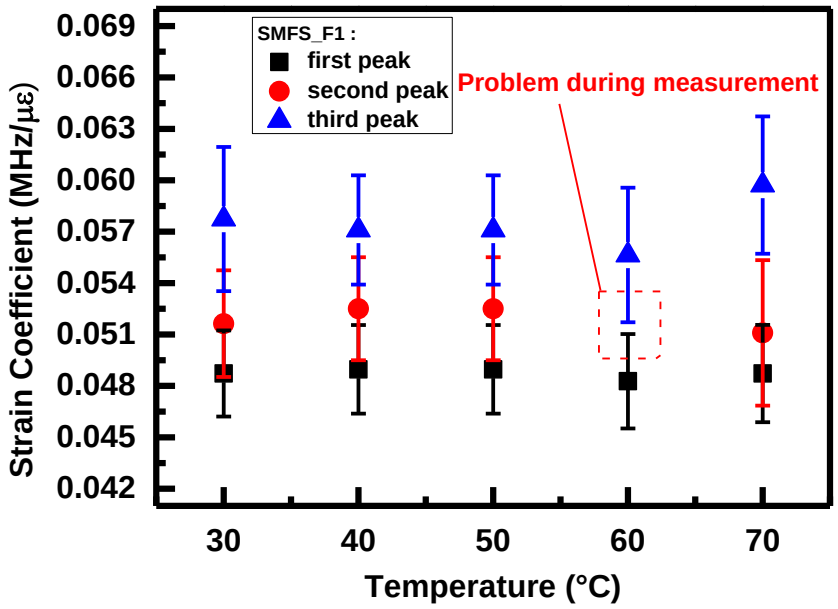

Figure 3.22: Evolution of the strain coefficient for each Brillouin frequency peak at different temperatures for SMFS_F1 sample

TABLE 3.20: EXPERIMENTAL STRAIN COEFFICIENT OF THE SMFS_F SAMPLES

Sample	$C\varepsilon_1$ (MHz/με)	$C\varepsilon_2$ (MHz/με)	$C\varepsilon_3$ (MHz/με)
SMFS_F1	0.0487±0.0027	0.0519±0.0042	0.0575±0.0042
SMFS_F2	0.0454±0.0023	0.0432±0.0079	0.0465±0.0081
SMFS_F3	0.0442±0.0038	0.0471±0.0016	0.0489±0.0012

3.4.1.3 Ge-doped fiber

3.4.1.3.1 Brillouin spectrum

We have measured the Brillouin spectra of the SMFS_Ge samples to determine the position of each frequency peak, and as for the SMFS_F sample, we have recorded each Brillouin frequency peak with a frequency step of 0.64 MHz. By using the Lorentzian fit (equation 3.1) we have determined the frequency value of each Brillouin peak. TABLE 3.21 reports these experimental values. Regarding the first Brillouin peak we obtain a maximum variation of 0.5 % (48 MHz) of its frequency, for the second and third peaks we observe that the frequency value decreases when the drawing tension and speed increase. Indeed we obtained a maximum difference of 0.6 % (69 MHz) and 0.4 % (74 MHz) for ν_2 and ν_3, respectively.

TABLE 3.21*:* MEASURED BRILLOUIN FREQUENCY FOR EACH PEAK OBSERVED IN THE SMFS_GE SAMPLES

Sample	ν_1 (GHz)	ν_2 (GHz)	ν_3 (GHz)
SMFS_Ge1	$10.277\pm0.13\cdot10^{-3}$	$10.629\pm0.90\cdot10^{-3}$	$11.096\pm0.55\cdot10^{-3}$
SMFS_Ge2	$10.276\pm0.09\cdot10^{-3}$	$10.622\pm0.24\cdot10^{-3}$	$11.087\pm0.52\cdot10^{-3}$
SMFS_Ge3	$10.229\pm0.19\cdot10^{-3}$	$10.560\pm0.15\cdot10^{-3}$	$11.022\pm0.12\cdot10^{-3}$

3.5.1.2.3 Temperature coefficients

We have determined the temperature coefficients of each sample with the procedure described in part 3.4.1.2.2, and we have investigated possible effect of strain on the temperature coefficient. We have observed the same phenomena than for the SMFS_F sample, and then we have performed an averaging of the temperature coefficients measured for each strain step. TABLE 3.22 reports these values of temperature coefficient. We obtained a variation of 3.6 % (0.04 MHz/°C) for C_{T1}, 14.8 % (0.2 MHz/°C) for C_{T2}, and 4.2 % (0.05 MHz/°C) for C_{T3}.

TABLE 3.22: EXPERIMENTALLY MEASURED TEMPERATURE COEFFICIENTS FOR THE DIFFERENT BRILLOUIN PEAKS OF THE SMFS_GE SAMPLES

Sample	C_{T1} (MHz/°C)	C_{T2} (MHz/°C)	C_{T3} (MHz/°C)
SMFS_Ge1	1.08±0.006	1.27±0.030	1.15±0.021
SMFS_Ge2	1.12±0.005	1.15±0.033	1.20±0.018
SMFS_Ge3	1.11±0.005	1.35±0.095	1.18±0.033

3.4.1.3.3 Strain coefficients

Finally, we have determined the strain coefficients (detailed in TABLE 3.23) of each of the SMFS_Ge samples. As previously, we have compared the strain coefficients to highlight the possible impact of drawing conditions. We measured variations of 12 % (0.0065 MHz/ με) for $C_{\varepsilon 1}$, 5.7 % (0.0031 MHz/με) for $C_{\varepsilon 2}$, and 13.0 % (0.0074 MHz/με) for $C_{\varepsilon 3}$. This confirms an impact of the drawing, but none tendency can be found with respect to the considered tensions and speeds.

TABLE 3.23: EXPERIMENTAL STRAIN COEFFICIENT OF THE SMFS_GE SAMPLES

Sample	$C\varepsilon_1$ (MHz/με)	$C\varepsilon_2$ (MHz/με)	$C\varepsilon_3$ (MHz/με)
SMFS_Ge1	0.0541±0.00019	0.0506±0.0012	0.0565±0.00055
SMFS_Ge2	0.0504±0.00019	0.0537±0.0008	0.0568±0.00054
SMFS_Ge3	0.0476±0.00021	0.0516±0.0012	0.0494±0.00120

3.5 Confrontation between simulation and experiments

3.5.1 Brillouin Spectrum

TABLE 3.24 and TABLE 3.*25* compare the simulation and the experimental results regarding the frequencies of each Brillouin peaks of the SMFS_Ge and SMFS_F samples, respectively. For both sample types, our simulations well predict the experimental results. Indeed, the maximum difference for the SMFS_Ge sample is 1% (peak 3 of the SMFS_Ge3)

and the maximum difference of the SMFS_F sample is 0.7% (peak 2 of the SMFS_F3). In terms of drawing effect, these results demonstrate our ability to predict the Brillouin peak frequencies regardless of the drawing tension and speed, indeed for each sample we have 1% or less of difference between experiments and simulation.

TABLE 3.24*:* COMPARISON BETWEEN CALCULATED AND MEASURED FREQUENCIES FOR EACH BRILLOUIN PEAK OF THE SMFS_GE SAMPLES

	SMFS_Ge1	SMFS_Ge2	SMFS_Ge3
$\nu_{1\_measured}$ (GHz)	$10.277 \pm 0.13 \cdot 10^{-3}$	$10.276 \pm 0.09 \cdot 10^{-3}$	$10.229 \pm 0.19 \cdot 10^{-3}$
$\nu_{1\_simulat}$ (GHz)	10.237	10.276	10.188
Difference (%)	0.4	0	0.4
$\nu_{2\_measured}$ (GHz)	$10.629 \pm 0.90 \cdot 10^{-3}$	$10.622 \pm 0.24 \cdot 10^{-3}$	$10.560 \pm 0.15 \cdot 10^{-3}$
$\nu_{2\_simulat}$ (GHz)	10.639	10.647	10.520
Difference (%)	0.1	0.2	0.4
$\nu_{3\_measured}$ (GHz)	$11.096 \pm 0.55 \cdot 10^{-3}$	$11.087 \pm 0.52 \cdot 10^{-3}$	$11.022 \pm 0.12 \cdot 10^{-3}$
$\nu_{3\_simulat}$ (GHz)	11.029	11.023	10.922
Difference (%)	0.6	0.6	1

TABLE 3.25: COMPARISON BETWEEN CALCULATED AND MEASURED FREQUENCIES FOR EACH BRILLOUIN PEAK OF THE SMFS_F SAMPLES

	SMFS_F1	SMFS_F2	SMFS_F3
$\nu_{1\_measured}$ (GHz)	$10.281 \pm 1 \cdot 10^{-3}$	$10.291 \pm 0.22 \cdot 10^{-3}$	$10.242 \pm 0.05 \cdot 10^{-3}$
$\nu_{1\_simulat}$ (GHz)	10.265	10.267	10.239
Difference (%)	0.2	0.2	0.03
$\nu_{2\_measured}$ (GHz)	$10.610 \pm 0.34 \cdot 10^{-3}$	$10.608 \pm 0.45 \cdot 10^{-3}$	$10.574 \pm 0.35 \cdot 10^{-3}$
$\nu_{2\_simulat}$ (GHz)	10.648	10.627	10.593
Difference (%)	0.4	0.2	0.2
$\nu_{3\_measured}$ (GHz)	$11.055 \pm 0.41 \cdot 10^{-3}$	$11.050 \pm 0.68 \cdot 10^{-3}$	$11.030 \pm 0.52 \cdot 10^{-3}$
$\nu_{3\_simulat}$ (GHz)	11.005	10.983	10.977
Difference (%)	0.5	0.6	0.5

3.5.2 Temperature coefficients

As for the Brillouin peak frequencies we compared the calculated and measured temperature coefficients. TABLE 3.26 and TABLE 3.*27* report the results for the SMFS_Ge and the SMFS_F sample, respectively. Regarding the SMFS_Ge fiber, we obtained around 10% of difference with two exceptions for the second temperature coefficient of the SMFS_Ge1 and SMFS_Ge3 samples for which the difference reaches ~20%. Concerning the SMFS_F sample, we obtain a mean variation around 13% with a maximum difference of 20.6 % (second temperature coefficient of the SMFS_F2 sample) and a minimum difference of 1 % (first temperature coefficient of the SMFS_F2 sample). For both types of fiber, similar results to those reported in chapter 2 have been obtained.

TABLE 3.26: COMPARISON BETWEEN SIMULATED AND MEASURED TEMPERATURE COEFFICIENTS OF THE BRILLOUIN PEAKS OF THE SMFS_GE SAMPLES

	SMFS_Ge1	SMFS_Ge2	SMFS_Ge3
$C_{T1\_measured}$ (GHz)	1.08±0.006	1.12±0.005	1.11±0.005
$C_{T1\_simulat}$ (GHz)	1.0	1.00	1.0
Difference (%)	7.4	10.7	9.9
$C_{T2\_measured}$ (GHz)	1.27±0.03	1.15±0.033	1.35±0.095
$C_{T2\_simulat}$ (GHz)	1.04	1.04	1.03
Difference (%)	18.1	9.60	23.7
$C_{T3\_measured}$ (GHz)	1.15±0.021	1.20±0.018	1.18±0.033
$C_{T3\_simulat}$ (GHz)	1.08	1.08	1.07
Difference (%)	6.1	10	9.3

TABLE 3.27: COMPARISON BETWEEN SIMULATED AND MEASURED TEMPERATURE COEFFICIENTS OF THE BRILLOUIN PEAKS OF THE SMFS_F SAMPLES

	SMFS_F1	SMFS_F2	SMFS_F3
$C_{T1\_measured}$ (GHz)	1.11±0.014	0.99±0.02	1.18±0.012
$C_{T1\_simulat}$ (GHz)	1.0	1.0	1.0
Difference (%)	9.9	1	15.3
$C_{T2\_measured}$ (GHz)	1.32±0.06	1.31±0.034	1.21±0.064
$C_{T2\_simulat}$ (GHz)	1.05	1.04	1.03
Difference (%)	20.5	20.6	14.9
$C_{T3\_measured}$ (GHz)	1.26±0.045	1.12±0.046	1.26±0.0431
$C_{T3\_simulat}$ (GHz)	1.07	1.07	1.07
Difference (%)	15.1	4.5	15.1

3.5.3 Strain coefficients

Finally we compare in TABLE 3.28 and TABLE 3.*29* the experiments and the simulations for the strain coefficients of the SMFS_Ge and the SMFS_F samples, respectively. For the SMFS_Ge samples we obtain a mean difference of 4% with a maximum difference of 10.5% for the first strain coefficient of SMFS_Ge1 and a minimum difference of 0.8% for the first strain coefficient of the SMFS_Ge3. The predictions of strain coefficients are then very close to the experimental values. Regarding the SMFS_F samples, we obtain a mean difference of 9% with the maximum error 18.8% (2^{nd} coefficient of SMFS_F2) and a minimum difference of 0.8% (1^{st} coefficient of SMFS_F1). As a reminder, to calibrate the strain coefficient we have coiled the sample at different tensions in grams on cylinder in fused silica. To convert our strain coefficient from MHz/g into MHz/με we have applied different weights on the fiber and convert this tension in strain with a tensile gauge. Typically, after measurement, to convert the strain coefficient we divide the strain coefficient of the SMFS_F sample by 9.2 and by 8.6 for the SMFS_Ge sample. Despite these small differences between the simulation and the experiment, our predictions are considered as in good agreement with the experimental results and for sure are efficient to design optimized optical fibers for sensing applications.

TABLE 3.28: COMPARISON BETWEEN SIMULATED AND MEASURED STRAIN COEFFICIENTS OF THE BRILLOUIN PEAKS OF THE SMFS_GE SAMPLES

	SMFS_Ge1	SMFS_Ge2	SMFS_Ge3
$C_{\varepsilon 1\_measured}$ (GHz)	0.0541±0.0002	0.0504±0.0002	0.0476±0.0002
$C_{\varepsilon 1\_simulat}$ (GHz)	0.0484	0.049	0.048
Difference (%)	10.5	2.8	0.8
$C_{\varepsilon 2\_measured}$ (GHz)	0.0506±0.0012	0.0537±0.0008	0.0516±0.0001
$C_{\varepsilon 2\_simulat}$ (GHz)	0.0513	0.0515	0.05
Difference (%)	1.4	4.1	3.1
$C_{\varepsilon 3\_measured}$ (GHz)	0.0565±0.0006	0.0568±0.0005	0.0494±0.0001
$C_{\varepsilon 3\_simulat}$ (GHz)	0.0551	0.0547	0.0531
Difference (%)	2.5	3.7	7.5

TABLE 3.29: COMPARISON BETWEEN SIMULATED AND MEASURED STRAIN COEFFICIENTS OF THE BRILLOUIN PEAKS OF THE SMFS_F SAMPLES

	SMFS_F1	SMFS_F2	SMFS_F3
$C_{\varepsilon 1\_measured}$ (GHz)	0.0487±0.0003	0.0454±0.0002	0.0442±0.0004
$C_{\varepsilon 1\_simulat}$ (GHz)	0.0483	0.049	0.0486
Difference (%)	0.8	7.9	10
$C_{\varepsilon 2\_measured}$ (GHz)	0.0519±0.0006	0.0432±0.0007	0.0471±0.0002
$C_{\varepsilon 2\_simulat}$ (GHz)	0.0513	0.0513	0.051
Difference (%)	1.2	18.8	8.3
$C_{\varepsilon 3\_measured}$ (GHz)	0.0575±0.0004	0.0465±0.0007	0.0489±0.0001
$C_{\varepsilon 3\_simulat}$ (GHz)	0.055	0.0546	0.0542
Difference (%)	4.3	17.4	10.8

3.6 Discrimination between the strain and temperature applied to the fibers

3.6.1 Metrological approach

The discrimination problem has been already studied in the literature [132] for optical fibers presenting two Brillouin frequency peaks such as the LEAF fiber from Corning [133]. In their article, the authors proposed to solve the equations 3.2 and 3.3 to discriminate between the strain and the temperature applied on the single-mode optical fiber [133]:

$$\delta' T = \frac{|C_{\epsilon 2}|\delta\nu_1 + |C_{\epsilon 1}|\delta\nu_2}{|C_{\epsilon 2}C_{T1} - C_{\epsilon 1}C_{T2}|} \quad (3.2)$$

$$\delta' \epsilon = \frac{|C_{T2}|\delta\nu_1 + |C_{\epsilon 1}|\delta\nu_2}{|C_{\epsilon 2}C_{T1} - C_{\epsilon 1}C_{T2}|} \quad (3.3)$$

where $\delta\nu$ is the error done when measuring the Brillouin peak frequency.

Generally this error is related to the interrogator architecture scheme and performances. In our case the interrogator from Oz Optics gives only the strain or temperature measurements [131], but not the error associated on the Brillouin peak frequency measurement. To solve these equations, it has been decided to use a least squares method to determine the error associated to each measure of Brillouin frequency. The equation used to determine the temperature or strain values is:

$$\nu_m - C_{\epsilon_m} \times \epsilon = C_{T_m} \times T \quad (3.4)$$

In our case we have considered $C_{\epsilon_m} \times \epsilon$ as a constant, this is supported by the fact that no crossing effect between the strain and the temperature has been measured. So the equation 3.4 can be written as:

$$P = XR \quad (3.5)$$

where X and P are defined as follow :

$$\begin{cases} P = \left[\nu_m - C_{\epsilon_m} \times \epsilon\right] \\ X = [T\ 0] \end{cases} \quad (3.6)$$

The coefficient of the linear model is given by:

$$\begin{cases} R = (X^T X)^{-1} X^T P \\ R = [C_T] \end{cases} \quad (3.7)$$

where X^T is the transpose of matrix X. The response A and the residue e are calculated as:

$$A = XR \quad (3.8)$$

$$e = P - A \quad (3.9)$$

and the variance is given by:

$$\sigma^2 = \frac{1}{N-2} \sum_{i=1}^{N} e_i^2 \quad (3.10)$$

where N is the number of measurements. The confidence interval can be calculated as:

$$\Sigma^2 = \sigma^2 \left[1 + X^* (X^T X)^{-1} X^{*T}\right] \quad (3.11)$$

where X^* is the matrix at the temperature at which we calculated the confidence interval. So finally the boundaries for the confidence interval for one measurement are given by:

$$\nu_m - C_{\epsilon_m} \times \epsilon = C_{T_m} \times T \pm t_\alpha \Sigma \quad (3.12)$$

where t_α is the Student's coefficient :1.96 in our case to obtain a boundary confidence of 95 % [134]. The boundary confidence interval for N measurements is given by equation 3.14:

$$\Sigma'^2 = \sigma^2 \left[\frac{1}{N} + X^* (X^T X)^{-1} X^{*T}\right] \quad (3.13)$$

$$\nu_m - C_{\epsilon_m} \times \epsilon = C_{T_m} \times T \pm t_\alpha \Sigma' \quad (3.14)$$

Figure 3.23 gives each point measured at the different temperatures and for each differently strained region of the SMFS_F1 sample. In this figure, the red line corresponds to a linear fit while the blue line corresponds to the 95% boundary confidence interval for N measurements.

Treating all fibers and all their Brillouin peaks, we also have considered 101 spatial positions, and 5 steps of strain. In this case N= 505. By dividing the boundary confidence interval by two, we have obtained the frequency measurement error for each Brillouin frequency peak. The results are detailed in TABLE 3.30. We can observe a frequency error ($\delta\nu$) superior to 1 MHz in all case except for the $\delta\nu_1$ of the SMFS_Ge1. This result can be explained by the distributed capacities. Indeed, the applied strain along the fiber is not perfectly homogenous, and then, the Brillouin frequency measurement along the fiber could vary of several MHz.

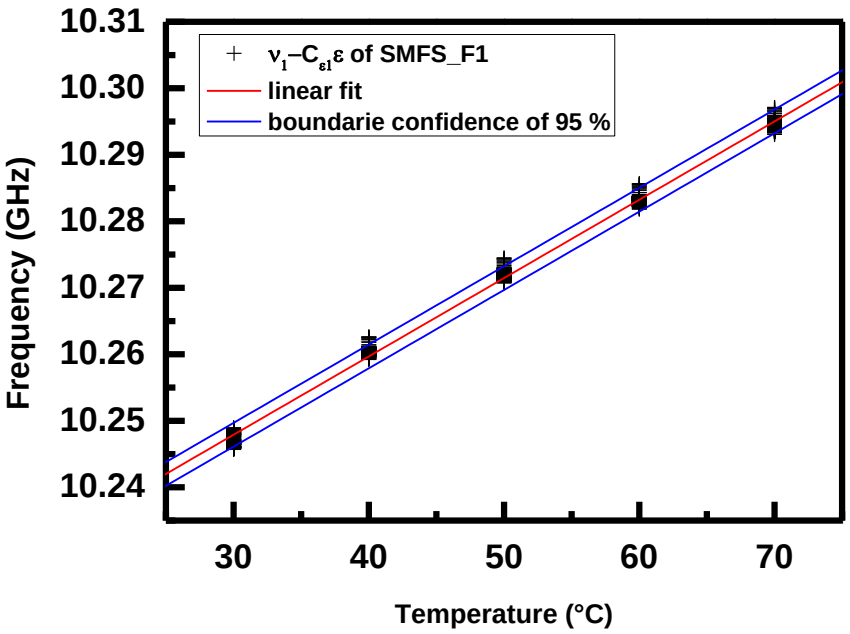

Figure 3.23: Metrological analysis of the first Brillouin frequency peak minus strain effect of the SMF_F sample. The red line corresponds to the linear fit and the blue line to the boundary confidence of 95%

TABLE 3.30*:* ASSOCIATED ERROR TO THE FREQUENCY MEASUREMENT CALCULATED WITH THE LAST SQUARE ROOT METHOD

Error frequency	SMFS_F1 (MHz)	SMFS_F2 (MHz)	SMFS_F3 (MHz)	SMFS_Ge1 (MHz)	SMFS_Ge2 (MHz)	SMFS_Ge3 (MHz)
$\delta\nu_1$	2.1	2.4	1.8	0.7	1.6	1.5
$\delta\nu_2$	4.2	3.1	3.7	2.4	2.4	2.7
$\delta\nu_3$	3.2	3.7	3.1	2.6	2.4	2.2

3.6.2 Discrimination strain temperature

By applying the equations (3.2) and (3.3) we have calculated the discrimination performances that can be achieved with the various fibers combined to our BOTDA. For the results shown in Figure 3.24 we have considered the best system between ν_1/ν_2, ν_2/ν_3, and ν_1/ν_3 to achieve the best discrimination. Obviously, we obtained reduced discrimination capacity, this being explained by the large error, previously discussed, on the frequency measurement. The best candidate is the SMFS_Ge1 with an error of 248 με/ 12 °C.

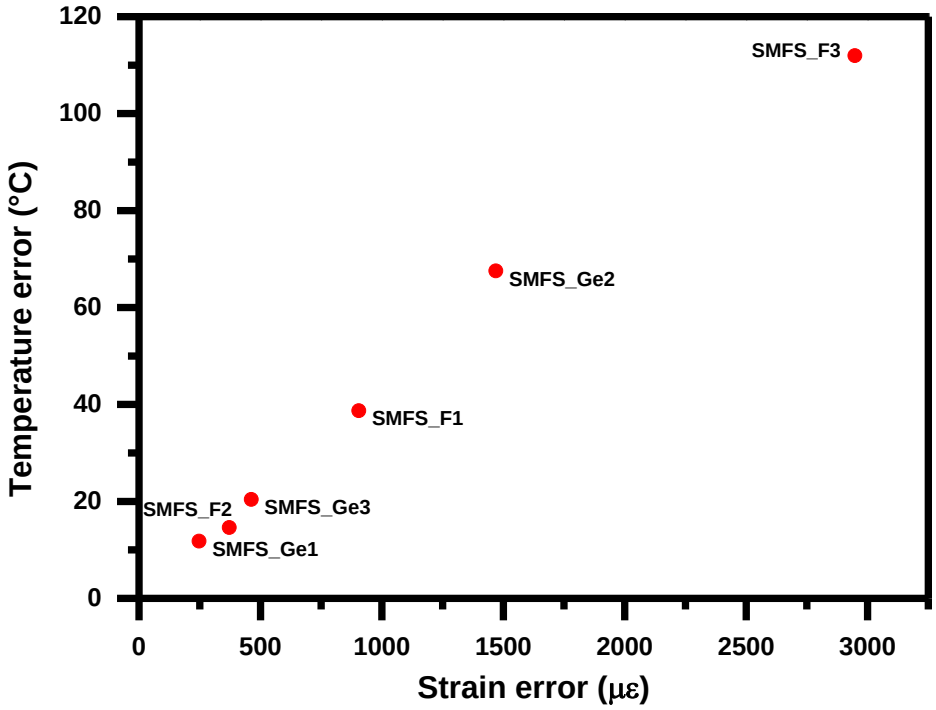

Figure 3.24: Discrimination capacities of each sample with the associated error calculated with the metrological approach

3.6.3 Discrimination with the method of patent

The results presented in the previous part are not satisfying, however during this PhD work period, other peoples have been working on the same research subject. The first study was about simulations [132] while a second one concerns both theoretical and experimental results [135]. The authors propose a discrimination method basing on the measurements of two Brillouin frequency peaks in the same fiber with a BOTDA interrogator. We propose to

compare our results with the literature ones including the older results of the LEAF fiber [124], [136], [137]. To compare the potential of discrimination of our fiber with the literature we have to consider the same error induced by the interrogator on the frequency measurement. So, we used the equation described in the patent [118] to compare the discrimination capacities:

$$\delta\epsilon = \frac{\sqrt{C_{T1}^2 + C_{T2}^2}}{|C_{T1}C_{\epsilon 2} - C_{T2}C_{\epsilon 1}|} \quad (3.15)$$

$$\delta T = \frac{\sqrt{C_{\epsilon 1}^2 + C_{\epsilon 2}^2}}{|C_{T1}C_{\epsilon 2} - C_{T2}C_{\epsilon 1}|} \quad (3.16)$$

In this case we obtain a $\delta\epsilon$ and a δT in με/MHz and °C/MHz respectively. It is then possible to compare different fibers and interrogators with different measurement errors. As previously, we have considered the best combination between ν_1/ν_2, ν_2/ν_3, and ν_1/ν_3. Figure 3.25 and TABLE 3.31 summarize the resulting discriminations capacities of our fibers and the ones of literature. Two of our fibers present better discrimination performances than the SSMF-B [135] and the LEAF fiber. It should be pointed out that our fiber has been tested with a BOTDR interrogator contrary to the SSMF-B, FMF, and the SSMF-A. The Brillouin spectrum of the SMFS_F1 measured with a BOTDR is represented in Figure 3.26. We can see clearly the three Brillouin frequency peaks. So we can conclude that two of our fibers have the best discrimination actually reported. Furthermore all the fibers produced by iXblue Photonics can be adapted on each type of interrogator (BOTDA, BOTDR) thanks to their single mode characteristics, low attenuation. This BOTDR is from Viavi-solutions and propose another solution to discriminate the strain and the temperature. It will be detailed in the part 3.7 in the framework of a research about fiber instrumentation in the nuclear domain.

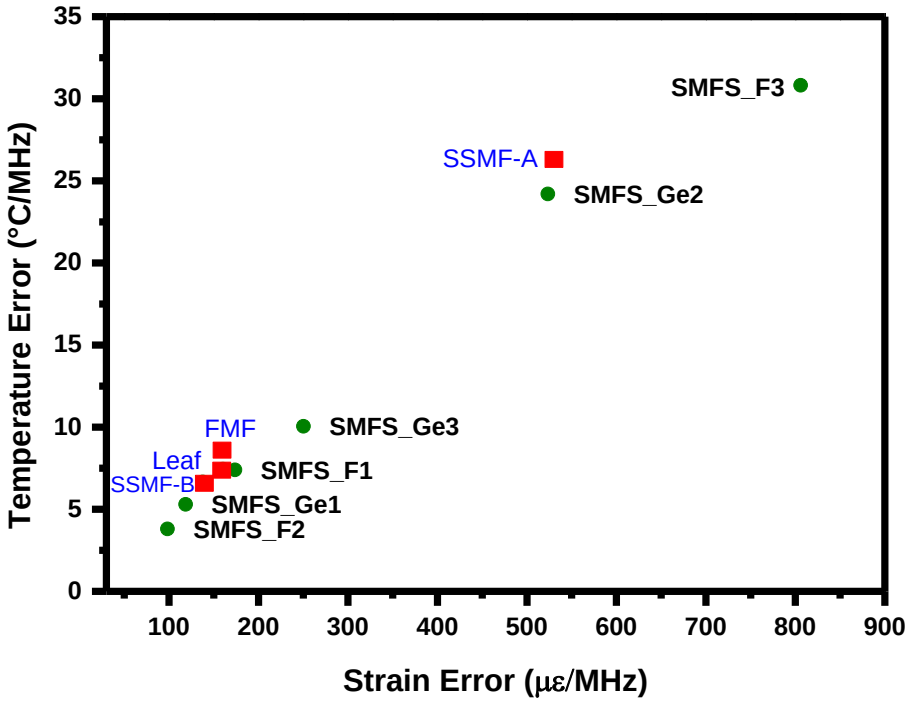

Figure 3.25: Discrimination capacities between the strain and the temperature with the patent method. The green characters correspond to the samples of this thesis, and the red characters correspond to the literature data [124], [135]

TABLE 3.31: DISCRIMINATION PERFORMANCES OF THE VARIOUS FIBERS CALCULATED WITH THE PATENT METHOD

Sample		Temperature error (°C/MHz)	Strain error (με/MHz)
PhD Thesis	SMFS_F1	7.4	173.7
	SMFS_F2	3.8	98.3
	SMFS_F3	30.82	806
	SMFS_Ge1	5.3	118.6
	SMFS_Ge2	24.2	523.42
	SMFS_Ge3	10.05	250.2
Literature [124], [135]	SSMF-A	26.3	531
	SSMF-B	6.66	137.79
	FMF	8.57	158.76
	LEAF	7.44	160.4

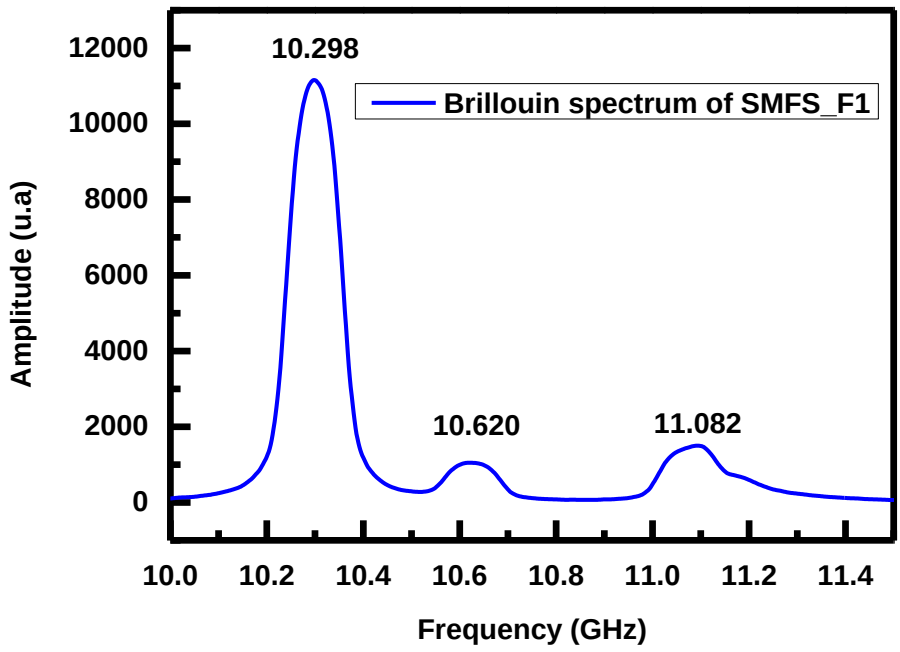

Figure 3.26: Brillouin spectrum of the SMFS_F1 sample measured with the BOTDR from Viavi-solutions

3.6.4 Discrimination with 3 peaks

Finally, we have tried to use the contribution of the three peaks to discriminate between the temperature and the strain contribution along the fiber. For that, we have adapted the equation (3.15) and (3.16) to create a system of three equations:

$$\begin{bmatrix} \nu_1 \\ \nu_2 \\ \nu_3 \end{bmatrix} = \begin{bmatrix} C_{T1} & C_{\epsilon 1} \\ C_{T2} & C_{\epsilon 2} \\ C_{T3} & C_{\epsilon 3} \end{bmatrix} \begin{bmatrix} T \\ \epsilon \end{bmatrix} \qquad (3.17)$$

if we define our matrix C as:

$$C = \begin{bmatrix} C_{T1} & C_{\epsilon 1} \\ C_{T2} & C_{\epsilon 2} \\ C_{T3} & C_{\epsilon 3} \end{bmatrix} \qquad (3.18)$$

We can solve our system through the equation (3.19):

$$\begin{bmatrix}\delta T\\ \delta\epsilon\end{bmatrix} = (C^T C)^{-1} C^T \begin{bmatrix}\delta_{\nu 1}\\ \delta_{\nu 2}\\ \delta_{\nu 3}\end{bmatrix} \quad (3.19)$$

where $(C^T C)^{-1} C^T$ is called the M matrix (2x3), and then we define the temperature and strain precision as:

$$\delta T = \sqrt{M_{11}^2 + M_{12}^2 + M_{13}^2} \quad (3.20)$$

$$\delta\epsilon = \sqrt{M_{21}^2 + M_{22}^2 + M_{23}^2} \quad (3.21)$$

From these equations we have represented the capacities of discrimination in Figure 3.27 and detailed in TABLE 3.32. With this method we increase a bit the performances of our sensors, but the performances are still under the ones of the SSMF-B sample except for the SMFS_Ge1 and SMFS_F2 that present better performances.

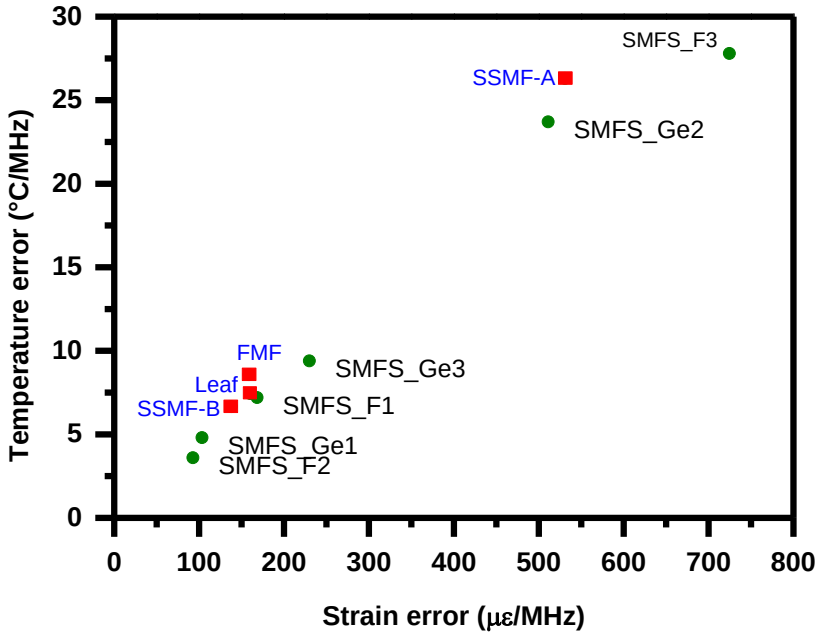

Figure 3.27: Discrimination capacities between strain and temperature by using the three Brillouin frequency peaks with the patent method

TABLE 3.32: DETAILS VALUES OF THE DISCRIMINATION CAPACITIES BY USING THE THREE BRILLOUIN FREQUENCY PEAKS WITH THE PATENT METHOD

Sample		Temperature error (°C/MHz)	Strain error (με/MHz)
Thesis	SMFS_F1	7.2	168.3
	SMFS_F2	3.6	92.7
	SMFS_F3	27.8	724.6
	SMFS_Ge1	4.8	103.5
	SMFS_Ge2	23.7	511.1
	SMFS_Ge3	9.4	229.8
Literature [124], [135]	SSMF-A	26.3	531
	SSMF-B	6.66	137.79
	FMF	8.57	158.76
	LEAF	7.44	160.4

3.6.5 Partial conclusion

Starting on two fiber structures designed with our simulation model, optical fibers have been manufactured by iXblue Photonics. The objective was to evaluate the quality of our prediction of the Brillouin response of low loss optical fibers presenting multiple Brillouin peak and then able to discriminate the strain and the temperature. Different fiber samples have been produced starting from the same preform and varying the drawing conditions. These samples have been fully characterized, they present low loss levels in the IR with attenuation around 1 dB/km for each sample at 1550 nm. In a second time, we have characterized our samples in terms of Brillouin signature: frequency peak, temperature and strain coefficients. The experimental results have been compared to the predictions, showing a very good agreement b for the Brillouin frequency peak and the strain coefficients. Concerning the

temperature coefficients, the prediction remains good but may be improved by performing further research on the Young modulus and its dependence on the nature of the fiber coating.

The built optical fibers have different temperature and strain coefficients and then exhibit different performances in terms of discrimination. We compare different metrological approaches to calculate the capacities of our sensor and compare our results with those from other researchers that published articles during the PhD thesis work [118]. We have seen that our samples, SMFS_Ge1 and SMFS_F2 present better capacities than all other fibers discussed in the literature. To increase the performances in terms of discrimination we have adapted the method described in [118] to exploit the three Brillouin peaks of our fibers. In this case we increase, but only slightly, the performances of the sensor. Finally we have tested our sample with a BOTDR allowing to confirm that the developed fibers can be used with both BOTDR and BOTDA interrogators.

This interrogator from Viavi Solutions has been developed to allow discriminating the strain and the temperature changes along a single fiber by combining a BOTDR and a Rayleigh backscattering measurements. In the following section, we evaluate this sensor when the fiber is exposed to a harsh environment associated with radiations (*X-rays and γ-rays*).

3.7 Landau-Placzek Ratio: LPR

In order to solve the problem of discrimination, we have also studied another strategy. In the framework of a collaboration with Viavi-Solutions we have investigated the discrimination capacity of their new sensor [138] for the temperature and strain measurement in radiation environments. Viavi-Solution is an international company specialized in the manufacturing of fiber interrogators such as OTDR, DTS based on the Raman scattering, and BOTDR [138]. This collaboration allowed evaluating a different approach for the discrimination, working at the interrogator level. Their solution relies on an interrogator measuring both the Brillouin and the Rayleigh backscattered light[3]. This technology presents a huge interest for various harsh environments, such as the nuclear waste repositories [6], high energy physics [5], or fusion-related facilities [139] due to the distributed capacities of optical fiber sensor. The Distributed Optical Fiber Sensors (DOFS) based on Rayleigh scattering under radiation have been studied in [21–23], DOFS based on Raman scattering under

[3] These work has been presented at the 2018 RADECS conference in Sweden (S) [69]

radiation have been studied in [142], [143], and DOFS based on Brillouin scattering under radiation have been studied in [144], [145]. To discriminate the temperature and the strain effect, the solution is to combine two of these three scattering phenomena, because the Rayleigh and the Brillouin scattering are sensitive to the temperature and the strain, whereas the Raman scattering is sensitive only to the temperature. The main drawback in radiation environment is the Radiation Induced Attenuation (RIA)[146]. RIA will limit the sensing length of the DOFS. To solve this problem we have used the Distributed Temperature Strain Sensor (DTSS) interrogator from Viavi-solutions and a radiation-tolerant optical fiber from iXblue in order to reduce the RIA.

3.7.1 Distributed Temperature Strain Sensor (DTSS)

The DTSS is based on the measurement of the Rayleigh and Brillouin components of the backscattered signal around 1500 nm. The instrument is an OTDR for the attenuation characterization, and measure the Brillouin Frequency Shift to have access to the strain component assuming a constant temperature, or to obtain the information on the temperature assuming a constant strain. We can resume this interrogator such as a Brillouin-OTDR. By performing the normalization of the Brillouin power with the Rayleigh power, we can perform a measurement of the strain and the temperature independently with a unique optical fiber. Indeed, this technique has been studied first in [147] for the temperature measurement and in [148] for the strain measurement. It has been shown that the Landau-Placzek ratio (LPR), which corresponds to the normalization of the Brillouin power by the Rayleigh power, is sensitive to the strain and the temperature. Moreover, the Brillouin scattering is sensitive to the strain and the temperature, so by coupling these technologies, we obtain the needed system of equations for the discrimination:

$$\begin{bmatrix} \Delta\nu_B \\ \Delta P \end{bmatrix} = \begin{bmatrix} C_\nu^\epsilon & C_\nu^T \\ C_P^\epsilon & C_P^T \end{bmatrix} \begin{bmatrix} \Delta\epsilon \\ \Delta T \end{bmatrix} \qquad (3.22)$$

where $\nu_B$is the Brillouin Frequency Shift (BFS) and P is the normalized Brillouin power, C_ν^ϵ and C_ν^T are the temperature and the strain coefficients of the BFS respectively. C_P^ϵ and C_P^T are the temperature and strain coefficients of the Brillouin power with typical values of C_P^T=0.33 %/°C and C_P^ε= -0.0013 %/με for commercial germanosilicate optical fibers [147], [148], $\Delta\epsilon$ and ΔT are respectively the variations of strain and temperature. With this interrogator is it

possible to have a one meter spatial resolution over a distance of 10 km. As explained previously, we have tested this solution in harsh environment. Radiation induces an excess of optical losses (RIA) which increases the losses of the fiber, and thus could affect the LPR. The Rayleigh and the Brillouin scattering have a negligible difference of wavelength of 0.03 nm. Then the attenuation will be the same for the both scattering process, so the LPR will not be affected by the radiation, but the sensing length will decrease while the losses increases. Concerning the frequency Brillouin measurement, it was shown that the BFS will be affected by radiation. In [144], [145], different compositions of fiber, such has germanium (SMF28) or fluorine doped fibers, have been tested showing that the BFS of fluorine doped fiber changes of 2 MHz up to 10 MGy contrary to the germanosilicate fiber, which has a variation of BFS of 6 MHz. Moreover, the RIA is less important in fluorine-doped fiber than the germanium-doped fiber, so we will keep a good sensing length. By choosing the appropriate fluorine-doped fiber, is it possible to minimize the radiation effects and perform temperature and strain measurement along a single fiber in harsh environment. Finally, to obtain an absolute measurement of temperature and strain, the DTSS uses a reference with a thermally isolated fiber coupling with a thermocouple.

3.7.2 Post Mortem Study

The first experience is a post mortem study where the measurements are in-lab after the irradiation stops. With this test, we could evaluate the functionality of the interrogator in harsh environment and that the possible degradation levels of its performances.

3.7.2.1 Experimental set up

3.7.2.1.1 Optical fiber

We have chosen two radiation-hardened optical fibers from iXblue. Both are doped with fluorine to reduce the RIA effect. These fibers have very close characteristics (see TABLE 3.33), the unique difference being their respective coatings: polyimide for SMFV_1 and acrylate for SMFV_2. Moreover the radiation responses of these fibers have already been reported in literature [149].

TABLE 3.33: CHARACTERISTICS OF THE FIBERS

Sample	Dopant in core	Core diameter (µm)	Dopant in cladding	Coating	Numerical Aperture
SMFV_1	Pure Silica	7.0	Fluorine	Polyimide	0.14
SMFV_2	Pure Silica	7.0	Fluorine	Acrylate	0.14

3.7.2.1.2 Irradiation Facilities

For the post-mortem study, we have irradiated our sample with *γ-rays* at the IRMA ^{60}Co source from IRSN at Saclay in France up to 1.5 MGy(SiO_2) at room temperature with a dose rate of 3 kGy/h. Another sample of the SMFV_2 has been irradiated under the same conditions at 0.75 MGy. For our tests, we have spliced together 100 m of pristine (non irradiated) to 100 m of irradiated fiber for the SMFV_1. We do the same for the SMFV_2 sample, but have added 100 m of SMFV_2 sample (0.75 MGy) between the pristine and the 1.5 MGy irradiated sample of this fiber.

The aim of the first experiment is to highlight the possible irradiation effect on the Rayleigh and Brillouin scatterings. To this aim, we have placed in the oven our pristine and irradiated samples and monitored the Rayleigh scattering and the BFS at 25 °C, 50 °C, 0 °C, and 25 °C again.

The second test of the post-mortem study is described in Figure 3.28. We have placed in the oven only the irradiated sample: 1.5 MGy for the SMFV_1, 0.75 MGy, and 1.5 MGy for the SMFV_2. For both kinds of fibers, we have kept the pristine samples, as a reference, outside the oven. For that, we have connected a thermocouple and the pristine samples to the DTSS. Being thermally isolated, they provided an absolute measurement. We have measured the temperature and the strain of the irradiated sample at 25°C, 50°C, 0°C, and once again at 25°C. The objective of this second test was to discriminate the temperature and the strain using the interrogator probing hugely irradiated fiber samples.

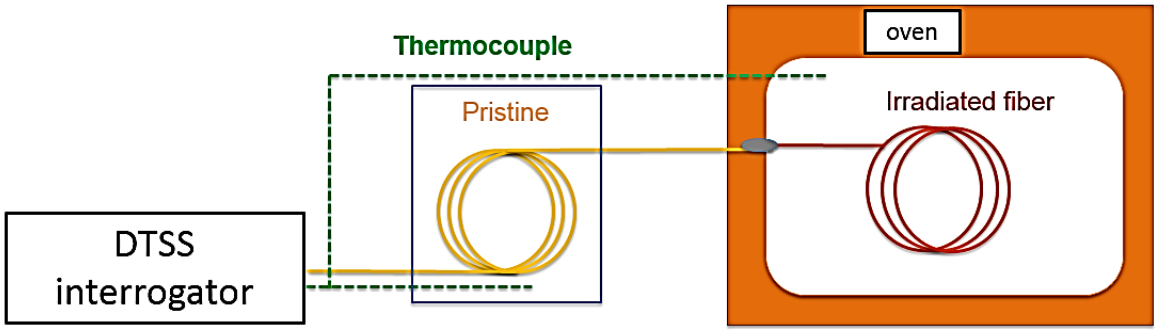

Figure 3.28: Experimental setup used for the post-mortem study

3.7.2.2 Results

3.7.2.2.1 Radiation Induced Attenuation (RIA)

The linear attenuations of the samples have been measured using the OTDR function of the DTSS. The total attenuation (intrinsic attenuation + RIA) at 1550 nm of both samples are given in Figure 3.29. The data on the pristine sample gives the intrinsic attenuation: 0.25 dB/km for the SMFV_1 and 0.35 dB/km for the SMFV_2. Concerning the SMFV_1 we measured attenuation around ~20 dB/km for the 1.5 MGy irradiated sample. Regarding the SMFV_2, the RIA associated to the 0.75 MGy irradiated sample is of ~20 dB/km and ~27 dB/km for the 1.5 MGy irradiated sample. These results agree with the RIA levels reported in [149].

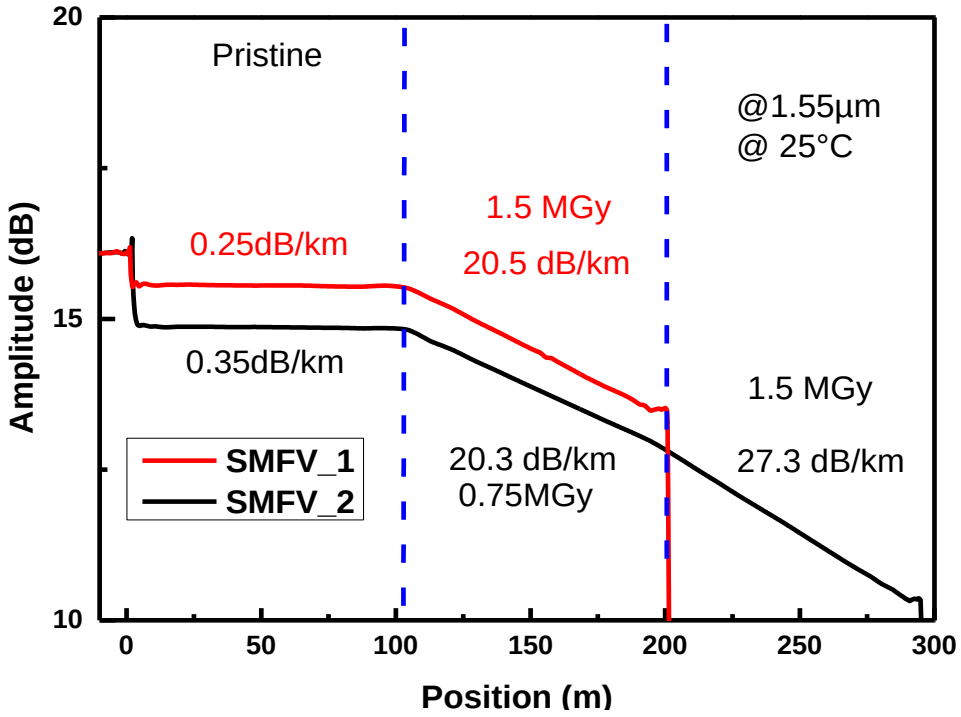

Figure 3.29: OTDR traces of SMFV_1 and SMFV_2 fiber sensing lines. Dashed lines illustrate the splicing zones of the different samples. The attenuation levels written in red correspond to the SMFV_1, and the black labels for SMFV_2.

3.7.2.2.2 Brillouin response

We have represented the Brillouin signatures along both fiber samples in Figure 3.30, in a) the Brillouin response of the SMFV_1 and in b) the Brillouin response of the SMFV_2. In the same figure are given the average values of the Brillouin frequencies of all sample at 0°C, 25°C, and 50°C. From this set of data, the thermal coefficient of each sample has been extracted. As shown in this figure, the Brillouin frequency seems unchanged by radiation for the two fibers, as shown by the comparison between the pristine and the irradiated samples. TABLE 3.34 review the Brillouin frequency values, highlighting no change. For the SMFV_1, the mean values of the Brillouin frequency at 25 °C for the pristine and the irradiated samples are of 11.0653 GHz (± 0.3 MHz), the error corresponds to the standard deviation (SD). Concerning the SMFV_2, the mean Brillouin frequency is 11.0845 GHz (± 0.3 MHz) for the pristine sample and increases to 11.0854 GHz (± 0.3 MHz) at 1.5 MGy. Finally, for both samples, the temperature coefficient seems unaffected by radiations. For the SMFV_1 the temperature coefficient is unchanged between the pristine and the irradiated samples, the largest difference (<5%) are observed for the SMFV_2 fiber between the pristine and the

0.75 MGy samples. We can conclude that the *γ-rays* do not strongly affect the Brillouin response of these radiation hardened optical fibers.

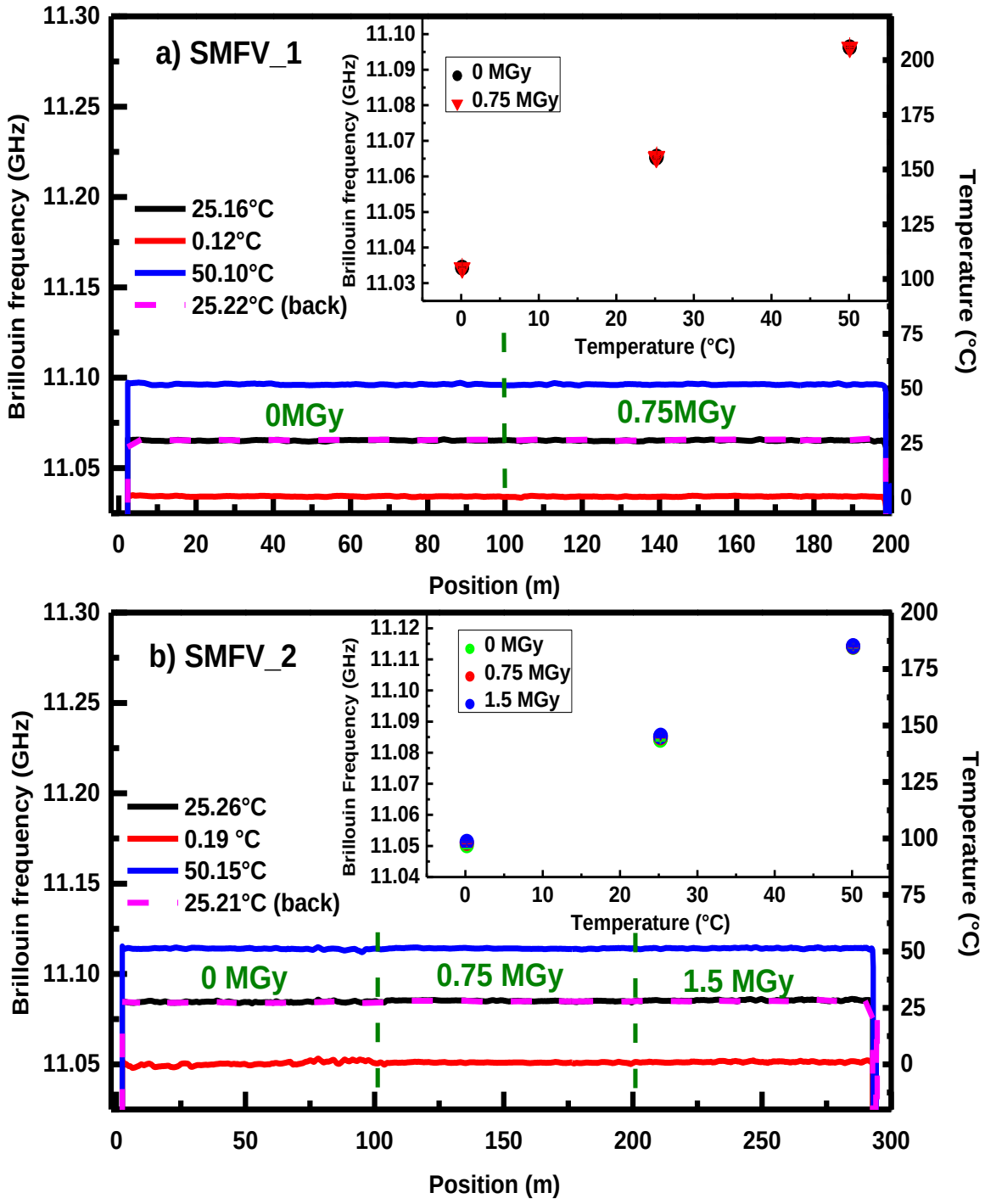

Figure 3.30: Brillouin frequency shift of pristine and irradiated samples for different test temperatures. In a) the response of SMFV_1 fiber and in b) of the SMFV_2 fiber.

TABLE 3.34: BRILLOUIN RESPONSE OF TESTED FIBER SAMPLES

Sample	Dose (MGy)	Mean BFS (GHz)	SD (10^{-4} GHz)	C_ν^T (MHz/°C)
SMFV_1	0	11.0653	±3	1.24
	1.5	11.0653	±2	1.24
SMFV_2	0	11.0845	±3	1.22
	0.75	11.0852	±2	1.28
	1.5	11.0854	±3	1.25

3.7.2.2.3 Temperature and strain discrimination

For the second test, we packaged the irradiated samples as described in part 3.7.2.1.2. We have then measured the temperature and the strain distributions along the fiber with the DTSS, applying different temperatures. The temperature results provided by the DTSS are represented in Figure 3.31, in a) the SMFV_1 and in b) the SMFV_2. Concerning the SMFV_1, the temperature provided by the sensor using the irradiated sample fits very well with the thermocouple response with a difference of less than 1 °C as detailed in TABLE 3.35. Regarding SMFV_2 fiber, the biggest difference between the thermocouple and the DOFS is 1.5 °C±1.1 °C for the 0.75 MGy sample at 50 °C and 2.3 °C±1.2 °C for the 1.5 MGy sample at 50 °C. This small difference between the thermocouple and the DOFS response could be probably be reduced by performing a better thermal isolation on the pristine fiber, improving this way the absolute temperature measurement.

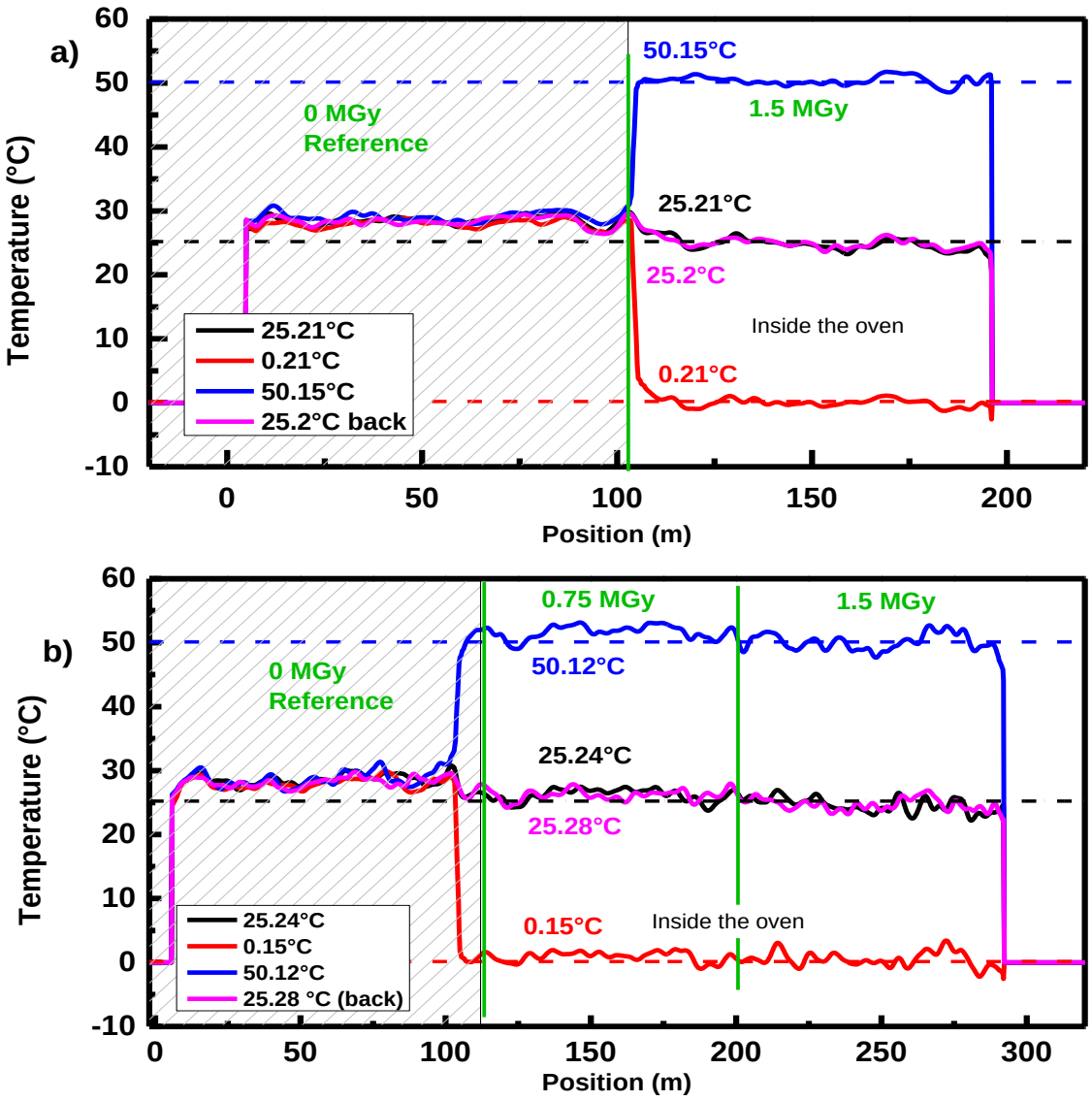

Figure 3.31: Temperature monitoring through LPR for non-irradiated and irradiated samples exposed at different temperatures a) SMFV_1 b) SMFV_2. The dashed area corresponds to our reference and the white one corresponds to the irradiated fibers in the oven. The dashed line indicates the temperature in the oven as provided by the thermocouple (TC).

TABLE 3.35: TEMPERATURE MEASUREMENTS THROUGH THE LPR AND WITH THE TC

Sample	Dose (MGy)	Temperature TC (°C)	DOFS Temperature (°C)	Difference (°C)
SMFV_1	1.5	25.2	24.8	0 ±1
		0.21	0.1	-0.1 ±0.9
		50.15	50.36	+0.2 ±0.7
		25.2	25	-0.2±0.8
SMFV_2	0.75	25.24	26.2	1.0±0.9
		0.15	0.9	0.8 ±0.8
		50.12	51.6	1.5 ±1.1
		25.28	26.2	0.9 ±0.8
	1.5	25.24	23.4	-1.8±1.1
		0.15	0.5	0.7±1.2
		50.12	47.8	2.3±1.2
		25.28	23.6	-1.7±0.9

From the LPR, we have deduced the strain along the fiber through the Brillouin frequency dependence. The distribution of strain is represented in Figure 3.32 a) for the SMFV_1 and in Figure 3.32 b) for the SMFV_2. Regarding the SMFV_1, the mean value of the microstrain at 1.5 MGy is 40 με with a dispersion of ±20 με, as detailed in TABLE 3.36, the large dispersion is explained by the averaging along the full sensing length. For the SMFV_2, mean value of the microstrain calculated with the same strain coefficients is 70 με ±30 με at 0.75 MGy and 50.12°C, and at 1.5 MGy the maximum mean micro-strain is 50 με ± 30με, at 24.25°C. In all cases, the strain along the fiber stays low and independent on the accumulated dose.

We can conclude that after an irradiation of 1.5 MGy, the performances of the DTSS are not affected. Indeed, we have seen that by choosing the appropriate fiber we can discriminate the temperature and the strain with a maximum error of 2 °C for the SMFV_2 or less than 1 °C

with the SMFV_1 for the temperature, and a maximum error of 40 με for the SMFV_1 and 70 με for the SMFV_2 for the strain. Moreover, for the strain measurement we have used the strain coefficient for the literature [145]. These results could be improved by performing a strain calibration and by performing a better thermal isolation of the fiber used as a reference. These results are satisfying and decide us to perform an online study under X-rays.

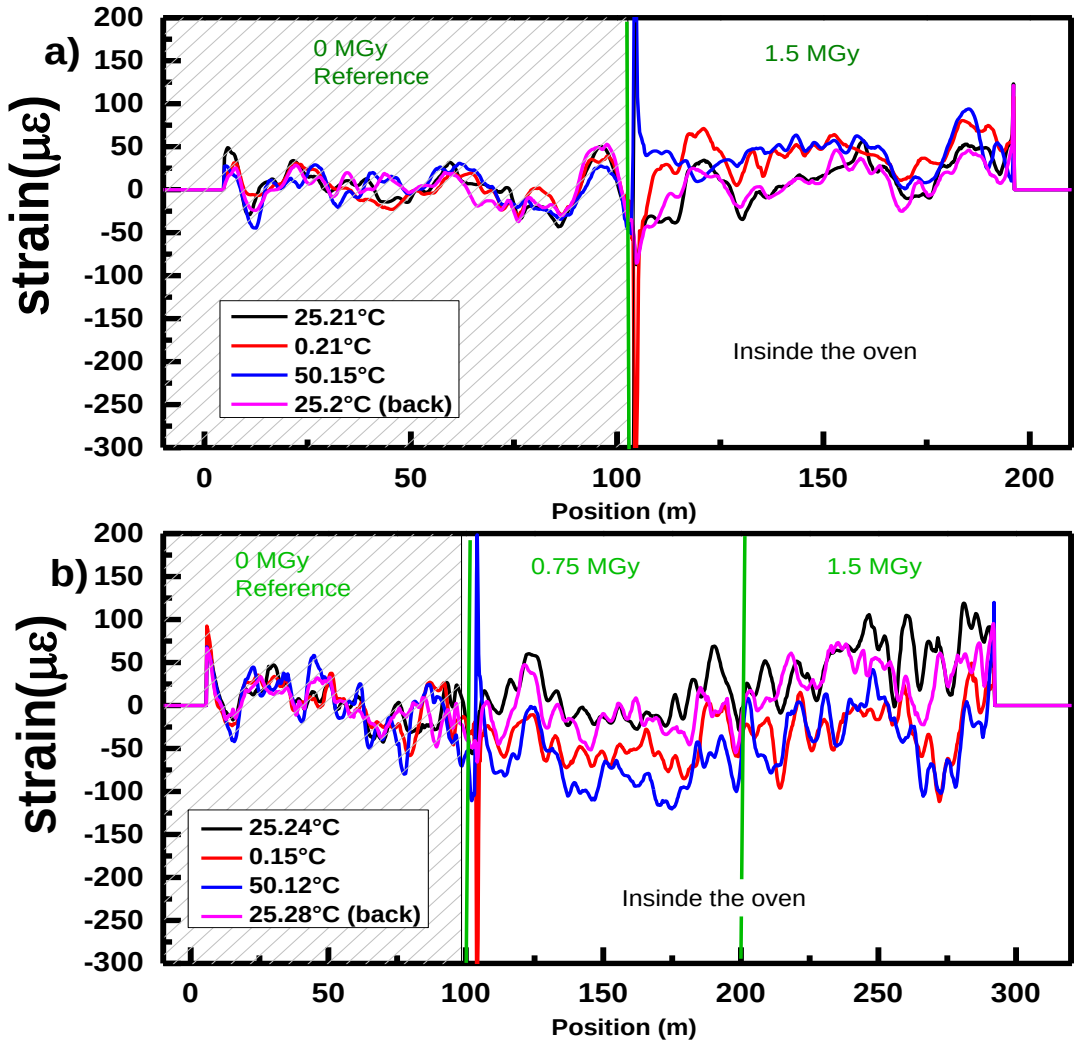

Figure 3.32: Strain response of (a) the SMFV-1 and (b) the SMFV_2, for the irradiated samples exposed at different temperatures. The white area corresponds to the irradiated fibers in the oven and the dashed area to our reference.

TABLE 3.36: STRAIN MEASUREMENT OF THE FIBER AT DIFFERENT TEMPERATURE FOR THE SMFV-1 IRRADIATED SAMPLE

Sample	Doses (MGy)	Temperature (°C)	Mean strain (με)	Strain error (με)
SMFV_1	0	27.4	0	20
	1.5	25.21	10	30
		0.21	40	20
		50.15	40	20
		25.2	0	20
SMFV_2	0	27.24	0	30
	0.75	24.25	0	30
		0.15	-50	20
		50.12	-70	30
		25.28	-10	20
	1.5	24.25	50	30
		0.15	-20	30
		50.12	-30	40
		25.25	40	30

3.7.3 Online Study

3.7.3.1 Irradiation facilities

For the online *X-rays* testing, the same fibers were selected. They have been irradiated with the MOPERIX X-ray machine from the Laboratoire Hubert Curien in Saint Etienne (France), delivering photons with an average photon energy of 45keV. The objective is to verify if the performances of the sensor are maintained during the irradiation and are not affected by transient mechanism.

3.7.3.2 Experimental setup

For this experiment, two samples of 15 m of the same fiber have been packaged as described in Figure 3.33. Both samples have been coiled with a diameter larger than 8 cm to be sure that all the samples will receive a homogeneous dose. The first sample has been irradiated while the second was shielded with lead (Pb plate). This configuration gives similar temperature and strain conditions for the irradiated and the shielded sample. As for the post-mortem study, we have used 100 m of pristine fiber thermally isolated with a PT100 (thermocouple) as the reference. Moreover, two type K thermocouples have been located close to the X-ray exposed sample and to the shielded sample to provide reference temperature measurements. The fiber has been irradiated with a dose-rate of ~1.4 Gy/s up to a dose of 0.5 MGy. During the irradiation run, we have performed the sensor measurement each 32 minutes with a spatial resolution of 30cm. The same experimental procedure has been repeated for the two fibers: SMFV_1 and SMFV_2.

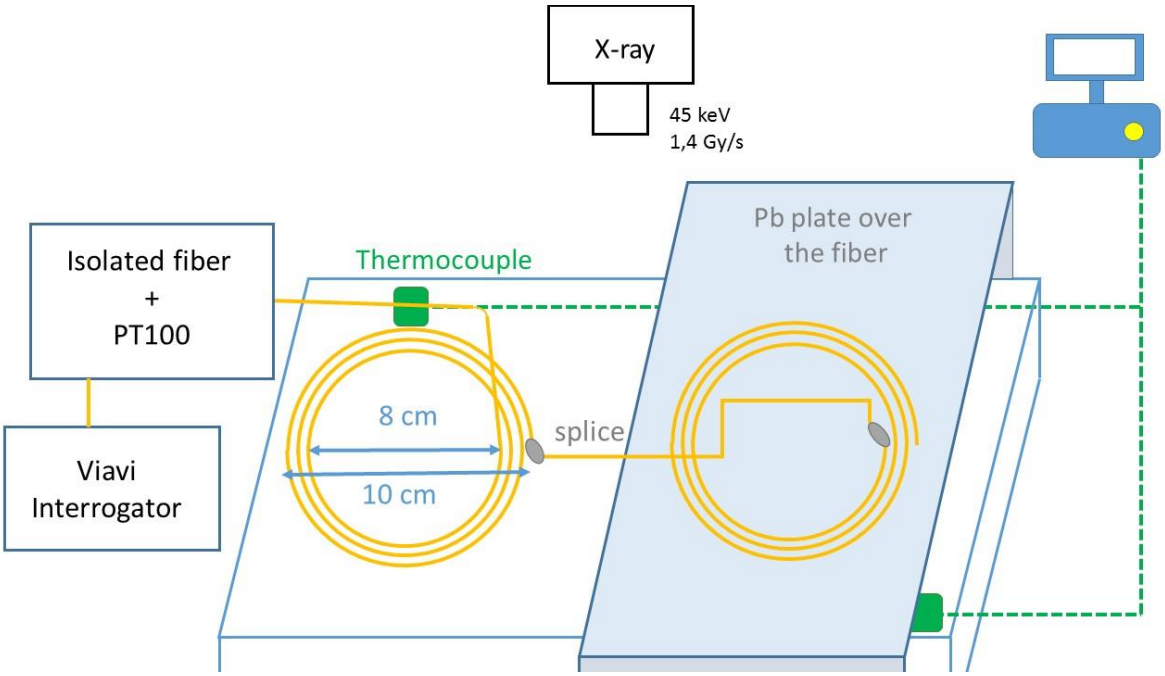

Figure 3.33: Experimental setup of online X-ray irradiation

3.7.3.3 Results

The time evolution of the temperature measured by the DOFS is compared with the one provided by the thermocouples close (blue line) to the irradiated sample (black dots) and to the shielded sample (red dots) in Figure 3.34. The dots represent an average value and the error bars correspond to the SD of the different spatial points. Concerning the SMFV_1, the maximum difference between the irradiated and shielded samples is 1.5 °C at 10 kGy. In comparison with TC, the highest difference is 1.8°C and 1.3°C for the irradiated and shielded samples as detailed in TABLE 3.37. Regarding the SMFV_2, the maximum difference between the irradiated and shielded samples is 2.4°C at 350 kGy, and in comparison with the TC the highest difference is 1.5°C and 1.1°C for the irradiated and the shielded sample. For both fibers, the temperature measurement with the irradiated and shielded samples is very close to the TC measurements. The small difference could be explained by the different localizations of the devices. Therefore, we assume that the radiation does not affect the temperature measurement within ~1 °C.

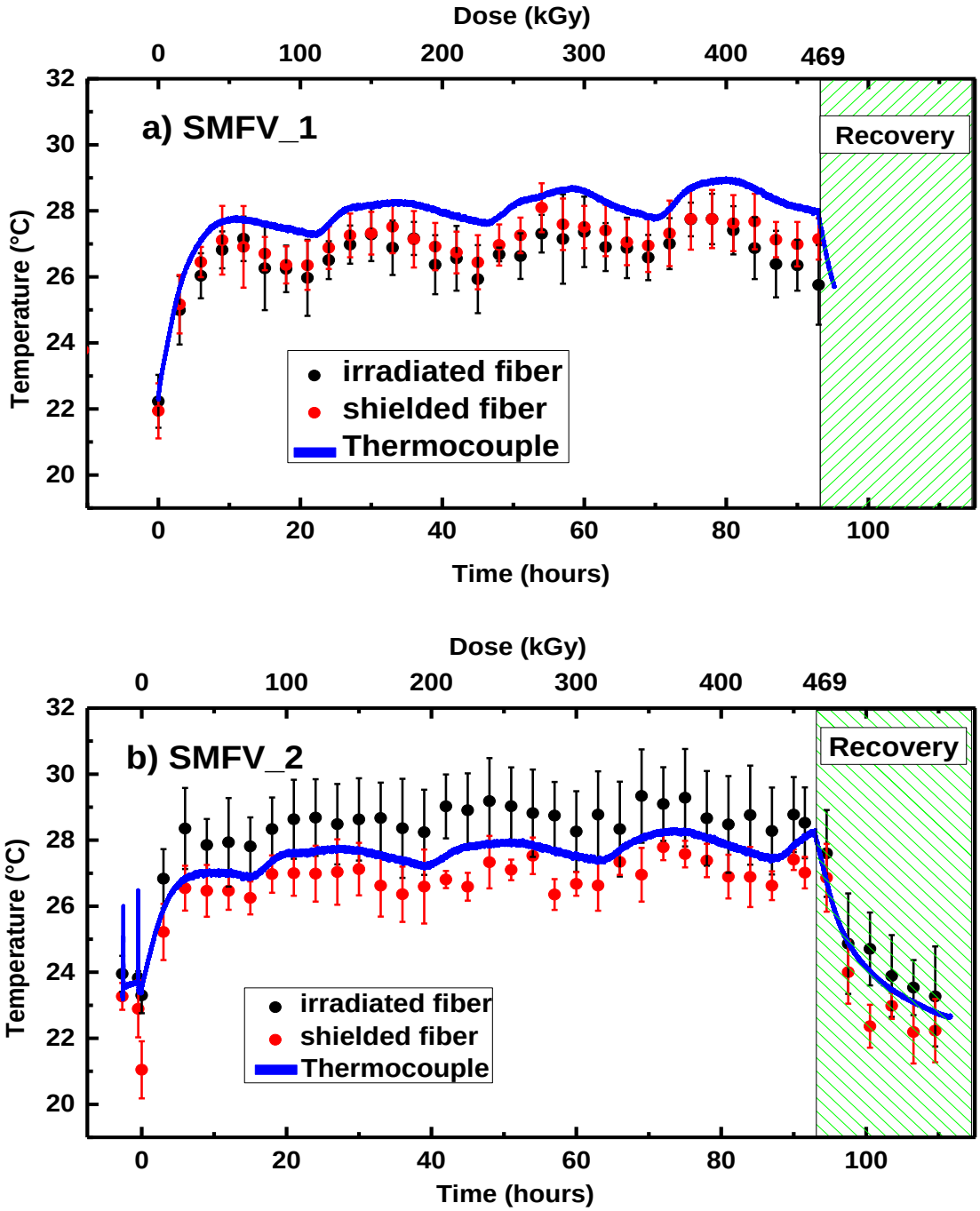

Figure 3.34: Comparison between the temperatures measured by the fiber sensor and the thermocouples during the X-ray irradiation (1.4 Gy/s) at RT. In a) the SMFV_1 and in b) the SMFV_2. The blue line illustrates the thermocouple response, black and red dots represent the temperature measurements performed by the irradiated fiber and the shielded one, respectively

TABLE 3.37: COMPARISON OF TEMPERATURE MEASUREMENTS PERFORMED BY IRRADIATED AND SHIELDED FIBER AND THERMOCOUPLE

Sample	ΔT °C (Irradiated-shielded)		ΔT °C (Irradiated-Thermocouple)		ΔT °C (Shielded-Thermocouple)	
	mean	max	mean	max	mean	max
SMFV_1	0.6	1.5	1.3	1.8	1.0	1.3
SMFV_2	1.6	2.4	0.9	1.5	0.8	1.1

Finally, the impact of the strain measurement has been investigated and is represented in Figure 3.35. The red dots represent the mean strain measurement of the shielded sample whereas the black dots represent the ones of the irradiated sample. The error bars corresponds to the SD of the strain measurement for the different spatial points. For the SMFV_1, the strain average is 7με (±40με) for the irradiated fiber, and -7 με (±50 με) for the shielded one. Concerning the SMFV_2, the average strain is -17 με (±50 με) for the irradiated fiber, and 19με (±50με) for the non-irradiated fiber. The sensor performances in terms of strain measurements seem not to evolve during the radiation. The max error is of about ±50 με due to the distributed capacities.

As after irradiation, the sensing performance of the DTSS seems not affected during the radiation up to 0.5 MGy with maximal errors of 1 °C and 50 με. Then, by combining the LPR and the Brillouin frequency, we are able to discriminate the strain and the temperature effect over 10 km with 1 m of spatial resolution in “standard case”. In radiation environment, these discrimination performances are maintained but the RIA will affect the achievable sensing length by the interrogator.

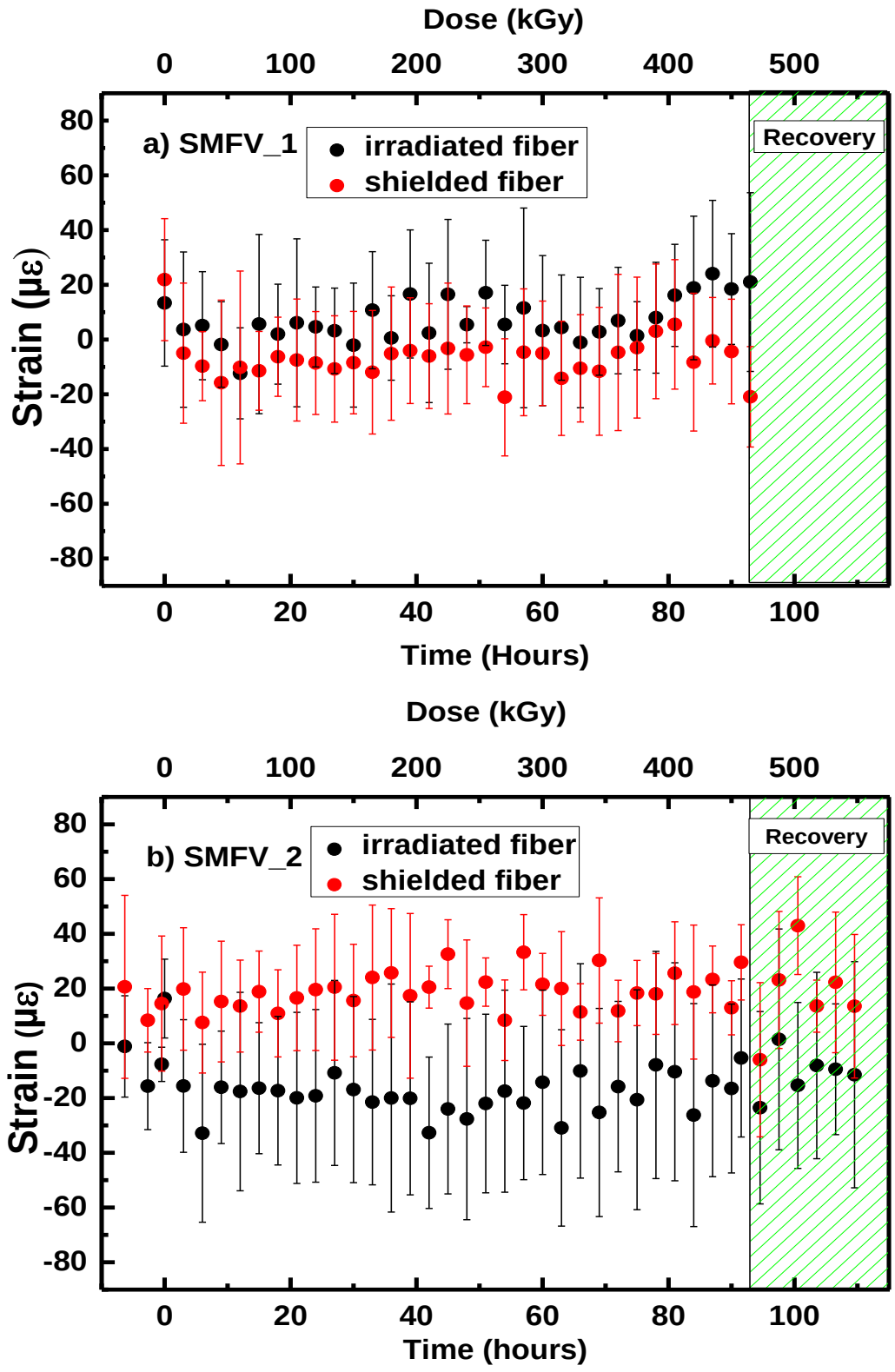

Figure 3.35: Comparison between the strain values measured by the fiber sensor during the X-ray irradiation (1.4 Gy/s) at RT on the irradiated and shielded samples. In a) the SMF_1 and in b) the SMF_2. Red dots correspond to the non-irradiated fiber and black dots

3.8 Conclusion

In this chapter, we have investigated the potential of two different solutions for the discrimination between the strain and the temperature on a single optical fiber. The first one is to use a fiber providing several Brillouin frequency peaks. From our developed simulation tools, we have been able to identify and manufacture two types of fiber with different dopants and with Telecom capacities in terms of attenuation. Six samples have been produced with different conditions of drawing. Comparing their experimental signature to the ones predicted by simulation, we confirm the pertinence of our simulation procedure.

Our work allows developping different fibers with good capacities of discrimination. Two samples propose a better discrimination capacity than the ones reported by other research teams in literature, with an error of 3.6 °C/MHz / 93 με/MHz for the SMFS_F2 sample and an error of 4.8 °C/MHz / 104 με/MHz for the SMFS_Ge1. In comparison, the more efficient reported optical fiber offers the discrimination with an error of 6.6 °C/MHz / 138 με/MHz. Moreover, our fibers are characterized by low attenuations at 1550 nm and are compatible with both BOTDA and BOTDR technologies.

A second approach has been studied during the PhD thesis thanks to a collaboration with Viavi-solutions. This manufacturer has developed an interrogator, the DTSS, allowing to discriminate the temperature and the strain distributions by performing both Brillouin and Rayleigh backscattering measurements on the same fiber. Two radiation-hardened optical fibers have been tested with this interrogator. Due to the huge interest of the nuclear industry for the distributed sensors, we have performed a study in radiation environment. These preliminary results confirm that the sensor performances are maintained under irradiation and open the way to a new generation of sensor by combining the interrogator of Viavi-solutions and the fiber(s) developed during this PhD thesis.

Summary (EN)

For this last chapter, an optimization of two optical fiber structures was modeled, which made it possible to highlight the robustness of the simulation model. Subsequently, these two structures were manufactured. Tests on fiber conditions were carried out in order to obtain a fiber with the best temperature / strain discrimination capabilities and to verify the robustness of the manufacturing. All the fibers presented have a Brillouin signature with several peaks. The experimental results were compared with the simulation data and show similar results. The discrimination capabilities of optical fibers have been verified and compared with the fibers already on the market. Some fibers presented in this chapter show discriminating capabilities superior to the fibers reported in literature. Finally, a study of temperature / deformation discrimination in a radiative medium was presented. To discriminate, an interrogator based on Brillouin and Rayleigh scattering was used. The results show a good capacity of discrimination and this for doses up to 1 MGy.

Résumé (FR)

Pour ce dernier chapitre, deux structures de fibre optique ont été optimisées par simulation, ce qui a permis de mettre en avant la robustesse de nos modèles. Par la suite, ces deux fibres optiques ont été fabriquées. Des tests sur les conditions de fibrages ont été réalisés afin d'obtenir une fibre avec les meilleurs capacités possibles de discrimination entre la température et la déformation et de vérifier la robustesse de la fabrication. Toutes les fibres fabriquées présentent une signature Brillouin avec plusieurs pics. Les résultats expérimentaux ont été comparés avec les calculs et confirment notre capacité de prédiction. Les capacités de discrimination des fibres optiques ont été vérifiées et comparées avec les fibres déjà présentes sur le marché. Certaines fibres présentées dans ce chapitre montrent des capacités de discrimination supérieures aux meilleures fibres de la littérature. Enfin, une étude de discrimination température/déformation en milieu radiatif a été présentée. Pour ce faire, un nouvel interrogateur, développé par Viavi Solutions, se basant sur la diffusion Brillouin et Rayleigh a été utilisé. Les résultats montrent que sa bonne capacité de discrimination est maintenue sous irradiation, et ce pour des doses allant jusqu'à 1 MGy.

Riassunto (IT)

In questo capitolo, è riportata la procedura di ottimizzazione e i corrispondenti risultati relativi a due differenti strutture di fibre ottiche. Tale studio, ha evidenziato la proprietà di robustezza del modello di simulazione sviluppato. Sono presentati inoltre i prototipi delle due fibre ottiche risultanti dal processo di ottimizzazione. Sono stati effettuati alcuni test sulle condizioni di tiraggio della fibra ottica al fine di ottenere le migliori capacità di discriminazione di temperatura/deformazione nonché di verificare la robustezza della fabbricazione. Tutte le fibre ottiche presentate sono caratterizzate da una risposta di Brillouin con picchi multipli. Successivamente, è stato effettuato il confronto tra dati sperimentali e di simulazione ottenendo un ottimo accordo. Inoltre, sono state verificate le capacità di discriminazione delle fibre ottiche fabbricate ed è stato effettuato un confronto con quelle già esistenti in commercio. Per alcune di esse, sono state osservate delle prestazioni migliori di quelle della corrispondente fibra ottica di riferimento: la Leaf. Infine, è stato presentato uno studio sulla discriminazione di temperatura/deformazione in ambiente radiativo. Per effettuare tale discriminazione, è stato utilizzato un interrogatore basato sul fenomeno fisico dello scattering di Brillouin e di Rayleigh. I risultati ottenuti mostrano una buona capacità di discriminazione, anche per dosi fino al 1 MGy.

References

[1] M. L. Filograno *et al.*, "Real-Time Monitoring of Railway Traffic Using Fiber Bragg Grating Sensors," *IEEE Sens. J.*, vol. 12, no. 1, pp. 85–92, Jan. 2012.

[2] S. Rizzolo *et al.*, "Radiation Characterization of Optical Frequency Domain Reflectometry Fiber-Based Distributed Sensors," *IEEE Trans. Nucl. Sci.*, vol. 63, no. 3, pp. 1688–1693, Jun. 2016.

[3] D. D. Francesca, G. L. Vecchi, Y. Kadi, M. Brugger, S. Girard, and A. Alessi, "Implementation of Optical Fiber based Dosimetry at CERN," in *26th International Conference on Optical Fiber Sensors (2018), paper WC1*, 2018, p. WC1.

[4] C. Sabatier *et al.*, "6-MeV Electron Exposure Effects on OFDR-Based Distributed Fiber-Based Sensors," *IEEE Trans. Nucl. Sci.*, vol. 65, no. 8, pp. 1598–1603, Aug. 2018.

[5] D. D. Francesca *et al.*, "Distributed Optical Fiber Radiation Sensing in the Proton Synchrotron Booster at CERN," *IEEE Trans. Nucl. Sci.*, vol. 65, no. 8, pp. 1639–1644, Aug. 2018.

[6] S. Delepine-Lesoille *et al.*, "France's State of the Art Distributed Optical Fibre Sensors Qualified for the Monitoring of the French Underground Repository for High Level and Intermediate Level Long Lived Radioactive Wastes," *Sensors*, vol. 17, no. 6, p. 1377, Jun. 2017.

[7] R. Di Sante, "Fibre Optic Sensors for Structural Health Monitoring of Aircraft Composite Structures: Recent Advances and Applications," *Sensors*, vol. 15, no. 8, pp. 18666–18713, Aug. 2015.

[8] O. J. Ohanian *et al.*, "OFDR on Photonic Circuits: Fiber Optic Sensing Infrastructure and Applications," in *26th International Conference on Optical Fiber Sensors (2018), paper WB1*, 2018, p. WB1.

[9] L. Schenato, "Distributed Sensing in Geotechnical and Hydrological Applications," in *26th International Conference on Optical Fiber Sensors (2018), paper ThB1*, 2018, p. ThB1.

[10] F. Ravet, S. Chin, and E. Rochat, "Field Experience with DTSS based Geotechnical Monitoring: Lessons Learnt and Guidelines," in *26th International Conference on Optical Fiber Sensors (2018), paper ThB2*, 2018, p. ThB2.

[11] R. Fiorin, A. P. G. O. Franco, P. F. Nascimento, M. A. de Souza, H. J. Kalinowski, and I. Abe, "The use of fiber Bragg gratings in the detection of the rhythmic masticatory muscle activity during bruxism episodes," in *26th International Conference on Optical Fiber Sensors (2018), paper WF1*, 2018, p. WF1.

[12] "Optical Communication and Networking Market worth 24.12 Billion USD by 2023." [Online]. Available: https://www.marketsandmarkets.com/PressReleases/optical-networking-communications.asp. [Accessed: 20-Feb-2019].

[13] "Optical Sensors Market Size, Share - Industry Forecast Report 2024." [Online]. Available: https://www.gminsights.com/industry-analysis/optical-sensor-market. [Accessed: 20-Feb-2019].

[14] "Les Etats-Unis trustent le marché mondial des capteurs à fibre optique." [Online]. Available: http://www.mesures.com/instrumentation/mesure-physique/item/11816-les-etats-unis-trustent-le-marche-mondial-des-capteurs-a-fibre-optique. [Accessed: 20-Feb-2019].

[15] J. S. Selker *et al.*, "Distributed fiber-optic temperature sensing for hydrologic systems," *Water Resour. Res.*, vol. 42, no. 12, 2006.

[16] T. Horiguchi, T. Kurashima, and M. Tateda, “A technique to measure distributed strain in optical fibers,” *IEEE Photonics Technol. Lett.*, vol. 2, no. 5, pp. 352–354, May 1990.
[17] G. B. Hocker, “Fiber-optic sensing of pressure and temperature,” *Appl. Opt.*, vol. 18, no. 9, pp. 1445–1448, May 1979.
[18] Z. Ding *et al.*, “Distributed Optical Fiber Sensors Based on Optical Frequency Domain Reflectometry: A review,” *Sensors*, vol. 18, no. 4, p. 1072, Apr. 2018.
[19] Y. Koyamada, M. Imahama, K. Kubota, and K. Hogari, “Fiber-Optic Distributed Strain and Temperature Sensing With Very High Measurand Resolution Over Long Range Using Coherent OTDR,” *J. Light. Technol.*, vol. 27, no. 9, pp. 1142–1146, May 2009.
[20] H. Ohno, H. Naruse, M. Kihara, and A. Shimada, “Industrial Applications of the BOTDR Optical Fiber Strain Sensor,” *Opt. Fiber Technol.*, vol. 7, no. 1, pp. 45–64, Jan. 2001.
[21] Z. Amira, M. Bouyahi, and T. Ezzedine, “Measurement of Temperature through Raman Scattering,” *Procedia Comput. Sci.*, vol. 73, pp. 350–357, Jan. 2015.
[22] S. Rizzolo, “Advantages and Limitation of Distributed OFDR Optical Fiber-based sensors in Harsh Environments,” Ph.D Thesis, Université Jean Monnet Saint Etienne, Saint Etienne, France, 2016.
[23] M. K. Barnoski and S. M. Jensen, “Fiber waveguides: a novel technique for investigating attenuation characteristics,” *Appl. Opt.*, vol. 15, no. 9, pp. 2112–2115, Sep. 1976.
[24] T. Kurashima, T. Horiguchi, and M. Tateda, “Distributed-temperature sensing using stimulated Brillouin scattering in optical silica fibers,” *Opt. Lett.*, vol. 15, no. 18, pp. 1038–1040, Sep. 1990.
[25] J. P. Dakin, D. J. Pratt, G. W. Bibby, and J. N. Ross, “Distributed optical fibre Raman temperature sensor using a semiconductor light source and detector,” *Electron. Lett.*, vol. 21, no. 13, p. 569, 1985.
[26] M. B. Hausner, F. Suárez, K. E. Glander, N. van de Giesen, J. S. Selker, and S. W. Tyler, “Calibrating Single-Ended Fiber-Optic Raman Spectra Distributed Temperature Sensing Data,” *Sensors*, vol. 11, no. 11, pp. 10859–10879, Nov. 2011.
[27] W. Eickhoff and R. Ulrich, “Optical frequency domain reflectometry in single-mode fiber,” *Appl. Phys. Lett.*, vol. 39, no. 9, pp. 693–695, Nov. 1981.
[28] D. Garus, K. Krebber, F. Schliep, and T. Gogolla, “Distributed sensing technique based on Brillouin optical-fiber frequency-domain analysis,” *Opt. Lett.*, vol. 21, no. 17, pp. 1402–1404, Sep. 1996.
[29] M. A. Farahani and T. Gogolla, “Spontaneous Raman Scattering in Optical Fibers with Modulated Probe Light for Distributed Temperature Raman Remote Sensing,” *J. Light. Technol.*, vol. 17, no. 8, p. 1379, Aug. 1999.
[30] Y. S. Muanenda *et al.*, “Advanced Coding Techniques for Long-Range Raman/BOTDA Distributed Strain and Temperature Measurements,” *J. Light. Technol.*, vol. 34, no. 2, pp. 342–350, Jan. 2016.
[31] D. Hwang, D.-J. Yoon, I.-B. Kwon, D.-C. Seo, and Y. Chung, “Novel auto-correction method in a fiber-optic distributed-temperature sensor using reflected anti-Stokes Raman scattering,” *Opt. Express*, vol. 18, no. 10, pp. 9747–9754, May 2010.
[32] A. Morana, “Gamma-rays and neutrons effects on optical fibers and Bragg gratings for temperature sensors,” Ph.D Thesis, Université Jean Monnet Saint Etienne, Saint Etienne, France, 2013.
[33] S. Girard *et al.*, “Recent advances in radiation-hardened fiber-based technologies for space applications,” *J. Opt.*, vol. 20, no. 9, p. 093001, 2018.

[34] A. F. Fernandez *et al.*, “Radiation-tolerant Raman distributed temperature monitoring system for large nuclear infrastructures,” *IEEE Trans. Nucl. Sci.*, vol. 52, no. 6, pp. 2689–2694, Dec. 2005.
[35] L. Schenato, “A Review of Distributed Fibre Optic Sensors for Geo-Hydrological Applications,” *Appl. Sci.*, vol. 7, no. 9, p. 896, Sep. 2017.
[36] S. Sakaguchi, S. Todoroki, and T. Murata, “Rayleigh scattering in silica glass with heat treatment,” *J. Non-Cryst. Solids*, vol. 220, no. 2, pp. 178–186, Nov. 1997.
[37] Y. Li, F. Zhang, and T. Yoshino, “Wide temperature-range Brillouin and Rayleigh optical-time-domain reflectometry in a dispersion-shifted fiber,” *Appl. Opt.*, vol. 42, no. 19, pp. 3772–3775, Jul. 2003.
[38] I. Toccafondo, “Distributed Optical Fiber Radiation and Temperature Sensing at High Energy Accelerators and Experiments,” Ph.D Thesis, Scuola Superiore Sant’Anna, Pisa, Italy, 2015.
[39] R. G. Duncan *et al.*, “OFDR-Based Distributed Sensing and Fault Detection for Single- and Multi-Mode Avionics Fiber-Optics,” p. 6.
[40] C. Sabatier *et al.*, “Potential of Optical Frequency Domain Reflectometry fibre-based sensors for distributed temperature measurements during vacuum thermal cycling of satellites,” p. 11.
[41] M. Froggatt and J. Moore, “High-spatial-resolution distributed strain measurement in optical fiber with Rayleigh scatter,” *Appl. Opt.*, vol. 37, no. 10, pp. 1735–1740, 1998.
[42] “OSA | High Resolution Distributed Strain or Temperature Measurements in Single-and Multi-mode Fiber Using Swept-Wavelength Interferometry.” [Online]. Available: https://www.osapublishing.org/abstract.cfm?uri=OFS-2006-ThE42. [Accessed: 28-May-2019].
[43] K. Lim, L. Wong, W. K. Chiu, and J. Kodikara, “Distributed fiber optic sensors for monitoring pressure and stiffness changes in out-of-round pipes,” *Struct. Control Health Monit*, vol. 23, no. 2, pp. 303–314, Feb. 2016.
[44] T. Guo, A. Li, Y. Song, B. Zhang, Y. Liu, and N. Yu, “Experimental study on strain and deformation monitoring of reinforced concrete structures using PPP-BOTDA,” *Sci. China Ser. E Technol. Sci.*, vol. 52, no. 10, pp. 2859–2868, Oct. 2009.
[45] C. Cangialosi, “Performances of Raman and Brillouin fiber-based sensing of temperature and strain in harsh environments,” Ph.D Thesis, Université de Lyon, 2016.
[46] V. Lanticq, “Mesure répartie de température et de déformations par diffusion Brillouin: de la fibre optique au capteur pour le génie civil,” Ph.D Thesis, TELECOM ParisTech, Paris, 2009.
[47] M. Nikles, “La diffusion Brillouin dans les fibres optiques: Etudes et application aux capteurs distribués,” Ph.D Thesis, EPFL, Lausanne, 1997.
[48] R. W. Boyd, *Nonlinear Optics*. Academic Press, 2013.
[49] X. Bao and L. Chen, “Recent Progress in Distributed Fiber Optic Sensors,” *Sensors*, vol. 12, no. 7, pp. 8601–8639, Jul. 2012.
[50] Y. S. Mamdem, “Capteurs à fibres optiques répartis par effet Brillouin: séparation de la dépendance à température et à la déformation,” Ph.D Thesis, TELECOM ParisTech, 2014.
[51] C. Sabatier *et al.*, “Influence of the core dopants on the Brillouin signature of specialty optical fibers,” in *5th Workshop on Specialty Optical Fibers and their Applications*, Limassol , Cyprus, 2017.
[52] T. Kurashima, T. Horiguchi, H. Izumita, S. ichi Furukawa, and Y. Koyamada, “Brillouin optical-fiber time domain reflectometry,” *IEICE Trans. Commun.*, vol. E76-B, no. 4, pp. 382–390, Apr. 1993.

[53] X. Bao, D. J. Webb, and D. A. Jackson, “32-km distributed temperature sensor based on Brillouin loss in an optical fiber,” *Opt. Lett.*, vol. 18, no. 18, pp. 1561–1563, Sep. 1993.
[54] M. Niklès, L. Thévenaz, and P. A. Robert, “Simple distributed fiber sensor based on Brillouin gain spectrum analysis,” *Opt. Lett.*, vol. 21, no. 10, pp. 758–760, May 1996.
[55] R. Bautz, L. Thevenaz, and M. Nikles, “Procédé de mesure de la diffusion Brillouin dans une fibre optique et dispositif de mise en Óoeuvre de ce procédé,” FR2710150B1, 17-Nov-1995.
[56] G. Failleau *et al.*, “A metrological comparison of Raman-distributed temperature sensors,” *Measurement*, vol. 116, pp. 18–24, Feb. 2018.
[57] S. Delepine-Lesoille, I. Planes, M. Landolt, G. Hermand, and O. Perrochon, “Compared performances of Rayleigh Raman and Brillouin distributed temperature measurements during concrete container fire test,” in *2017 25th Optical Fiber Sensors Conference (OFS)*, 2017, pp. 1–4.
[58] D. Inaudi and B. Glisic, “Long-Range Pipeline Monitoring by Distributed Fiber Optic Sensing | Journal of Pressure Vessel Technology | ASME DC,” *J Press. Vessel Technol*, vol. 132, no. 011701–9, Dec. 2009.
[59] K. Hotate and T. Hasegawa, *Measurement of Brillouin Gain Spectrum Distribution along an Optical Fiber Using a Correlation-Based Technique – Proposal, Experiment and Simulation*. 2000.
[60] Z. Li, Z. Yang, L. Yan, M. A. Soto, and L. Thévenaz, “Hybrid Golay-coded Brillouin optical time-domain analysis based on differential pulses,” *Opt. Lett.*, vol. 43, no. 19, pp. 4574–4577, Oct. 2018.
[61] Y. Dong, H. Zhang, L. Chen, and X. Bao, “A 2-cm-spatial-resolution and 2-km-range Brillouin optical fiber sensor using a transient differential pulse pair,” *Appl. Opt.*, vol. 51, no. 9, pp. 1229–1235, Mar. 2012.
[62] Y. Dong, L. Chen, and X. Bao, “Extending the Sensing Range of Brillouin Optical Time-Domain Analysis Combining Frequency-Division Multiplexing and In-Line EDFAs,” *J. Light. Technol.*, vol. 30, no. 8, pp. 1161–1167, Apr. 2012.
[63] H.-N. Li, D.-S. Li, and G.-B. Song, “Recent applications of fiber optic sensors to health monitoring in civil engineering,” *Eng. Struct.*, vol. 26, no. 11, pp. 1647–1657, Sep. 2004.
[64] “Fiber Optic Sensors | VIAVI Solutions Inc.” [Online]. Available: https://www.viavisolutions.com/en-us/product-category/fiber-optic-sensors. [Accessed: 18-Feb-2019].
[65] “Neubrex Co., Ltd. - NEUBRESCOPE.” [Online]. Available: http://www.neubrex.com/htm/products/pro-nbx6000.htm. [Accessed: 18-Feb-2019].
[66] “systeme – FEBUS-OPTICS.” [Online]. Available: http://febus-optics.com/1/en/technology/systeme/. [Accessed: 18-Feb-2019].
[67] D.-P. Zhou, W. Li, L. Chen, and X. Bao, “Distributed Temperature and Strain Discrimination with Stimulated Brillouin Scattering and Rayleigh Backscatter in an Optical Fiber,” *Sensors*, vol. 13, no. 2, pp. 1836–1845, Feb. 2013.
[68] Y. Li, L. Zhang, H. Fan, and H. Li, “A performance enhanced Rayleigh Brillouin optical time domain analysis sensing system,” *Optoelectron. Lett*, vol. 14, no. 2, pp. 84–87, Mar. 2018.
[69] C. Sabatier *et al.*, “Distributed Optical Fiber Sensor Allowing Temperature and Strain Discrimination in Radiation Environments.”
[70] M. N. Alahbabi, Y. T. Cho, and T. P. Newson, “Simultaneous temperature and strain measurement with combined spontaneous Raman and Brillouin scattering,” *Opt. Lett.*, vol. 30, no. 11, pp. 1276–1278, Jun. 2005.

[71] X. Bao, Q. Yu, and L. Chen, “Simultaneous strain and temperature measurements with polarization-maintaining fibers and their error analysis by use of a distributed Brillouin loss system,” *Opt. Lett.*, vol. 29, no. 12, pp. 1342–1344, Jun. 2004.
[72] F. Zhang and J. W. Y. Lit, “Temperature and strain sensitivity measurements of high-birefringent polarization-maintaining fibers,” *Appl. Opt.*, vol. 32, no. 13, pp. 2213–2218, May 1993.
[73] Y. Dong, L. Chen, and X. Bao, “High-Spatial-Resolution Time-Domain Simultaneous Strain and Temperature Sensor Using Brillouin Scattering and Birefringence in a Polarization-Maintaining Fiber,” *IEEE Photonics Technol. Lett.*, vol. 22, no. 18, pp. 1364–1366, Sep. 2010.
[74] “LEAF® Optical Fiber | Long-haul and Metro Network Solution | Corning.” [Online]. Available: https://www.corning.com/worldwide/en/products/communication-networks/products/fiber/leaf-fiber.html. [Accessed: 26-Feb-2019].
[75] M. Alahbabi, Y. T. Cho, and T. P. Newson, “Comparison of the methods for discriminating temperature and strain in spontaneous Brillouin-based distributed sensors,” *Opt. Lett.*, vol. 29, no. 1, pp. 26–28, Jan. 2004.
[76] X. Liu and X. Bao, “Brillouin Spectrum in LEAF and Simultaneous Temperature and Strain Measurement,” *J. Light. Technol.*, vol. 30, no. 8, pp. 1053–1059, Apr. 2012.
[77] L. Zou, X. Bao, S. A. V, and L. Chen, “Dependence of the Brillouin frequency shift on strain and temperature in a photonic crystal fiber,” *Opt. Lett.*, vol. 29, no. 13, pp. 1485–1487, Jul. 2004.
[78] “Polarization-Maintaining Photonic Crystal Fibers.” [Online]. Available: https://www.thorlabs.com/newgrouppage9.cfm?objectgroup_id=910. [Accessed: 27-Feb-2019].
[79] V. Shahraam Afshar, K. V.P, B. Xiaoyi, and C. Liang, “Simultaneous distributed strain and temperature measurement,” *Opt. Lett.*, vol. 30, no. 20, pp. 2685–2687, 2005.
[80] A. Ladaci, “Rare Earth Doped Optical Fibers and Amplifiers for Space Applications,” 2017.
[81] L. Tartara, C. Codemard, J.-N. Maran, R. Cherif, and M. Zghal, “Full modal analysis of the Brillouin gain spectrum of an optical fiber,” *Opt. Commun.*, vol. 282, no. 12, pp. 2431–2436, Jun. 2009.
[82] Y. Koyamada, S. Sato, S. Nakamura, H. Sotobayashi, and W. Chujo, “Simulating and designing Brillouin gain spectrum in single-mode fibers,” *J. Light. Technol.*, vol. 22, no. 2, pp. 631–639, Feb. 2004.
[83] “Corning SMF-28 Ultra Fibre optique.” [Online]. Available: https://www.corning.com/media/worldwide/coc/documents/Fiber/PI1424_11-14_fr-FR.pdf. [Accessed: 17-Oct-2018].
[84] C.-K. Jen, C. Neron, A. Shang, K. Abe, L. Bonnell, and J. Kushibiki, “Acoustic Characterization of Silica Glasses,” *J. Am. Ceram. Soc.*, vol. 76, no. 3, pp. 712–716, Mar. 1993.
[85] Y. S. Mamdem, “Capteurs à fibres optiques répartis par effet Brillouin : séparation de la dépendance à température et à la déformation,” phdthesis, Télécom ParisTech, 2012.
[86] A. Kobyakov *et al.*, “Design concept for optical fibers with enhanced SBS threshold,” *Opt. Express*, vol. 13, no. 14, pp. 5338–5346, Jul. 2005.
[87] P.-C. Law, Y.-S. Liu, A. Croteau, and P. D. Dragic, “Acoustic coefficients of P_2O_5-doped silica fiber: acoustic velocity, acoustic attenuation, and thermo-acoustic coefficient,” *Opt. Mater. Express*, vol. 1, no. 4, pp. 686–699, Aug. 2011.
[88] L. G. Hwa and W. C. Chao, “Velocity of sound and elastic properties of lanthanum gallo-germanate glasses,” *Mater. Chem. Phys.*, vol. 94, no. 1, pp. 37–41, Nov. 2005.

[89] P. D. Dragic, “Simplified model for effect of Ge doping on silica fibre acoustic properties,” *Electron. Lett.*, vol. 45, no. 5, pp. 256–257, Feb. 2009.
[90] A. V. Anan’ev *et al.*, “Origin of Rayleigh scattering and anomaly of elastic properties in vitreous and molten GeO2,” *J. Non-Cryst. Solids*, vol. 354, no. 26, pp. 3049–3058, May 2008.
[91] J. Smith, A. Brown, M. DeMerchant, and B. Xiaoyi, “Enhancement of stimulated Brillouin scattering of higher-order acoustic modes in single-mode optical fiber,” *Appl. Opt.*, vol. 38, no. 25, pp. 5372–5377, 1999.
[92] P. D. Dragic, “Proposed model for the effect of Ge-doping on the acoustic properties of silica fibers,” in *2009 Conference on Optical Fiber Communication - incudes post deadline papers*, 2009, pp. 1–3.
[93] E. T. Y. Lee, “Development and characterisation of phosphate glasses for athermalisation,” phd, University of Southampton, 2004.
[94] M. Cavillon, P. D. Dragic, and J. Ballato, “Additivity of the coefficient of thermal expansion in silicate optical fibers,” *Opt. Lett.*, vol. 42, no. 18, pp. 3650–3653, Sep. 2017.
[95] P. Dragic, M. Cavillon, C. Kucera, J. Parsons, T. Hawkins, and J. Ballato, “Tailoring the Thermo-Optic Coefficient in Silica Optical Fibers.”
[96] P. D. Dragic, M. Cavillon, A. Ballato, and J. Ballato, “A unified materials approach to mitigating optical nonlinearities in optical fiber. II. B. The optical fiber, material additivity and the nonlinear coefficients,” *Int. J. Appl. Glass Sci.*, vol. 9, no. 3, pp. 307–318, Jul. 2018.
[97] P. D. Dragic, “Brillouin Gain Reduction Via B2O3 Doping,” *J. Light. Technol.*, vol. 29, no. 7, pp. 967–973, Apr. 2011.
[98] M. Cavillon *et al.*, “Brillouin Properties of a Novel Strontium Aluminosilicate Glass Optical Fiber,” *J. Light. Technol.*, vol. 34, no. 6, pp. 1435–1441, Mar. 2016.
[99] J. W. Fleming, “Dispersion in GeO_2–SiO_2 glasses,” *Appl. Opt.*, vol. 23, no. 24, pp. 4486–4493, Dec. 1984.
[100] Lin M. ., “Anomalous Temperature Dependence of Ultrasonic Velocity in Potassium Silicate Glasses,” *Chin. J. Phys.*, vol. 23, no. 4, pp. 235–244, Dec. 1985.
[101] S. Spinner, “Temperature Dependence of Elastic Constants of Vitreous Silica,” *J. Am. Ceram. Soc.*, vol. 45, no. 8, pp. 394–397, Aug. 1962.
[102] M. Dossou, “Acoustic modes in photonic crystal fibres for distributed optical fibres sensors applications.” Theses, Université des Sciences et Technologie de Lille - Lille I, 2011.
[103] R. Hooke, *Lectures de potentia restitutiva, or, Of spring : explaining the power of springing bodies : to which are added some collections*. London : Printed for J. Martyn, 1678.
[104] L. Solomon, *Elasticité linéaire*. Masson et Cie Editeurs, 1968.
[105] Jean-Claude Charmet, *Mecanique du solide et des materiaux Elasticite-Plasticite-Rupture*. ".
[106] F. D. Murnaghan, *Finite Deformation of an Elastic Solid*. Wiley, 1951.
[107] D. S. Hughes and J. L. Kelly, “Second-Order Elastic Deformation of Solids,” *Phys. Rev.*, vol. 92, no. 5, pp. 1145–1149, Dec. 1953.
[108] S. Chaki and G. Bourse, “Guided ultrasonic waves for non-destructive monitoring of the stress levels in prestressed steel strands,” *Ultrasonics*, vol. 49, no. 2, pp. 162–171, Feb. 2009.
[109] G. W. Scherer, “Stress-induced index profile distortion in optical waveguides,” *Appl. Opt.*, vol. 19, no. 12, pp. 2000–2006, Jun. 1980.

[110] W. Zou, Z. He, A. D. Yablon, and K. Hotate, “Dependence of Brillouin Frequency Shift in Optical Fibers on Draw-Induced Residual Elastic and Inelastic Strains,” *IEEE Photonics Technol. Lett.*, vol. 19, no. 18, pp. 1389–1391, Sep. 2007.
[111] I. H. Malitson, “Interspecimen Comparison of the Refractive Index of Fused Silica” *JOSA*, vol. 55, no. 10, pp. 1205–1209, Oct. 1965.
[112] C. Sabatier *et al.*, “Influence of the core dopants on the Brillouin signature of specialty optical fibers,” in *5th Workshop on Specialty Optical Fibers and their Applications*, Limassol , Cyprus, 2017.
[113] “Interfiber Analysis Home Site.” [Online]. Available: http://www.interfiberanalysis.com/. [Accessed: 17-Oct-2018].
[114] R. Davidi, U. Ben-Simon, S. Shoham, I. Kressel, N. Gorbatov, and M. Tur, “The importance of Fiber Coating and Bonding Process in Accurate High Spatial Resolution Strain Measurements,” presented at the OFS-26.
[115] Q. Li, G. Li, and G. Wang, “Effect of the plastic coating on strain measurment of concrete by fiber optic sensor,” *Elsevier*, vol. 34, pp. 215–227, 2003.
[116] G. Zhou, H. Li, L. Ren, and D. Li, “Influencing parameters analysis of strain transfer in optic fiber Bragg grating sensors,” in *Advanced Sensor Technologies for Nondestructive Evaluation and Structural Health Monitoring II*, 2006, vol. 6179, p. 61790R.
[117] M. Alahbabi, Y. T. Cho, and T. P. Newson, “Comparison of the methods for discriminating temperature and strain in spontaneous Brillouin-based distributed sensors,” *Opt. Lett.*, vol. 29, no. 1, pp. 26–28, Jan. 2004.
[118] E. Burov, A. Pastouret, and L.-A. De Montmorillon, “Temperature and strain sensing optical fiber and temperature and strain sensor,” US9835502B2, 05-Dec-2017.
[119] D. B. Wittry, “Electron probe microanalyzer,” US2916621A, 08-Dec-1959.
[120] C. Sabatier *et al.*, “Combined experimental and simulation study of the fiber composition effects on its Brillouin scattering signature,” presented at the OFS-26.
[121] M. N. Alahbabi, Y. T. Cho, and T. P. Newson, “Simultaneous temperature and strain measurement with combined spontaneous Raman and Brillouin scattering,” *Opt. Lett.*, vol. 30, no. 11, pp. 1276–1278, Jun. 2005.
[122] D.-P. Zhou, W. Li, L. Chen, and X. Bao, “Distributed Temperature and Strain Discrimination with Stimulated Brillouin Scattering and Rayleigh Backscatter in an Optical Fiber,” *Sensors*, vol. 13, no. 2, pp. 1836–1845, Feb. 2013.
[123] B. G. Gorshkov and M. A. Taranov, “Simultaneous optical fibre strain and temperature measurements in a hybrid distributed sensor based on Rayleigh and Raman scattering,” *Quantum Electron.*, vol. 48, no. 2, p. 184, Feb. 2018.
[124] M. Alahbabi, Y. T. Cho, and T. P. Newson, “Comparison of the methods for discriminating temperature and strain in spontaneous Brillouin-based distributed sensors,” *Opt. Lett.*, vol. 29, no. 1, pp. 26–28, Jan. 2004.
[125] “Corning® SMF-28® Ultra Optical Fiber.” [Online]. Available: https://www.corning.com/media/worldwide/coc/documents/Fiber/SMF-28%20Ultra.pdf.
[126] “Corning® LEAF® Optical Fiber.” [Online]. Available: https://www.corning.com/media/worldwide/coc/documents/Fiber/LEAF%20optical%20fiber.pdf.
[127] S. R. Nagel, J. B. MacCHESNEY, and K. L. WALKER, “An Overview of the Modified Chemical Vapor Deposition (MCVD) Process and Performance,” *IEE Trans. Microw. Theory Tech.*, vol. MTT-30, no. 4, pp. 305–322, Apr. 1982.
[128] M. Vivona, “Radiation Hardening of Rare-Earth Doped Fiber Amplifier,” Université Jean Monnet Saint Etienne, 2013.

[129] T. Kitoh, N. Takato, M. Yasu, and M. Kawachi, “Bending loss reduction in silica-based waveguides by using lateral offsets,” *J. Light. Technol.*, vol. 13, no. 4, pp. 555–562, Apr. 1995.
[130] Y. Tsuchida, K. Saitoh, and M. Koshiba, “Design and characterization of single-mode holey fibers with low bending losses,” *Opt. Express*, vol. 13, no. 12, pp. 4770–4779, Jun. 2005.
[131] Oz Optics, “Fiber Optic Distributed Strain and Temperature Sensors (DSTS).” [Online]. Available: https://www.ozoptics.com/ALLNEW_PDF/DTS0139.pdf.
[132] H. Xiao *et al.*, “A numerical analysis of GeO 2 -doped multi-step index single-mode fiber for stimulated Brillouin scattering,” *J. Opt.*, vol. 20, no. 6, p. 065701, 2018.
[133] T. R. Parker, M. Farhadiroushan, V. A. Handerek, and A. J. Rogers, “The simultaneous measurement of strain and temperature distributions from Brillouin backscatter,” pp. 1–1, Jan. 1997.
[134] *Evaluation of measurement data - Guide to the expression of uncertainty in measurment*. BIPM, 2008.
[135] C. Xing *et al.*, “Distributed multi-parameter sensing utilizing Brillouin frequency shifts contributed by multiple acoustic modes in SSMF,” *Opt. Express*, vol. 26, no. 22, pp. 28793–28807, Oct. 2018.
[136] “LEAF® Optical Fibre.” [Online]. Available: https://www.corning.com/au/en/products/communication-networks/products/fiber/leaf-fiber.html. [Accessed: 10-Jan-2019].
[137] C. C. Lee, P. W. Chiang, and S. Chi, “Utilization of a dispersion-shifted fiber for simultaneous measurement of distributed strain and temperature through Brillouin frequency shift,” *IEEE Photonics Technol. Lett.*, vol. 13, no. 10, pp. 1094–1096, Oct. 2001.
[138] “Home.” [Online]. Available: https://www.viavisolutions.com/en-us. [Accessed: 10-Jan-2019].
[139] A. F. Fernandez *et al.*, “Radiation-tolerant Raman distributed temperature monitoring system for large nuclear infrastructures,” *IEEE Trans. Nucl. Sci.*, vol. 52, no. 6, pp. 2689–2694, Dec. 2005.
[140] S. Rizzolo *et al.*, “Radiation effects on optical frequency domain reflectometry fiber-based sensor,” *Opt. Lett.*, vol. 40, no. 20, p. 4571, Oct. 2015.
[141] C. Sabatier *et al.*, “6 MeV Electron Exposure Effects on OFDR-based Distributed Fiber-based Sensors,” *IEEE Trans. Nucl. Sci.*, pp. 1–1, 2018.
[142] C. Cangialosi *et al.*, “Development of a Temperature Distributed Monitoring System Based On Raman Scattering in Harsh Environment,” *IEEE Trans. Nucl. Sci.*, vol. 61, no. 6, pp. 3315–3322, Dec. 2014.
[143] C. Cangialosi *et al.*, “Hydrogen and radiation induced effects on performances of Raman fiber-based temperature sensors,” in *23rd International Conference on Optical Fibre Sensors*, 2014, vol. 9157, p. 91576U.
[144] X. Phéron, J. Bertrand, S. Girard, Y. Ouerdane, S. Delepine-Lesoille, and A. Boukenter, “Brillouin scattering based sensor in high gamma dose environment: design and optimization of optical fiber for long-term distributed measurement,” in *OFS2012 22nd International Conference on Optical Fiber Sensors*, 2012, vol. 8421, p. 8421A4.
[145] X. Phéron *et al.*, “High γ-ray dose radiation effects on the performances of Brillouin scattering based optical fiber sensors,” *Opt. Express*, vol. 20, no. 24, pp. 26978–26985, Nov. 2012.
[146] S. Girard *et al.*, “Recent advances in radiation-hardened fiber-based technologies for space applications,” *J. Opt.*, vol. 20, no. 9, p. 093001, 2018.

[147] P. C. Wait and T. P. Newson, “Landau Placzek ratio applied to distributed fibre sensing,” *Opt. Commun.*, vol. 122, no. 4, pp. 141–146, Jan. 1996.
[148] K. D. Souza, P. C. Wait, and T. P. Newson, “Characterisation of strain dependence of the Landau-Placzek ratio for distributed sensing,” *Electron. Lett.*, vol. 33, no. 7, pp. 615–616, Mar. 1997.
[149] G. Melin *et al.*, “Specific radiation restitant single-mode fiber for sensing in high dose radiation environments,” *IEEE Trans. Nucl. Sci.*

Conclusion

The objective of this PhD thesis work was to evaluate how the definition of a new optical fiber generation could overcome the scientific and technical factors limiting today the performances of distributed sensors. The main goal was to design and manufacture an optical fiber allowing through a tailored Brillouin signature, to discriminate between the temperature and strain contributions to the sensor measurements, and this using a single optical fiber. In order to fulfill this objective, a good knowledge about the Brillouin scattering mechanisms in optical fibers and about the current state-of-the-art regarding the accessible sensor technologies was required. To conceive the targeted fiber, a strategy combining simulations and experiments was chosen. Simulation codes have been built to model a fiber Brillouin response and they have been exploited in order to identify optical fiber structures having several Brillouin peaks in their responses. From these simulations, two fiber structures have been identified and then manufactured thanks to iXblue's production facilities. Their experimental characterization confirms that these fiber possess low attenuation levels in the infrared and Brillouin signatures very close to those theoretically predicted. Metrology study was then conducted, highlighting that some of the drawn fibers present discrimination performances exceeding those reported by other research teams in the literature. In parallel, another approach was evaluated for the discrimination, in collaboration with the industrial Viavi Solutions. In this case, the discrimination is possible thanks to a dedicated interrogation scheme combining the measurements of both the Rayleigh and Brillouin responses on the same single-mode optical fiber.

In this PhD thesis, several remarkable results have been obtained, allowing to improve our understanding of the distributed fiber-based sensors.

Through both experiments and simulations, we show how the Brillouin response of an optical fiber strongly depends on its composition and on its refractive index profile. This was achieved by studying the dopants that are commonly incorporated in the core and cladding of the telecom-grade optical fibers. Thanks to this study, we have been able to develop a scalar model that can predict the Brillouin spectrum of an optical fiber and its evolution under the effects of both temperature and stress, knowing its composition and refractive index profile.

This validated model can now be used to conceive new fiber structures with tailored Brillouin spectrum for various sensing applications.

A metrology approach has been developed to assess the discrimination potential of the different fiber structures. This approach shows that some (2) of the fibers manufactured during the PhD thesis present superior discrimination capabilities than the competing fibers discussed in literature. Furthermore the developped fibers can be interrogated by either BOTDR or BOTDA sensors.

Finally, we demonstrate how the sensing scheme offered by the DTSS of Viavi Solutions is able to achieve the temperature and strain distributions discrimination along a Telecom-grade fibers, characterized by classical one-peak Brillouin signature. The potential of the DTSS to perform this discrimination has been evaluated when the sensing optical fiber is submitted to radiations (γ-rays, X-rays), the interrogator being kept in a radiation-free zone. The obtained preliminary results confirm that the discrimination capability is maintained, even for doses up to 1.5 MGy deposited on the fiber. However, this distributed sensors, as all such sensors, will be affected by a reduction of the possible sensing distance under irradiation, caused by the radiation-induced attenuation phenomenon.

Perspectives

The presented work shows that the targeted discrimination could be achieved by working both at the fiber and at the interrogator levels. An obvious first perspective consists in combining this novel architecture of interrogator with one of the developed multi-peak fibers. Should be able to ameliorate the temperature / strain discrimination capability of the sensing line.

A second possible improvement could be the conception and the manufacturing of a pure-silica or fluorine-doped core fiber with a multi-peak Brillouin signature. Such fiber should allow the implementation of the sensor in radiation environments such as those encountered at nuclear power plants or at high energy physics facilities. Indeed the radiation effects on Brillouin scattering have already been studied in the literature and it was shown that those optical fibers are significantly less sensitive to radiation, with reduced radiation induced attenuation at MGy dose levels and almost no radiation-induced shift of their Brillouin peak frequencies.

Finally, at a shorter term, tests in real conditions, such as the monitoring of infrastructure, under radiation environment, or at very high temperature of a strained-controlled optical fiber, have to be carried out in order to experimentally assess the discrimination capacities on-site and not just in-lab.

List of Publications

- IEEE TNS:
  - S. Rizzolo, C. Sabatier, A. Boukenter, E. Marin, Y. Ouerdane, M. Cannas, J. Perisse, J.R. Macé, S. Bauer, and S. Girard, "**Radiation Characterization of Optical Frequency Domain Reflectometry Fiber-Based Distributed Sensors**" *IEEE Trans. Nucl. Sci.*, vol. 63, no. 3, pp. 1688–1693, Jun. 2016.
  - C. Sabatier *et.al*, "**6 MeV Electron Exposure Effects on OFDR-based Distributed Fiber-based Sensors**", *IEEE Trans. Nucl. Sci.*, vol. 65, no. 8, pp. 1598–1603, Aug. 2018.
  - C. Sabatier *et.al*, "**Distributed Optical Fiber Sensor Allowing Temperature and Strain Discrimination in Radiation Environments**", *IEEE Trans. Nucl. Sci*, DOI: 10.1109/TNS.2019.2903922 (accepted)
  - T. Blanchet, A. Morana, T. Allanche, C. Sabatier, I.Reghioua, E. Marin, A. Boukenter, Y. Ouerdane, P. Paillet, M. Gaillardin, O. Duhamel, C. Marcandella, M. Trinczek, G. Assaillit, G. Auriel, D. Aubert, G. Laffont, and S. Girard, "**X-ray, Proton and Electron Radiation Effects on Type I Fiber Bragg Gratings**", *IEEE Trans. Nucl. Sci.*, vol. 65, no. 8, pp. 1632–1638, Aug. 2018
- Journal Lightwave of Technology:
  - C. Sabatier *et.al*, "**Combined Experimental and Simulation Study of the Fiber Composition Effects on Its Brillouin Scattering signature**", publication in JLT (accepted)
  - A. Alessi, A. Guttilla, S. Agnello, C. Sabatier, T.Robin, A. Barnini, D. Di Francesca, G. Li Vecchi, M. Cannas, A. Boukenter, Y. Ouerdane, S.Girard, " **Near Infrared Radiation Induced Attenuation in Aluminosilicate Optical Fibers**", submitted in JLT
  -
- Optic Express:
  - A. Piccolo, S. Delepine-Lesoille, M. Landolt, S. Girard, Y. Ouerdane, C. Sabatier, "**Coupled temperature and g-radiation effect on silica-based optical fiber strain sensors based on Rayleigh and Brillouin scatterings**", publication in Optic Express (accepted)

Conferences

- 2016 :
  - JINOG : C. Sabatier *et al*, "**Détermination de la distribution radiale des pertes dans une fibre optique**"
- 2017 :
  - RADECS 2017:
    - C. Sabatier *et.al*, "**6 MeV Electron Exposure Effects on OFDR-based Distributed Fiber-based Sensors**", poster contribution
    - T. Blanchet, A. Morana, T. Allanche, C. Sabatier, I. Reghioua, E. Marin, A. Boukenter, Y. Ouerdane, P. Paillet, M. Gaillardin, O. Duhamel, C. Marcandella, M. Trinczek, G. Assaillit, G. Auriel, D. Aubert, G. Laffont, and S. Girard, "**X-ray, Proton and Electron Radiation Effects on Type I Fiber Bragg Gratings**", oral contribution
  - WSOF 2017:
    - C. Sabatier *et al*, "**Influence of the core dopants on the Brillouin signature of specialty optical fibers**", poster contribution
  - FMR 2017:
    - C. Sabatier *et al*, "**Effet des électrons de 6 MeV sur les capteurs OFDR à fibre optiques**", oral contribution
- 2018 :
  - RADECS 2018:
    - C. Sabatier *et.al*, "**Distributed Optical Fiber Sensor Allowing Temperature and Strain Discrimination in Radiation Environments**", oral contribution
    - G. Li Vecchi, C. Sabatier, D. Di Francesca, S. Girard, Y. Kadi, M. Brugger, "**Infrared Radiation Induced Attenuation of Radiation Sensitive Optical Fibers: Influence of Temperature and Modal Propagation**", oral contribution

- OFS 2018:

  - C. Sabatier *et.al*, "**Combined Experimental and Simulation Study of the Fiber Composition Effects on Its Brillouin Scattering signature**", poster contribution

- EWSHM 2018:

  - C. Sabatier *et al*, "**Potential of Optical Frequency Domain Reflectometry fibre-based sensors for distributed temperature measurements during vacuum thermal cycling of satellites**", oral contribution

- FMR 2018:

  - C. Sabatier *et.al*, "**Distributed Optical Fiber Sensor Allowing Temperature and Strain Discrimination in Radiation Environments**", oral contribution